ABSTRACT

Title of Document: **DEVELOPMENT OF AN AERODYNAMIC SYNTHETIC JET ACTUATOR BASED ON A PIEZOCERAMIC BUCKLED BEAM**

Dan J. Clingman Masters of Science in Aerospace Engineering February 2006

Directed By: Professor Alison Flatau Department of Aerospace Engineering, University of Maryland

This thesis documents the development of a synthetic jet actuator powered by an Enhanced Displacement (ED) motor based on piezoceramic bimorph beam operating in a post-buckled state. The motor is modeled using Lagrange's equations to capture the post-buckling beam dynamics and the dynamics of supporting elements of the motor. The fluid section of the actuator, including the air pressure and velocity within chamber, is modeled by a three-state adiabatic flow model. The motor and fluid models are coupled together to form a complete synthetic jet actuator model.

An ED motor was fabricated and tested and shows that it produces eight times the energy compared to the same bimorph operated without a buckling load. Motor and model data agree well for both static and dynamic operation.

The ED motor was installed in a synthetic jet actuator and demonstrated the ability to produce flows in excess of 15 m/sec with duty cycles varying between 2 Hz and 30 Hz. For these tests the drive signal used was a square wave and jet velocity was only mildly dependent of actuation frequency.

DEVELOPMENT OF AN AERODYNAMIC SYNTHETIC JET ACTUATOR BASED ON A PIEZOCERAMIC BUCKLED BEAM

By
Dan J, Clingman

Thesis submitted to the Faculty of the Graduate School of the
University of Maryland, College Park, in partial fulfillment
of the requirements for the degree of
Masters in Engineering
2006

Advisory Committee:
Professor Alison Flatau, Chair
Professor Inderjit Chopra
Professor Balakumar Balachandran

Dedication

I dedicate this work to my family. Without Annette this work would not have happened. Amy and Kathleen suffered without a Daddy for much to long. Finally, Dean and Beryl Clingman, who showered me with love and helped, develop a life long love of engineering.

Acknowledgements

I would like to acknowledge people and organizations who with out there help this work would never have been accomplished. My wife Annette Clingman who's constant support while keeping our household happy and under control made it possible for me to accomplish this work Professor Alison Flatau who secured funding and provided advice and support was essential to completion of the work. Her friendship and advice is appreciated. Ted Whitley, my Boeing manager and mentor, who's "can do" attitude and support made my trip to Maryland possible. His confidence in me and support were critical to allowing this work to take place. Dr. Bob Ruggeri, he kept the bean counters off my back and provided important consultation. Darin Arbogast, my cube mate, who programmed the data accusation system and listened to me belly aching. Lynn Gravatt, whose long hours building and testing synthetic jets was a big help. All the graduate students whose moral support was critical to keeping me on task. These include Luke Twarek, Dave Pullen, Supartik Datta and Sandra Ugrina. Finally, I would like to thank The National Science Foundation and Boeing Phantom Works for financial support and Mr. Bud Cass of Advanced Cerametrics Inc. who provided Piezo Fiber Composite elements that form the basis of the device.

Table of Contents

Chapter 1: Active Flow Control Overview and Synthetic Jet Technology

Section 1.1 Active Flow Control Overview

Active Flow Control (AFC) can mitigate undesirable aerodynamic properties in designs where other constraints force a compromise. It will not improve a good design [1]. An example is the helicopter blade where the blade undergoes huge dynamic changes in flight regime during a single rotation. When the helicopter is in forward flight and the blade is in the retreating half of its cycle, the blade operates at or near stall. When the blade is in the advancing half of the cycle it is operating near Mach 1. The ideal aerodynamic solution is to morph the blade between a low speed, thick blade and a high speed, thin blade during each rotation. This is not practical and a compromised fixed geometry blade leads to vibration, limited helicopter speed and excess noise. AFC can be applied to "synthetically morph" the blade to increase performance [2]. Transport aircraft wings are also a compromise between a low drag wing needed during cruise and a high lift wing needed during take off and landing. The wing is adapted by including high lift systems such as flaps and slats with corresponding increases in weight, drag and complexity. Work is being done to reduce the size and complexity of high lift systems by applying AFC [3]. Modern fighter aircraft and UAVs have serpentine and nonuniform cross-section air inlets leading to the jet engine. This complex geometry creates problems maintaining a constant pressure distribution at the jet engine. AFC is being developed to create constant pressure profiles in complex geometry engine inlets [4].

The goal of aerodynamic AFC concepts is to cause large scale changes in flow by introducing small dynamic airflow perturbations. This is accomplished by exploiting regions of attached air flow that are close to separating from the boundary layer. These nearly unstable regions require little energy to trip them into turbulent flow so small energy injectors can be used. Energy can be injected by moving physical surfaces such as vibrating surface actuators [5] or by injecting oscillatory air with synthetic jets [6].

Two parameters are generally used to quantify the minimum injected airflow velocity and optimal injected frequency required to achieve AFC benefit. These parameters are C_μ, a ratio of ejected momentum to total flow momentum and F^+, a non dimensional frequency related to the time scale of flow over the surface of interest.

Equations 1.1 and 1.2 show the definition of C_μ and F^+ for a synthetic jet placed on a trailing edge flap to reduce separation [7].

$$C_\mu = 2(H/c)(U_j/U_\infty)^2 \qquad \textbf{(1.1)}$$

$$F^+ = fX_f/U_\infty \qquad \textbf{(1.2)}$$

Where H is the chordwise slot width, c is the chord length of the flap, U_j is the RMS velocity of the jet, U_∞ is the free stream velocity, f is the synthetic jet air injection frequency and X_f is the length between the slot and the trailing edge of the flap.

Each AFC application will have a different definition and range of effective values for C_μ and F^+ that depending on the application geometry and goals. For example,

Amitay [8] defines C_μ for a cylinder with an internal synthetic jet as shown in ***Equation 1.3***.

$$C_\mu = \frac{2\rho_j v^2{}_j b_j}{\rho_a U_\infty^2 D} \qquad \textbf{(1.3)}$$

where $\boldsymbol{\rho_j}$ is the density of the jet air, $\boldsymbol{v_j}$ is the velocity of the jet, $\boldsymbol{b_j}$ is the jet slot radial width, $\boldsymbol{\rho_a}$ is the density of the free stream air, $\boldsymbol{U_\infty}$ is the velocity of the free stream air and $\boldsymbol{D}$ is the diameter of the cylinder. This definition takes into account the density of the two flows and is appropriate where the characteristics of the synthetic jet produce differences in air density.

AFC can be accomplished with many forms of energy injection; this thesis will concentrate on synthetic jet actuators.

Section 1.2 Synthetic Jet Technology

The synthetic jet concept consists of an exit orifice, an enclosed chamber and a method to change the pressure within the chamber so air is forced into and out of the chamber through the orifice or slot. Figure 1.1 shows the synthetic jet concept. The synthetic jet actuator is made of two sections. The motor provides electrical to mechanical conversion and the mechanical to fluid interface transforms the mechanical energy into air flow.

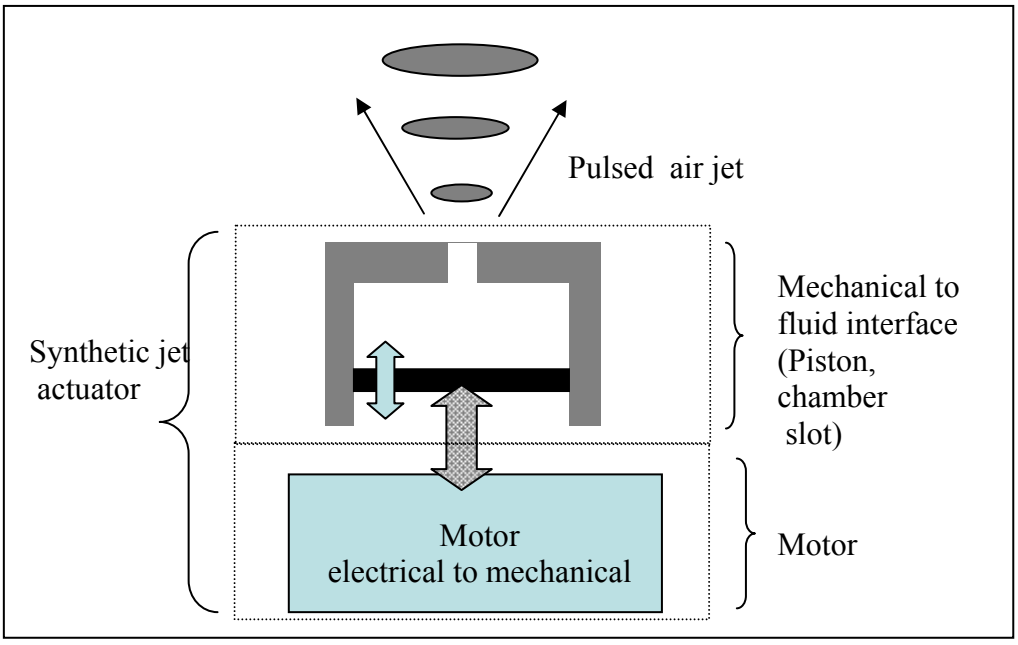

Figure 1.1 Synthetic jet concept.

Figure 1.2 lists different synthetic jet concepts and some key characteristics. Concepts include moving piston, flexing membrane, gas detonation and pneumatic driven acoustic resonances.

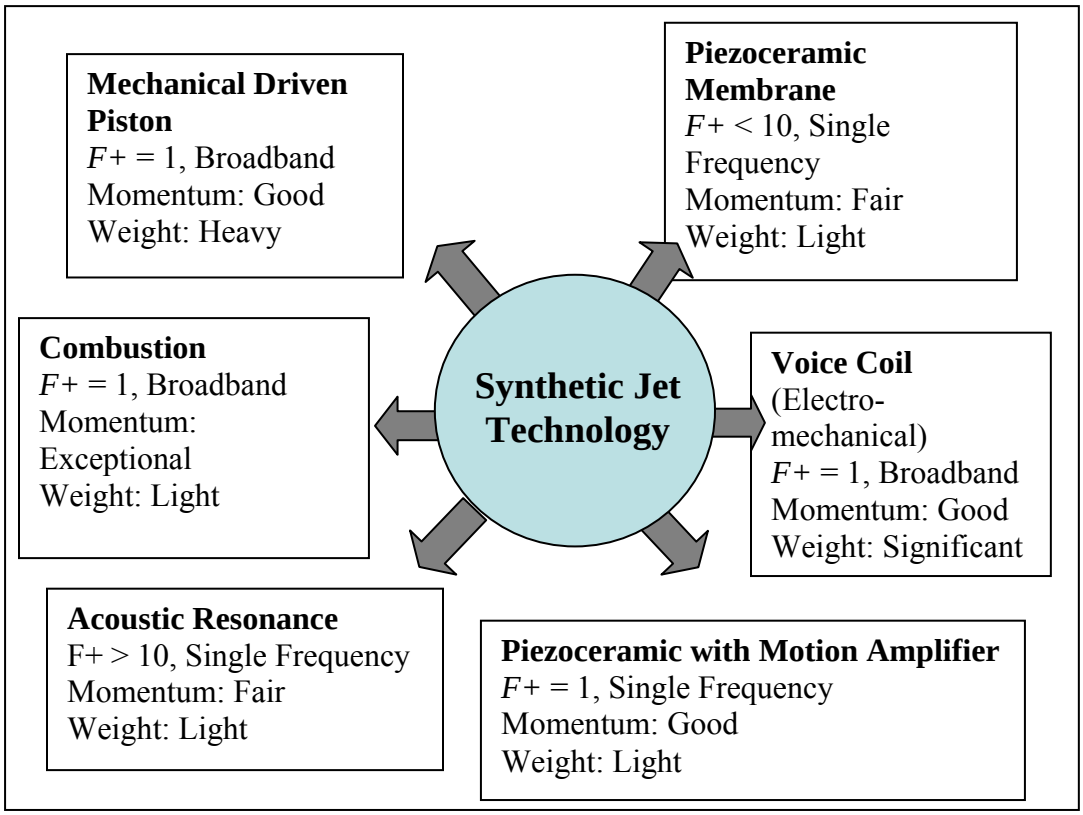

Figure 1.2 Synthetic jet technology summary.

Gilarranz [9] developed an electric motor powered, piston-based synthetic jet and shows that it reduces separation. The device was complicated and required relatively high power to operate but did supply high momentum at moderate frequency around 100 Hz producing a C_m greater the 1% at F^+ near to 1.

Chen [10] uses a Thunder® piezoceramic membrane to power a synthetic jet. The displacement of this type of membrane is around 0.25 mm when operated in the hundreds of hertz range. The flow output by this type of actuator can be characterized as high velocity but low mass flow resulting in similar Cμ compared to piston type synthetic jest. Typically, these jets operate with an F^+ of around 10 (corresponding

to membrane excitation at frequencies of hundreds of hertz). Maximum output is generated when the actuator is operated at mechanical resonance which is typically an order of magnitude higher than the desired jet oscillation frequency. The excitation frequency can be modulated to produce lower frequency energy content in the output jet. Ugrina [18] shows that by matching the chamber Helmholtz acoustic resonance to the Thunder® mechanical resonance, significant velocity gains can be achieved.

McCormick [11] developed magnetic-based voice coil actuators that directly drive a piston much like a speaker. The jet produces large mass flow at frequencies in the hundred hertz range. These actuators are heaver than the Thunder®-based synthetic jet but produce more momentum around targeted F^+ frequencies due to much larger piston displacement (2.5 mm). These synthetic jets are broadband in nature and can provide jet oscillation over a range of frequencies without modulation.

Funk [12] experimented with a combustion synthetic jet that ignites a mixture of hydrogen and oxygen in a chamber and in-turn produces a strong jet. This jet provides the momentum and velocity necessary to support high Mach number flow control but suffers from requiring two hard-to-handle chemicals. Additionally, this jet concept does not provide a vacuum, which can be important when attempting to influence the boundary layer [13].

Raman [14] developed a compressed air powered acoustic synthetic jet. This jet uses tubes to set up an acoustic resonance thereby driving cyclic flow. This device

produces high frequency, high velocity, low mass-flow similar to jet flows produced by the Thunder®-based synthetic jet. An advantage of this device is that it has few moving parts and can be powered by aircraft bleed air.

Calkins and Mabe [15] developed a synthetic jet actuator based on recurve piezo-polymer actuators. The recurve actuators were made from multi layers of PVDF (PolyVinyliDene Fluoride) flexures, which were attached to a piston. These actuators are similar to voice coil actuators, as both use a direct drive motor to drive a piston. Piezo-polymer strains generate small displacements, which are amplified by the recurve configuration. Further amplification is accomplished by operation at resonance. Their frequency of operation is about 100 Hz, but since the device operates at resonance, they only produce a single frequency. These devices are very light weight and use low levels of power to achieve displacements in the order of 6 mm and peak air velocity of 25 m/sec.

Section 1.3 Synthetic Jet Model

Three energy domains are represented in the synthetic jet. These domains are often modeled with partial differential equations that relate the temporal and spatial response. Navier-Stoke's Equations provide a basis for modeling the fluid flow, structural elastic theory provides a basis for modeling the flexible and active structures and Maxwell's Equations provide the basis for electrical interaction. For a realistic synthetic jet, a closed form solution is not available and numerical methods and/or simplifying assumptions are needed to build a useful model.

Gallas [16] developed a lumped parameter model that links the three energy domains. The basis of this model is the assumption that variables are separable; time varying properties of the synthetic jet and its spatial variables are independent. This allows the governing partial differential equations to be separated into ordinary differential equations in time and space. A second assumption is that variables in different energy domains can be represented in other energy domains by linear scaling. The model represents the complete synthetic jet in the electrical domain, which allows simplified analysis. Information provided by this model is limited to bulk variables such as jet velocity and chamber pressure. This model is computationally inexpensive and is ideal for parametric optimization. The model is not useful for analysis of flow interaction because flow variables of interest vary in both space and time.

Computational Fluid Dynamics (CFD) is often used for analysis of synthetic jet interaction with free stream flow [17]. CFD is a numerical method that provides a coupled solution between time and space. Most research focuses on the jet interaction with the flow and models the synthetic jet with a pulsating jet stream. Ugrina [18] analyzed the fluid portion of a Thunder® based synthetic jet using CFD. The analysis includes both jet interactions with the free stream and chamber dynamics including the effect of the moving diaphragm. The diaphragm is modeled as a sinusoidal moving boundary. Computation time for these models can require tens of hours for each run, making optimization difficult. Yamaleev [19] provides a simplified CFD model that reduces the size of the model while maintaining critical features. This allows for relatively fast execution such as required for optimization studies.

The author did not find literature that described numerical models that combined fluid, mechanical and electrical domains. Recent advances in commercial software such as Control Multiphysics® offer a combined physics option that makes such analysis possible. It may not be necessary to provide this level of modeling because the lumped parameter modeling technique may provide information such as power and efficiency at much less computational cost.

Section 1.4 Electo-Mechanical Actuator Design

Piezo-active materials are selected for synthetic jets because this class of materials provides a lightweight energy conversion between electrical energy and mechanical energy [20]. Energy is converted between electrical charge and mechanical strain.

Piezoceramics such as PZT-5A [21] produce about 0.1% strain with an elastic modulus of 45 GPa. This motion can be characterized by a high force and small displacement. Piezoceramics provide large forces and small motions that must be coupled into moving air for a synthetic jet to function efficiently. Two mechanisms are available to adjust the impedance between the piezoceramic material and the air jet; mechanical motion amplification between the piezoceramic material and piston and the ratio between orifice area and piston area. Unlike applications such as flaps and pumps where piezoceramic energy is delivered to the load and is a function of displacement and force, energy transferred to the air is similar to viscous damping and is a function of velocity and force.

Section 1.5 Actuation Motion Amplification

Motion amplifiers have been constructed that convert the low displacement, high force output produced by a piezoceramic stack into high displacement, low force motion. Examples are the X-Frame actuator developed by Prechtl and Hall for a helicopter rotor blade servo flap [22] and a flexure-based, voice coil actuated, high ratio vortex generator system developed by Osborn [23]. See Figure 1.3. These devices provide constant motion amplification from quasi-static operation up to the resonant frequency of the device. Motion amplification devices can use the higher output of the piezoceramic stack d_{33} mode of operation compared to other types of piezoceramic based synthetic jet actuators which use the less authority d_{31} mode. Lesieutre [24] developed a nonlinear motion amplifier that couples a piezoceramic stack to a load that potentially increases energy transfer by 100%. The nonlinear element was constructed with a bell crank mechanism that produces maximum

motion amplification at the beginning of the piezo-stack and minimum amplification at the end of the stroke.

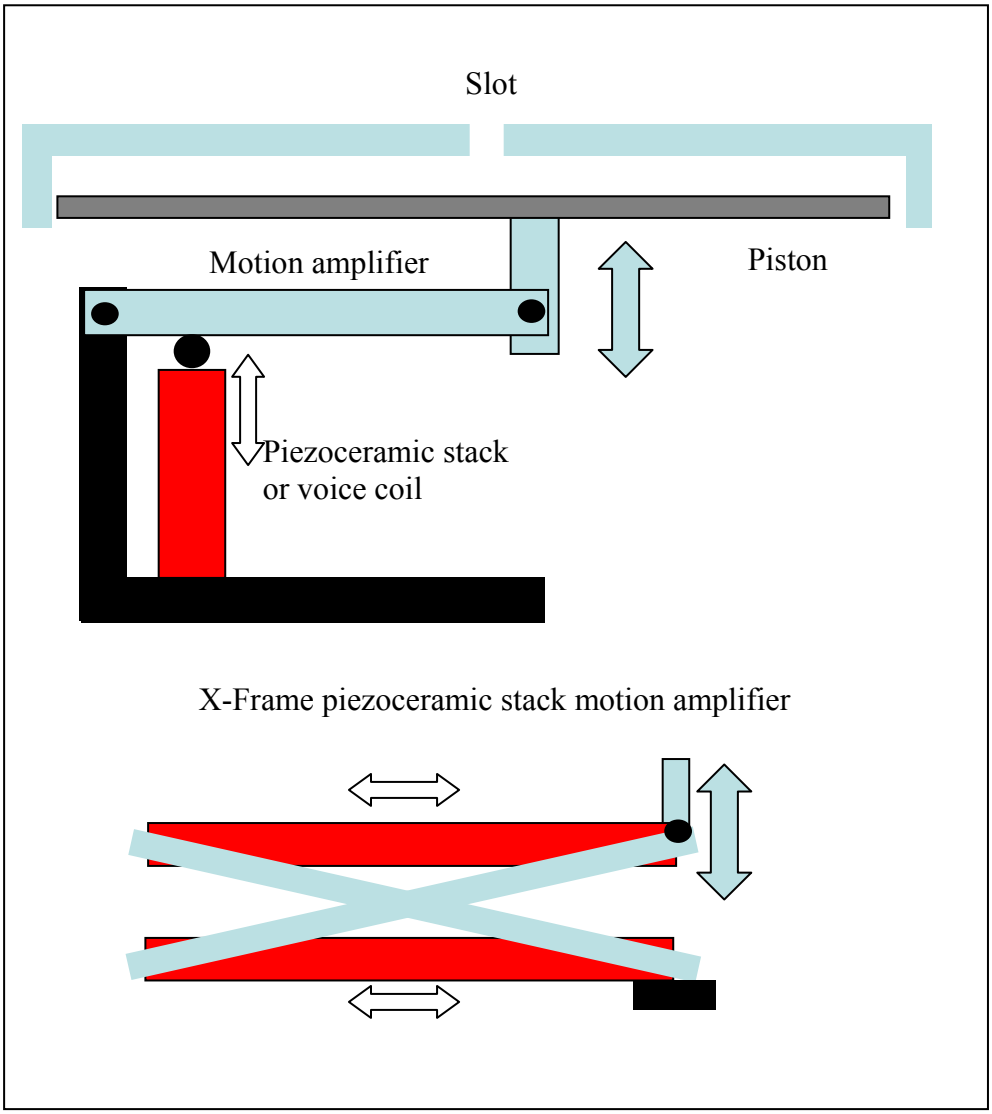

Figure 1.3 Small displacement motion amplifiers.

A different class of motion amplifiers utilizes the d_{31} mode of the piezoceramic material. Piezoceramic material is bonded to a structure and when charge is applied, the material strain is coupled into the structure, producing a bending moment, so that

the structure is deformed. This motion amplification mechanism can be applied to both diaphragm and piston type synthetic jets.

Section 1.6 Piezoceramic Bonded Wafer Motion Amplification

The d_{31} coupling mechanism is used for the diaphragm based synthetic jet actuators [20]. See Figure 1.4. Diaphragm actuators typically produce out of plane motion of approximately 25 μm when operated below their resonant frequency. The diaphragm has resonant frequencies on the order of 1 kHz. These synthetic jets typically produce high velocity and low displacement. This can be coupled with a high piston-to-orifice area ratio to produce useful jet momentum [18].

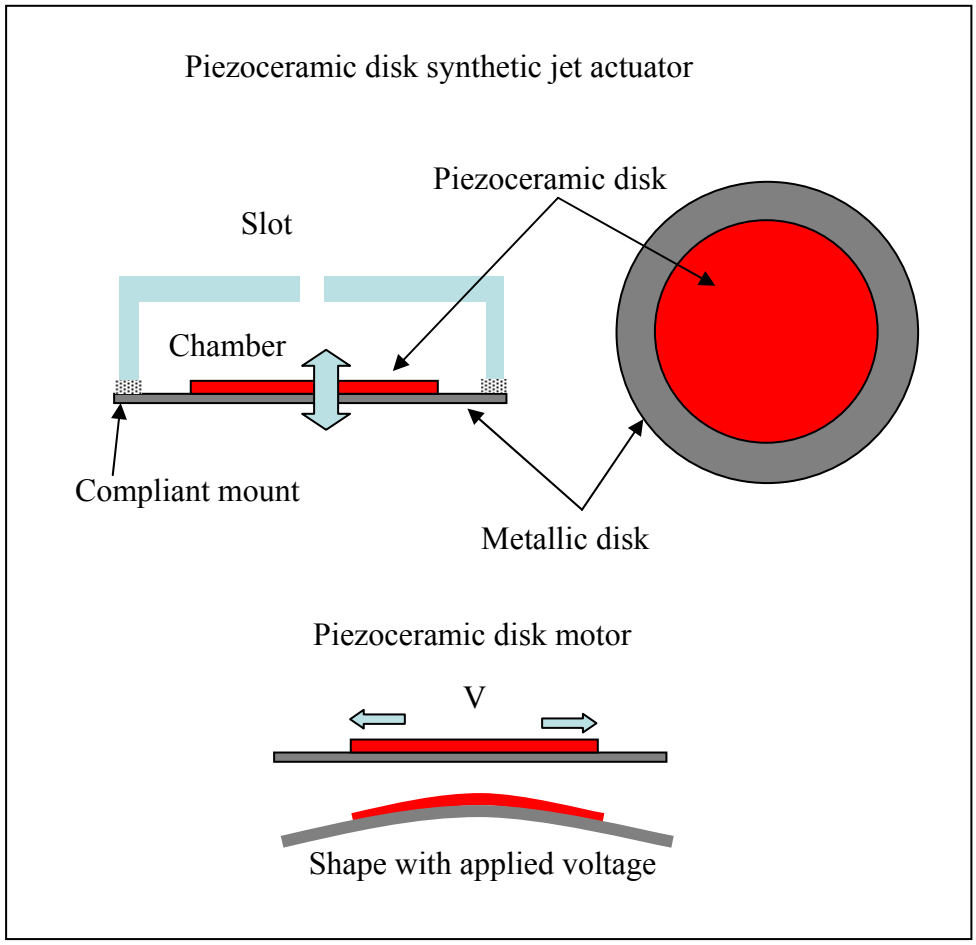

Figure 1.4 Piezoceramic disk synthetic jet.

Bailo, Brei and Calkins [25] developed a motion amplifier based on a recurve piezo-polymer actuation element operating in the d_{31} mode. The actuator was composed of three segment multilayer PVDF flexures with fixed end conditions. The PVDF was arranged such that upon application of a voltage, the upper and lower halves of the flexure move in opposite directions with a constant radius curvature. This is achieved by operating two end segments of each flexure in phase with each other and 180 degrees out of phase with the center segment. Additionally, the fixed ends allow easy stacking in parallel or series. See figure 1.4. Motion amplifications by a factor of a hundred are easily obtained. The dynamic behavior of a piezoceramic recurve actuator is presented by Ervin and Brei [26] including information on resonant frequencies and mode shapes.

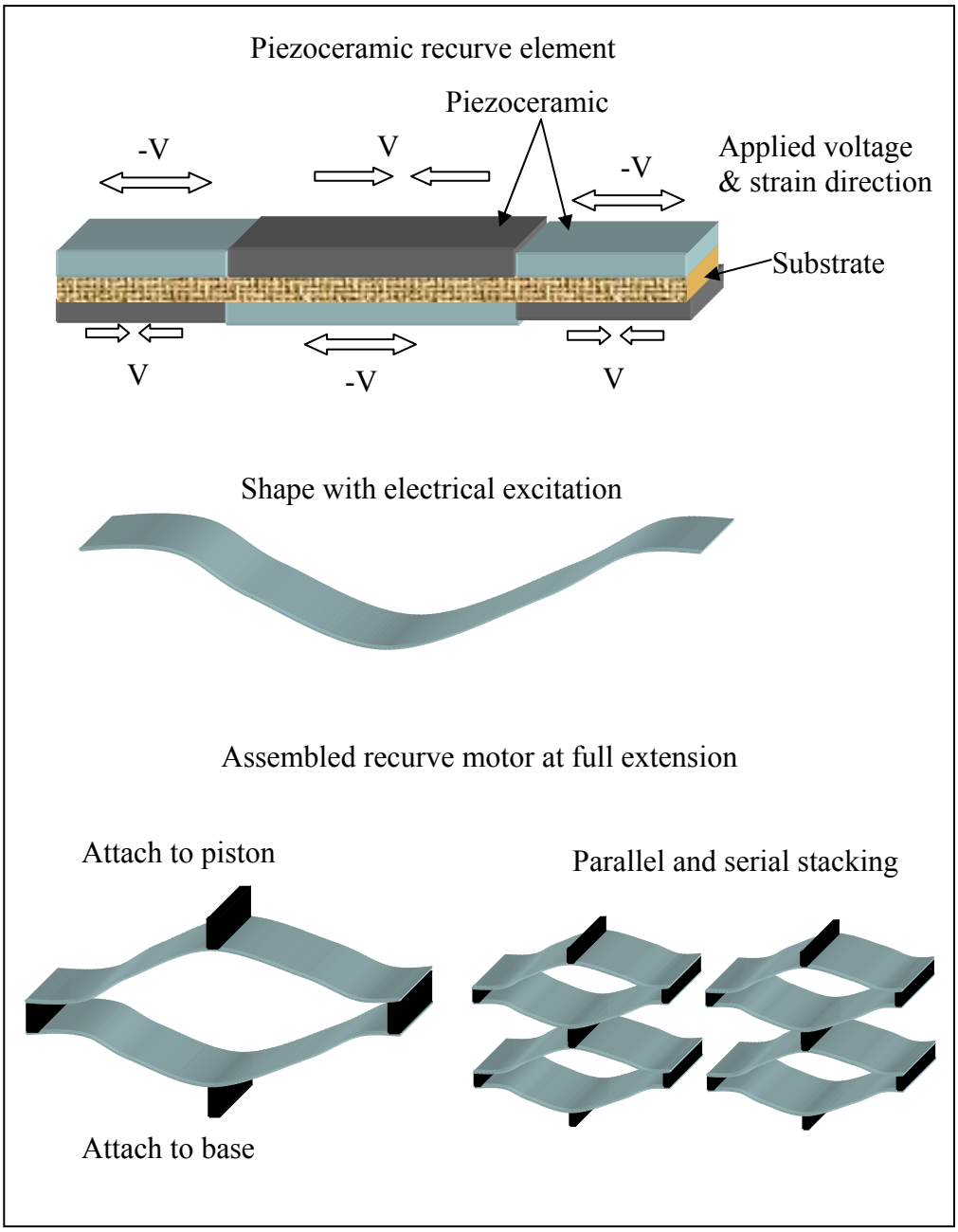

Figure 1.5 Piezo-material recurve-based motion amplifier.

Section 1.7 Motion Amplification by Resonant Operation

Operating a synthetic jet at the piezo motor structural resonance frequency will increase air jet momentum. Two effects work to increase momentum. First, at resonance, the piezoceramic motor maximum force occurs at maximum velocity and

zero displacement, increasing the energy coupling between the piezoceramic material and the vibrating motor structure. Second, the resonating motor structure has a much higher amplitude displacement and velocity, which more efficiently couples energy from the motor into air due to the viscous nature of the load. Both effects work together to increase synthetic jet performance. A difficulty with the resonant approach is that it operates in a very narrow band of frequencies restricts the actuator to a single F^+ value which limits the ability of the jet to trip laminar flow into turbulent flow. Amitay [8] has addressed this issue by amplitude modulating a disk type synthetic jet actuator operating at resonance to produce flow energy at a wide range of F^+ frequencies. The effectiveness of this approach is limited because the modulation process is not efficient at transferring energy from high to low frequencies.

Section 1.8 Nonlinear Motion Amplification

Lesieutre and Davis [27] have shown that inherent piezo-material energy transduction efficiency does not limit the device transduction efficiency. A d_{31} based piezoceramic flexure/beam with an applied compressive load will increase the transduction efficiency as the beam approaches the critical buckling load. The theoretical limit approaches 100% efficiency at buckling. The coupling between the piezoceramic and the load can be increased by the use of a nonlinear linkage. Lesieutre [24] shows that piezoceramic energy coupling to the load can be increased by 100% for a spring load. Figure 1.6 shows these concepts. Clingman and Ruggeri [28] show that a nonlinear linkage can be used to reduce by a factor of 300 the energy required to twist a wing by transferring strain energy between the blade and a set of

auxiliary springs. These authors show how nonlinearities can be used to increase actuator performance and how piezoceramic bimorphs and structural buckling can be combined to produce a superior actuator.

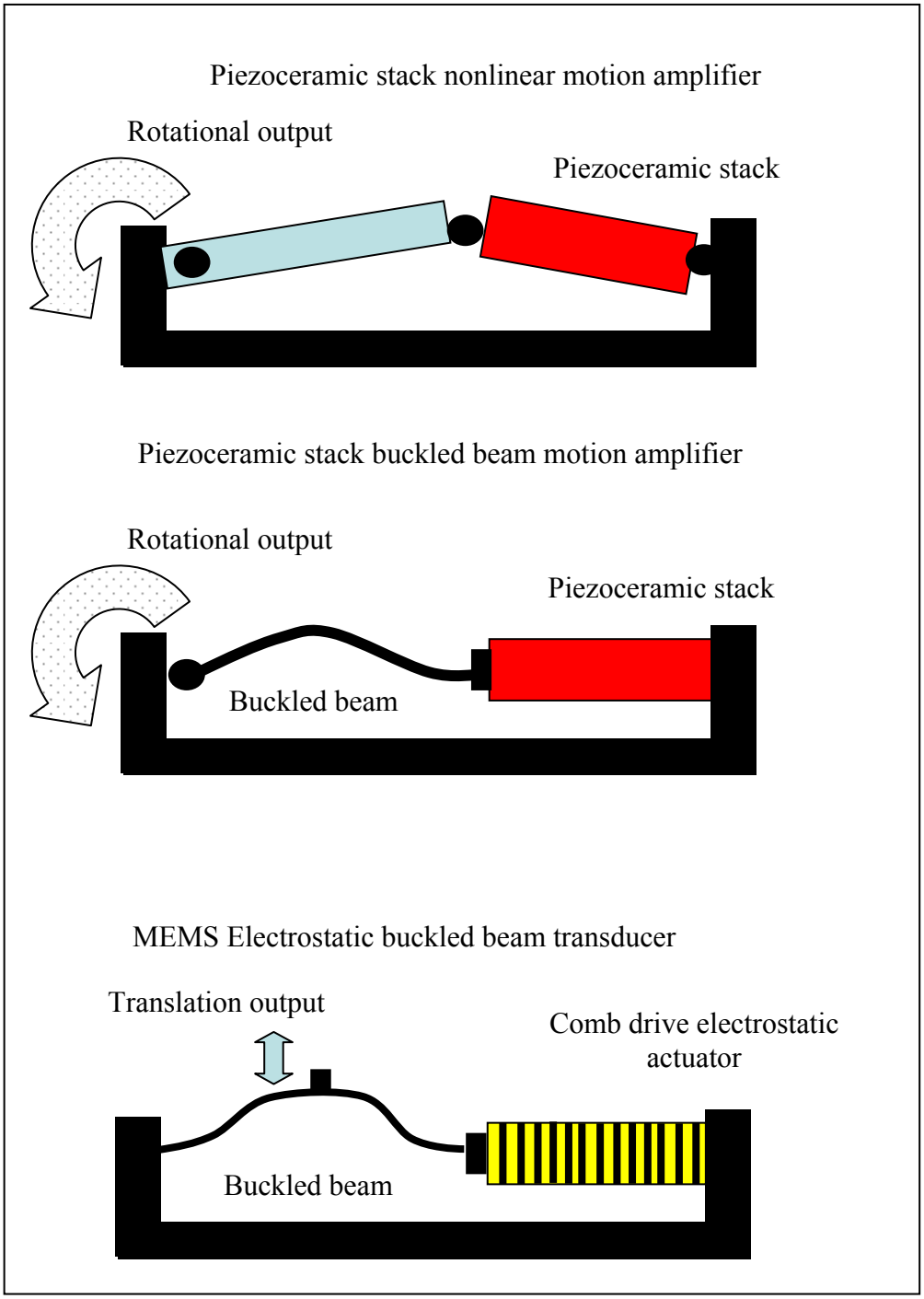

Figure 1.6 Piezoceramic nonlinear motion amplifiers.

Section 1.9 Buckled Beam Behavior

Aristizábal-Ochoa [29] develops an analytical model to describe the behavior of an elastic beam in the post-buckled condition. Behavior of both axial and normal stiffness is analyzed under general end boundary conditions including off center loading and torsion spring boundary conditions. Aristizábal-Ochoa shows that by tailoring the boundary conditions, axial and normal beam stiffness can be tailored from positive to negative stiffness. A subset of this analysis is given by Sun [30].

Saif [31] developed a Micro Electrical Mechanical (MEMS)-based tunable buckled beam transducer where electrically changing the axial load on a beam changes the resonant frequency and normal loading characteristics of the beam. Analysis assumes clamped end conditions and makes small angle approximations, which allow a closed form solution. The beam is fixed at one end and the other end is clamped to preclude rotation but is allowed to translate in the axial direction of the beam. An electrostatic comb actuator is attached to the sliding end of the beam to provide electrically controlled axial force. Relationships between the axial force and normal force, beam stiffness and resonant frequency are developed. The beam operating in the post-buckling regime has two stable states. Saif reports that the beam can be softened so that photon-generated force could change the post-bucked beam from one stable position to the other.

Section 1.10 Enhanced Displacement Actuator Design using Structural Softening Resulting from an Axial Load

The research for this thesis entails investigation of a synthetic jet actuator which utilizes a nonlinear piezoceramic electromechanical mechanism. The concept is a standard piezoceramic bimorph beam element, but an axial, nearly constant-force compression load is used to allow operation of the bimorph in a slightly post buckled state. By carefully controlling the buckling load one can "soften" or lower the bending rigidity seen by the piezoceramic and allows buckling to occur without causing permanent deformation The piezoceramic does not have to overcome the stiffness of the bimorph; very little energy is required to produce large displacement. The buckled beam bimorph or "enhanced displacement bimorph motor" has two stable positions which are shown in Figure 1.7. The piezoceramic applies a moment across the bimorph causing it to switch from one stable position to the other. During this transition the bimorph experiences first a positive stiffness which hinders movement, then the bimorph experiences a negative stiffness which aides movement. The both positive and negative structural stiffness results in a zero total energy requirement. This implies a coupling factor close to 1.

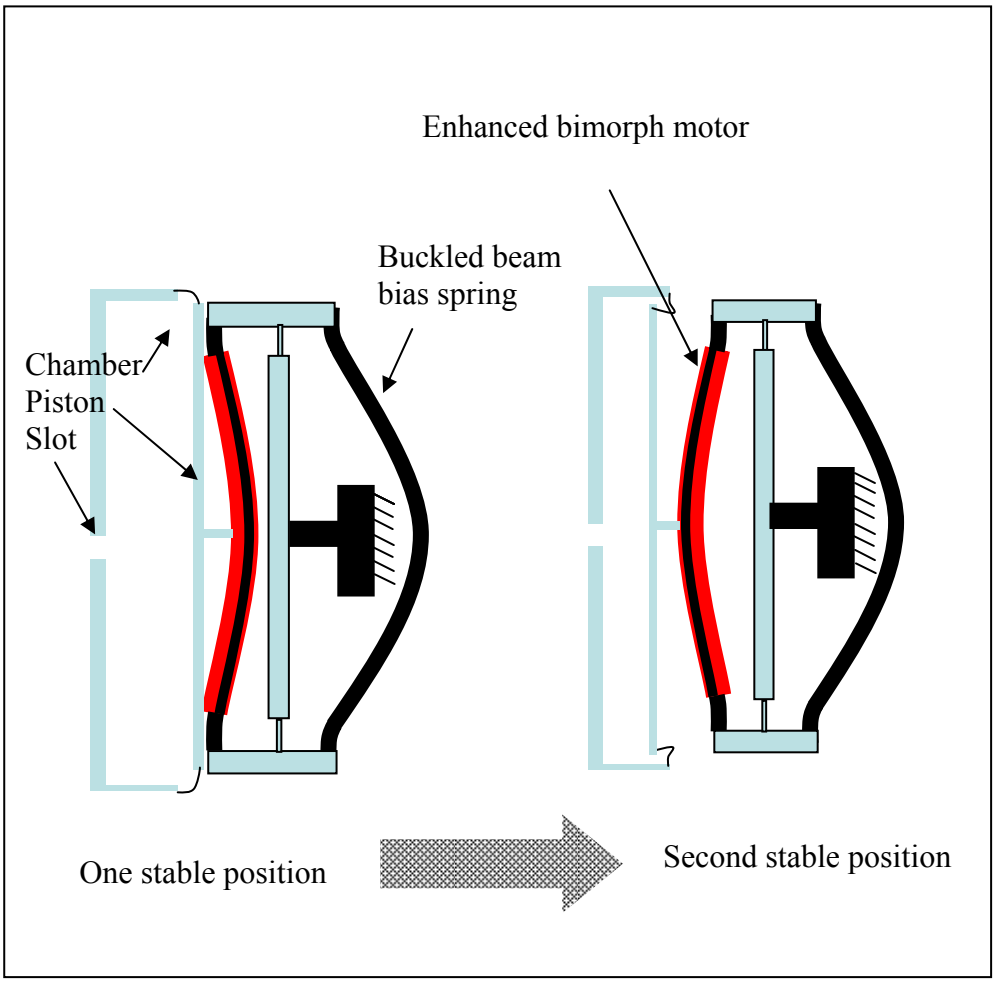

Figure 1.7 Enhanced displacement synthetic jet.

Chapter 2: Synthetic Jet Actuator Modeling

The synthetic jet actuator is modeled in two energy domains. The mechanical domain, where strain energy in the piezoceramic is converted into force and motion of a piston and the fluidic domain, where the force and motion of the piston are converted into air flow in the synthetic jet slot. The piezoceramic material is assumed to have a variable strain displacement that is dependent on applied voltage and a fixed extension modulus. The electrical energy domain is not modeled. An Euler-Bernoulli beam model is used to define the properties of a piezoceramic bimorph actuation element. The beam is operated in a post-buckled condition and is modeled using a large displacement approach presented by Saih [31] and Aristizábal-Ochoa [29]. Motor dynamics are captured by applying Lagrange's Equations to the motor elements, which allow the model to capture the dynamics of the buckled bimorph beam, bias spring, buckled beam and tilt platforms contained in the motor. The model predicts that the enhanced displacement motor will provide up to 14 times the energy into a spring load compared to a conventional pinned-pinned piezo-bimorph.

The fluid model is based on an internal combustion engine model developed by Cadou [32]. The fluid model assumes an isentropic flow process where air is pushed out and drawn into a piston driven chamber. The model includes three states: chamber pressure, chamber temperature and chamber air mass. The three states allow the prediction of air velocity through the slot.

The two energy domain models are coupled to provide an integrated synthetic jet model that can predict synthetic jet performance. The coupled model predicts periodic jet pulse velocities approaching 20 m/sec.

Section 2.1 Piezoceramic Bimorph Beam

The Euler-Bernoulli beam model assumes a beam with its length much larger than its width so that the effects of Poisson's Ratio can be ignored. The model also assumes that strain within the beam is proportional to the distance from the neutral axis of the beam. Each layer's properties are defined as an elastic modulus, width and thickness. Active material layers such as piezoceramic are modeled with an additional property - free strain. Free strain is the physical change in length of the layer per unit length of the material and is specified as a function of electric field.

The beam of interest is a three-layer bimorph beam made up of a passive center layer of uni-axial carbon composite and two active outer layers made from Piezo Fiber Composite (PFC), a piezoceramic fiber composite provided by Advanced Cerametrics Inc. [33]. Figure 2.1 shows a typical beam.

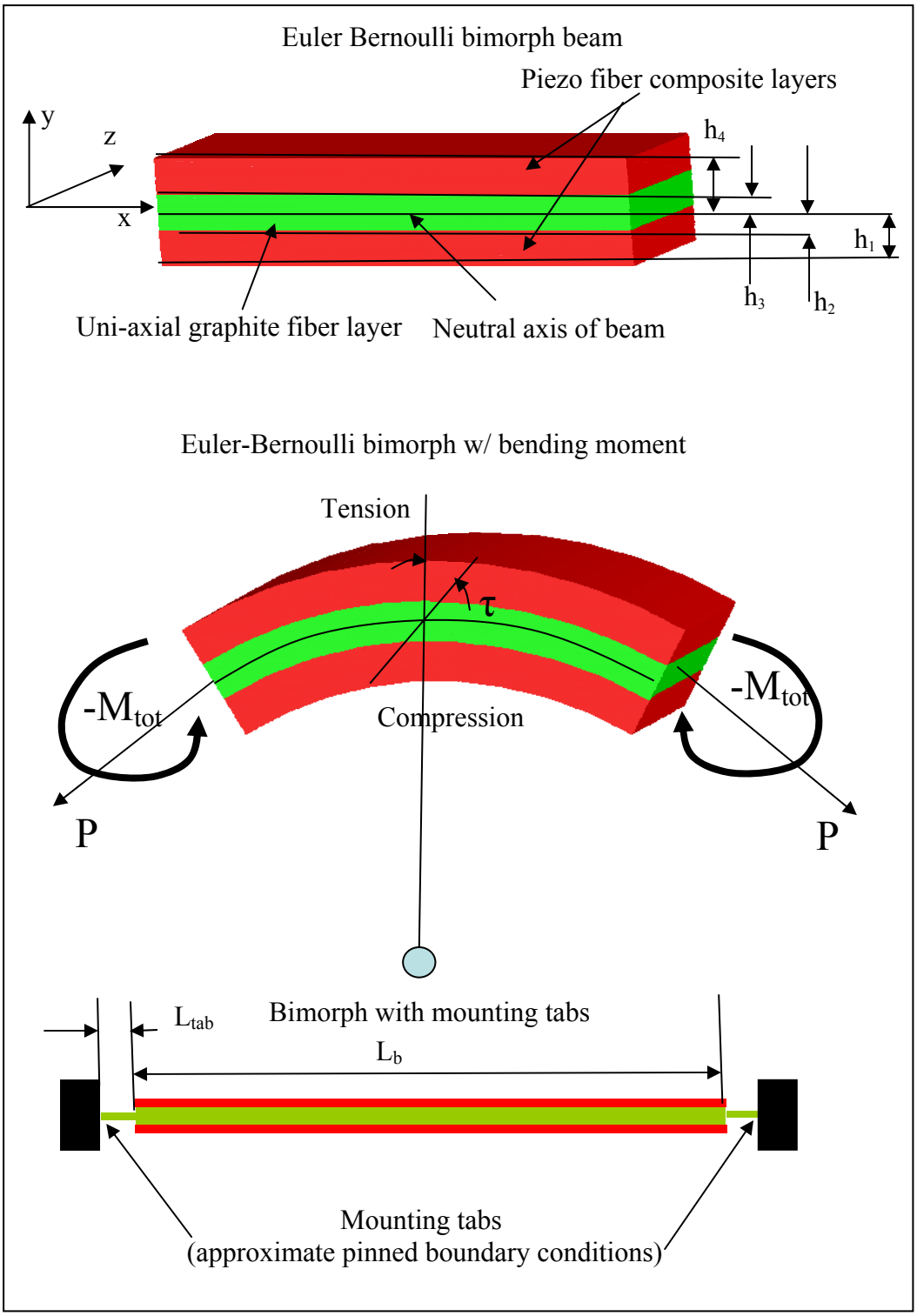

Figure 2.1 Euler-Bernoulli bimorph beam.

Equations 2.1 through 2.4 relate physical beam parameters to the model parameters for a three-layer bimorph beam [34].

$$E_b I_b = 2E_{pfc} b_{pfc} (h_2^{\,3} - h_1^{\,3}) + E_c b_c (h_3^{\,3} - h_2^{\,3}) \quad \textit{(2.1)}$$

$$M_b = 2\Lambda E_{pfc} b_{pfc} (h_2^{\,2} - h_1^{\,2}) \quad \textit{(2.2)}$$

$$\frac{d\Theta}{dx} = -\frac{M_b + M_{ext}}{E_b I_b} \quad \textit{(2.3)}$$

$$\Sigma_y = \frac{(M_b + M_{ext}) * C}{E_b I_b} \quad \textit{(2.4)}$$

$\boldsymbol{E_b I_b}$ is the flexural stiffness of Euler-Bernoulli beam. $\boldsymbol{E_{pfc}}$ is the modulus of the PFC, $\boldsymbol{b_{pfc}}$ is the width of the PFC, $\boldsymbol{h}_1$ through $\boldsymbol{h}_4$ are the distances between the center of the beam and the layers as shown in Figure 2.1. $\boldsymbol{E_c}$ is the uni-axial carbon composite extension modulus along the fiber direction and $\boldsymbol{b_c}$ is the width of the carbon layer. $\boldsymbol{M_b}$ is the moment applied along the beam caused by the PFC and $\boldsymbol{\Lambda}$ is the free strain of the PFC. $\boldsymbol{\tau}$ is the angle the fibers within the beam are deformed, and $\boldsymbol{x}$ is the distance along the beam. $\boldsymbol{M_{tot}}$ is the total moment on the beam including the PFC-induced moment, and $\boldsymbol{\Sigma_z}$ is the strain on the beam as a function of distance from the center of the beam. $\boldsymbol{C}$ is an arbitrary distance from the beam center but is contained in the beam.

A pinned end condition is chosen for the end conditions of the bimorph. The pinned condition allows a single segment PFC to excite the first buckling mode while providing the lowest buckling force of any end condition. The pinned condition is approximated by a small thickness tab. ***Equation 2.5*** shows the relationship between the tab rotational stiffness and the bimorph stiffness.

$$\frac{K_{tab}}{K_b} = \frac{E_{tab} I_{tab}}{E_b I_b} \frac{L_b}{L_{tab}} \qquad (2.5)$$

where K_{tab} is the rotational stiffness of the tab, K_b is the rotational stiffness of the bimorph, E_{tab} is the modulus of the tab, I_{tab} is the area moment of inertia of the tab, L_b is the length of the bimorph and L_{tab} is the length of the tab. The bimorph beam boundary condition can be assumed to be a pinned condition when K_{tab} is much smaller than K_b.

The partial differential equation relating applied load and moment to the beam defection and slope is given in ***Equation 2.6***.

$$\frac{\partial^2}{\partial x^2}\left(E_b I_b \frac{\partial^2 y}{\partial x^2}\right) + f(t,x) + \frac{\partial^2 M(t,x)}{\partial x^2} + \frac{\partial^2 P^* y}{\partial x^2} = \rho(x)\frac{\partial^2 y}{\partial t^2} \qquad (2.6)$$
$$y(0) = y(L) = 0$$
$$\frac{\partial^2 y(0)}{\partial x^2} = \frac{\partial^2 y(L)}{\partial x^2} = 0$$

$f(t,x)$ is the force loading on the beam, $M(t,x)$ is the applied moment on the beam, $\rho(x)$ is the mass density of the beam and $y(t,x)$ is the vertical displacement of the beam from the centerline. P is the tension load on the beam. A pinned-pinned boundary condition is specified by setting the displacement and moment equal to zero at each end of the bimorph beam.

Section 2.2 Buckled Beam

Buckling phenomena is often thought of in terms of sudden structural failure but analysis shows that under most conditions, the axial stiffness of the buckled member is reduced dramatically and remains positive [30, 31]. Figure 2.2 illustrates important

properties of a buckled beam with pinned end conditions.

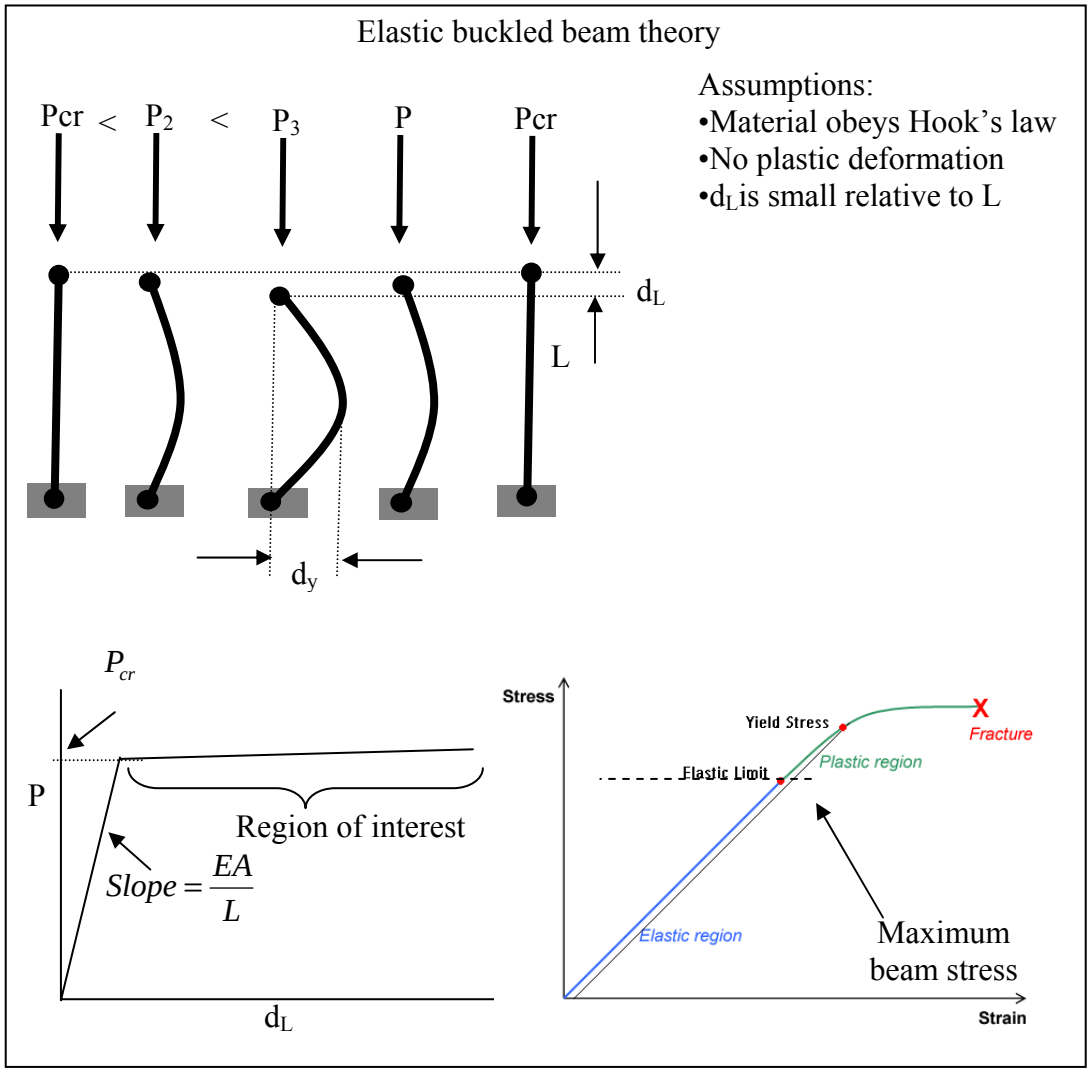

Figure 2.2 Buckled beam assumptions. Upper: Buckled beam sequence.
Lower Left: Buckled beam full region stress vs. strain.
Lower Right: Beam material stress vs. strain.

As long as the stress in the beam remains within the elastic region, buckling deformation is reversible. The axial load-displacement relationship is generally nonlinear with loads above the critical buckling load but for small displacements this relationship can be approximated by a constant stiffness. The relationship between the normal displacement of the center of the beam and axial displacements can be approximated by a quadratic relationship.

For this research, the buckled beam concept is applied to a PFC based bimorph and an un-powered PFC bimorph that operates as a bias spring. The application of an axial load, ***P,*** changes the stiffness properties of the bimorph. A tension load increases the flexural stiffness while a compressive load decreases the stiffness. This phenomenon is exploited by Lesieutre [27] to increase the piezoelectric coupling coefficient of a bimorph. At a critical load, P_{cr}, the bimorph exhibits zero flexural stiffness and a coupling coefficient of one. The straight condition of the beam becomes unstable as P is increased beyond P_{cr} and the bimorph takes on one of the two stable deformed positions, deflected to the left or right of the neutral position. See Figure 2.3.

Buckling mode shapes can be determined for any boundary condition by solving ***Equation 2.7a*** [30]. The solutions will be of the form shown in ***Equation 2.7b***.

$$\frac{\partial^2}{\partial x^2}\left(E_b I_b \frac{\partial^2 y}{\partial x^2}\right) + \frac{\partial^2 P^* y}{\partial x^2} = 0 \qquad \textbf{(2.7a)}$$

$$y(x) = A\sin(\omega x) + B\cos(\omega x) + Cx + D \qquad \textbf{(2.7b)}$$

Boundary conditions of the beam determine constants ω, A, B, C and D. A beam with pinned boundary conditions at both ends will have a nonzero load-dependent value for the constant A and values of zero for constants B, C, and D.

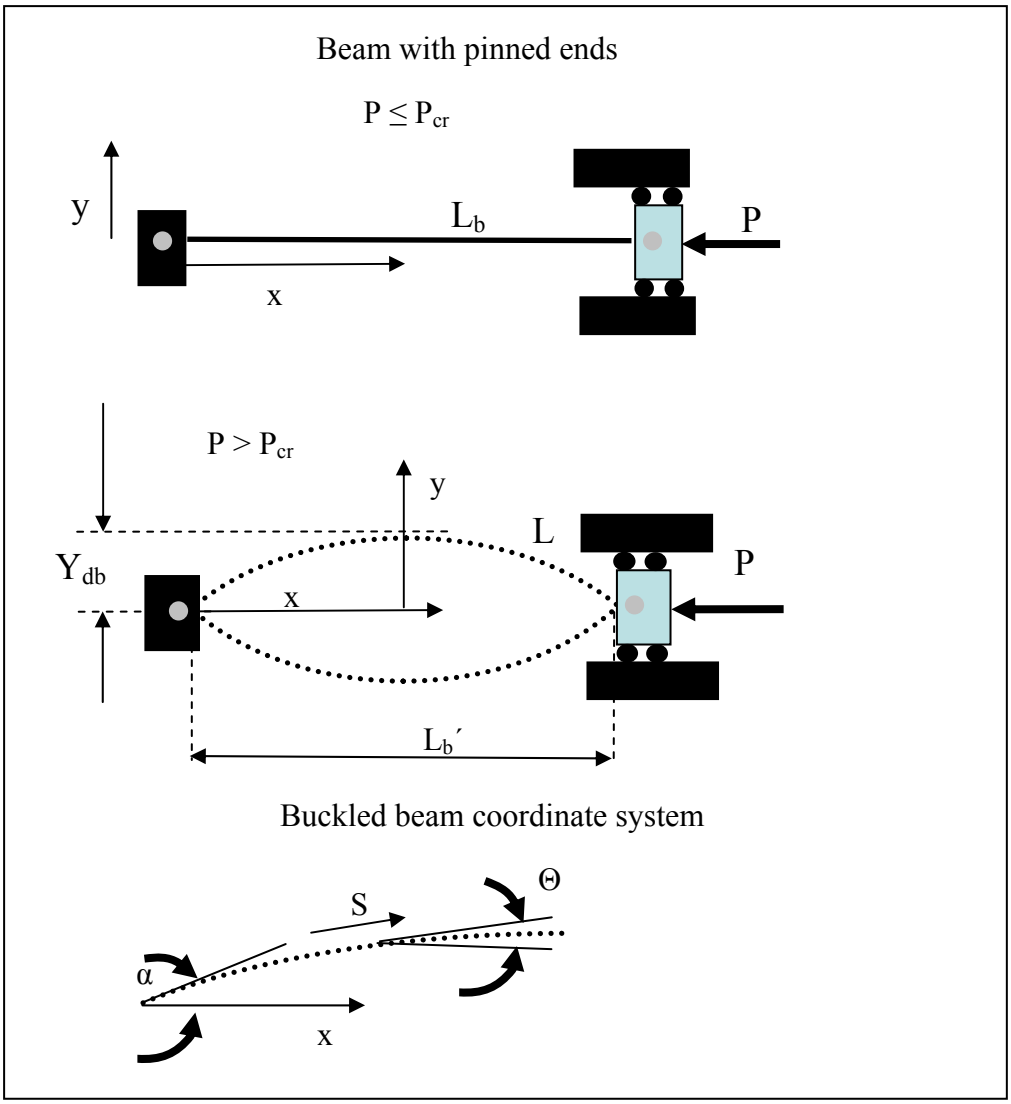

Figure 2.3 Beam with compressive axial load and pinned ends.

Equations 2.7 predicts the buckling mode shape and critical buckling load; however, it does not allow for determination of the magnitude of the constant ***A***. The work of Aristizábal-Ochoa [29], Sun [30] and Saih [31] will be used to develop the relationships between applied axial force and moment and the resulting displacements as a function of axial load for beams operating above the buckling load.

The motor is modeled as a buckled beam, PFC bimorph with the following properties; E_bI_b, the unit rotational stiffness of the bimorph, L_b, the length of the bimorph and ρ_b, the linear mass density of the bimorph. The model also includes a bias spring comprised of a second buckled beam with properties E_bI_{bs}, L_{bs} and ρ_{bs}. The two beams are connected by two rotational links with properties I_b, the mass moment of inertia and r, the distance between the pivot and the end of the beams. The bimorph beam center displacement is Y_{db} and the force applied to the bimorph beam center is Fa. The two beams are assumed to be attached at the same distance from the pivot point. The piston is modeled by a mass, m_p. A concept drawing of the Enhanced Displacement (ED) motor is shown in Figure 2.4.

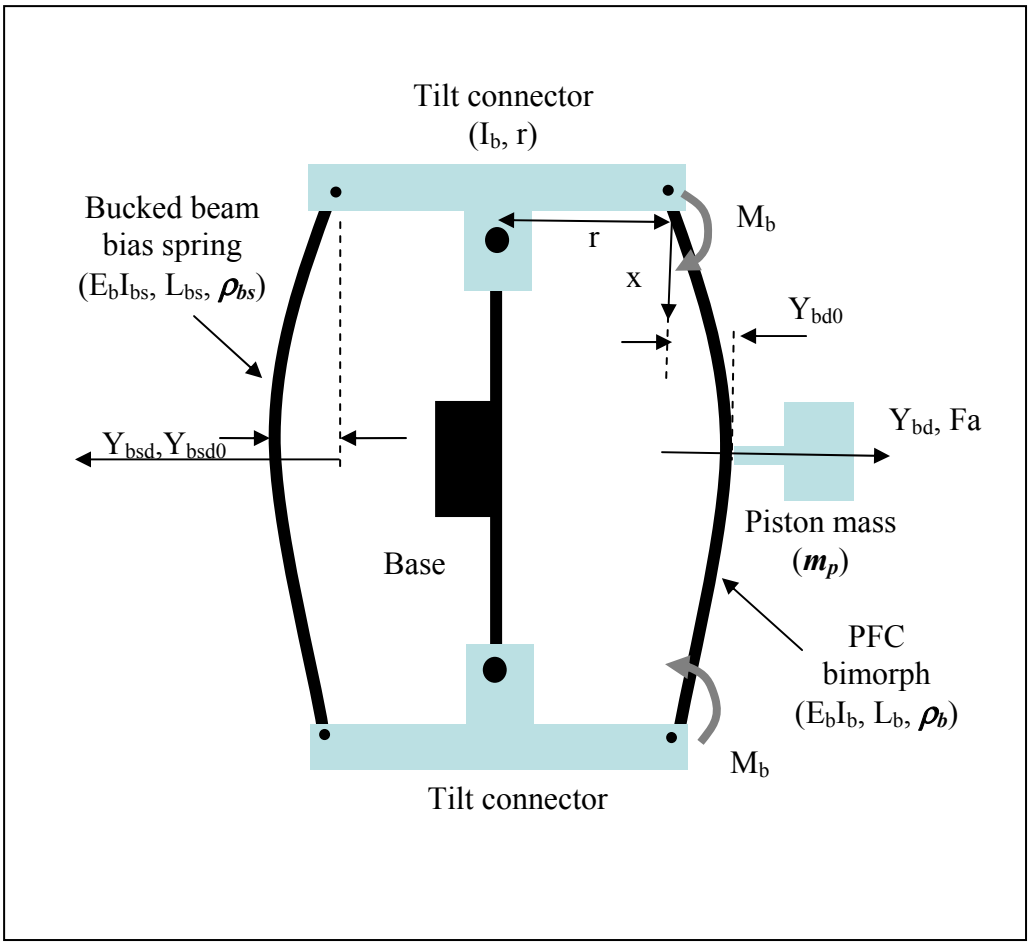

Figure 2.4 Enhanced displacement motor.

The motor is connected to the base at the center of a tie-rod and the output is taken at the piston.

The model will be developed by relating beam-applied forces and moments to beam displacement then solving for the equations of motion using Lagrange's Equations. We will assume the following properties:

- Only the first buckling mode will exist. The buckled shape of the pinned-pinned beam can be defined as a sine function defined between 0 and π. Saif [31]

supports this assumption with test data. The beam shape and buckling load are defined in ***Equations 2.8a and 2.8b*** [30].

$$Y(x) = Y_d \, Sin(\pi x / L) \qquad \textbf{(2.8a)}$$

$$P_{cr} = \pi^2 \frac{EI}{L^2} \qquad \textbf{(2.8b)}$$

- All materials behave according to Hook's Law.
- The axial deformation, δL_e, due to the applied compressive load before buckling is much smaller than L. Assume $L - dL_e \approx L$
- The slope of the deformed beam is much less than unity. This allows the distance integral to be approximated by a binomial expansion.
- The PFCs will apply a bending moment to each end of the beam when energized. The magnitude of the bending moment is M_p.

A large displacement elastic approach given by Sun [30] is used to develop the relationship between axial load and beam displacement for a pinned-pinned buckled beam. Alpha, α, is defined as the angle of the beam at the pinned end, $\Theta(x)$, the angle along the beam and P the axial load on the beam. ***Equations 2.9 - 2.11*** relate axial load P to initial angle α and beam mid-span displacement Y_d.

$$\beta = \sin\left(\frac{\alpha}{2}\right) \qquad \textbf{(2.9)}$$

$$\frac{P}{P_{crt}} = \frac{4}{\pi^2} \int_0^{\pi/2} \frac{\delta\phi}{\sqrt{\left(1-\beta^2 \sin^2(\phi)\right)}} \qquad \textbf{(2.10)}$$

$$Y_d = \frac{2\beta}{L} \qquad \textbf{(2.11)}$$

Equation 2.10 contains an elliptical function that must be solved numerically; however, for small α, the elliptical function in equation 2.10 can be approximated by the first term of a binomial expansion leading to ***Equations 2.12-13*** [31].

$$dl = \frac{\pi^2 Y_d^{\,2}}{4L} \qquad \textit{(2.12)}$$

$$\frac{P}{P_{cr}} = 1 + \frac{\pi^2 Y_d^{\,2}}{8L^2} + HOT \qquad \textit{(2.13)}$$

where ***dl*** is the change in length of the beam due to the axial load ***P*** when ***P*** is greater then $\boldsymbol{P_{cr}}$. HOT (higher order terms) contain forth and higher order terms of $\boldsymbol{Y_d}$ and is ignored since we will only consider values of $\boldsymbol{Y_d/L < 0.1}$.

Following the method of Lagrange, a single degree of freedom system is defined with respect to a single generalized coordinate $\boldsymbol{Y_{bd}}$, the distance the center of the bimorph is offset from the beam pinned ends. Using this coordinate system and Equation 2.12**,** the rotation angle of the tilt connector, $\boldsymbol{\Theta_t}$ is defined as a function of $\boldsymbol{Y_d}$ in ***Equation 2.14***.

$$\Theta_t = \frac{\pi^2 Y_{bd}^{\,2}}{r 8 L_b} \qquad \textit{(2.14)}$$

Equation 2.14 takes into account that only half of the displacement is applied to each of the two tilt connectors.

The proper preload of the motor is set by deforming the bimorph beam by Y_{bd00} then attaching it to the motor. When released the buckled bimorph and bias beam will have a steady state displacements of Y_{bd0} and Y_{bsd0}. ***Equation 2.15*** relates the bimorph steady state position to axial loads on both the bimorph and bias beam and steady state position of bias beamy

$$P_{bd0} = P_{cr}(1 + \frac{\pi^2 Y^2_{bd0}}{8L_b^2}) \qquad (2.15)$$

$$Y_{bsd0} = \sqrt{\left(\frac{P_{bd0}}{P_{crbs}} - 1\right)\frac{8L^2_{bs}}{\pi^2}}$$

where P_{bd0} is the axial load required to produce a desired steady state displacement Y_{bd0} of the bimorph. P_{crtb} is the buckling load of the bias spring beam and L_{bs} is the length of the bias spring beam. The displacement of the bias spring beam center Y_{bsd} is related to Y_{bd} by ***Equation 2.16***.

$$Y_{bsd} = \sqrt{Y^2_{bsd0} - \frac{L_{bs}}{L_b}\left(Y_{bd}^2\right)} \qquad (2.16)$$

To set an initial bimorph displacement, Y_{bd0}, one must determine a corresponding Y_{bsd0}. In practice, this is accomplished by adjusting the distance between the two tilt platforms until the desired offset of the bimorph is achieved. In the model, Y_{bsd0} is determined by iteration of Y_{bsd00} until the desired Y_{bd0} is achieved.

The potential and kinetic energy of the system in terms of the generalized coordinate Y_{bd} is calculated. Large displacement assumptions are used; hence, the distance between the two pinned ends of each beam can no longer be approximated by L. A dummy variable s is introduced that ranges from 0 to L and equations are used to

relate ***s*** to ***L'*** the shortened distance between the beam ends. The position along the beam can be related to Y_{bd} by the mode shape using ***Equation 2.17***. The curvature in the beam is related to the position of the beam by the second derivative of the displacement in the y direction with respect to the distance along the beam, ***s***. ***Equation 2.18*** relates beam curvature to displacement.

$$Y_d(s) = Y_d * \sin(\omega s) \qquad \textit{(2.17)}$$

$$\varepsilon = -\omega^2 Y_d * \sin(\omega s) \qquad \textit{(2.18)}$$

where ε is the curvature of the beam.

The potential energy of the bimorph and the bias spring is calculated using ***Equations 2.19 and 2.20.***

$$L_b' = L_b - \frac{\pi^2 {Y_{bd}}^2}{4 * L_b} \qquad \textit{(2.19)}$$

$$\omega_b = \frac{\pi}{L_b'}$$

$$P_b(\varepsilon) = P_{crb}\left(1 + \frac{\pi^2 \frac{\varepsilon^2}{{\omega_b}^4}}{8{L_b}^2}\right)$$

$$\Phi_b = \int_0^{L_b'} \int_0^{\left(-\omega_b^2 Y_{bd} \sin(\omega_b * s)\right)} \left(-E_b I_b \varepsilon + P_b(\varepsilon) * \frac{\varepsilon}{{\omega_b}^2}\right) d\varepsilon ds$$

$$L_{bs}^{'} = L_{bs} - \frac{\pi^2 Y_{bsd}^{\ 2}}{4 * L_{bs}} \qquad \textbf{(2.20)}$$

$$\omega_{bs} = \frac{\pi}{L_{bs}^{'}}$$

$$P_{bs}(\varepsilon) = P_{crbs}\left(1 + \frac{\pi^2 \frac{\varepsilon^{\ 2}}{\omega_{bs}^{\ 4}}}{8 L_{bs}^{\ 2}}\right)$$

$$\Phi_{bs} = \int_0^{L_{bs}^{'}} \int_0^{\left(-\omega_{bs}^{\ 2} Y_{bsd} \sin(\omega_{bs} * s)\right)} \left(-E_b I_{bs} \varepsilon + P_{bs}(\varepsilon) * \frac{\varepsilon}{\omega_{bs}^{\ 2}}\right) d\varepsilon \, ds$$

where Φ_b and Φ_{bs} are the potential energy of the bimorph beam and bias spring beams. Note that $\boldsymbol{Y_{bsd}}$ is a function of $\boldsymbol{Y_{bd}}$ and upon substitution; Equations 2.19 and 2.20 are a function of $\boldsymbol{Y_{bd}}$

Next, an expression for the kinetic energy of the system $\boldsymbol{\Phi_d}$ is developed. The four elements that store kinetic energy are the bimorph, bias spring, tilt platforms and piston mass. ***Equation 2.21*** shows the expression for the kinetic energy of the system.

$$\Phi_d = \frac{\rho_b}{2} \int_0^{L_b^{'}} \partial_t \left(Y_{bd} * \sin(\omega_b s)\right)^2 ds + \frac{\rho_{bs}}{2} \int_0^{L_{bs}^{'}} \partial_t \left(Y_{bs} * \sin(\omega_{bs} s)\right)^2 ds + I_b * \partial_t (\theta_t)^2 +$$

$$\frac{m_p}{2} \partial_t (Y_{bd})^2 \qquad \textbf{(2.21)}$$

where $\boldsymbol{\Phi_d}$ is the kinetic energy in the motor. Again, appropriate substitutions for $\boldsymbol{Y_{bs}}$ and $\boldsymbol{\Theta_t}$ are required before integration.

The non-conservative forces acting on the system are the force applied to the piston, ***Fa*** and the moments applied by the bimorph, M_p. ***Fa*** is collinear with the generalized coordinate Y_{bd} and is added directly. M_p applies a moment to each end of the bimorph. An equivalent force along Y_{bd} is calculated by equating the static displacement of a pinned-pinned beam with a center force and the displacement induced by an applied moment M_p [36]. A damping term $\zeta * dY_d/dt$, is added to account for damping within the system. The expression for the generalized forces is given in ***Equation 2.22***.

$$Q = Fa - \frac{6M_p}{L} + \xi \frac{\delta Y_{bd}}{\delta t} \qquad \textit{(2.22)}$$

The total energy in the system is expressed by ***Equation 2.23***.

$$\Phi_b + \Phi_{bs} + \Phi_d = Q \qquad \textit{(2.23)}$$

The method of Lagrange evaluates Equation 2.23 with ***Equation 2.24*** to get:

$$\frac{\partial}{\partial t}\left(\frac{\partial \Phi_d}{\partial \dot{Y}_{bd}}\right) - \frac{\partial \Phi_d}{\partial Y_{bd}} + \frac{\partial(\Phi_b + \Phi_{bs})}{\partial Y_{bd}} = Q \qquad \textit{(2.24)}$$

Equation 2.24 is a second order ordinary differential equation of $Y_{bd}(t)$. This is solved for the second derivative of $Y_{bd}(t)$ with respect to time and is shown in Appendix I. Equation 2.24 does not have a closed form solution so it must be solved numerically.

Section 2.3 Normalized Beam Example

Given the ED motor topology shown in Figure 2.4, a normalized motor model with the following properties is defined. The motor forces are normalized by the bimorph buckling load, $P_{cr.}$ The motor lengths are normalized by bimorph length L_b which leads to a normalized E_bI_b equal to $1/\pi^2$. The mass densities, ρ_b and ρ_{bs} are set to 1. An initial offset of the beam, Y_{bd0} , is arbitrarily set to 1/10 and then the initial beam compression Y_{bd00} is found. The time derivatives shown in Equation 2.24 are set to zero and the equation is solved for Fa, the force applied to the motor from the load.

Subsection 2.3.1 Reference Motor

A reference motor is defined as an unbuckled beam with pinned end conditions as shown in Figure 2.5. Also shown in Figure 2.5, is a load line for the reference motor. The load line defines the quasi-static displacement behavior of the motor as a function of load force applied to the motor. A load line is a measure of the stiffness, i.e. and force displacement relationship of the motor under different loads. For a given applied voltage, the bimorph beam displacement will lie along the load line. Points of interest are the blocked force where the load on the motor is high enough to restrain the motor from any movement, the free displacement, where the motor is unloaded and maximum displacement occurs and the optimal load and displacement were maximum energy transfer occurs. Note that bimorph motor force and the load applied to bimorph motor are equal and opposite.

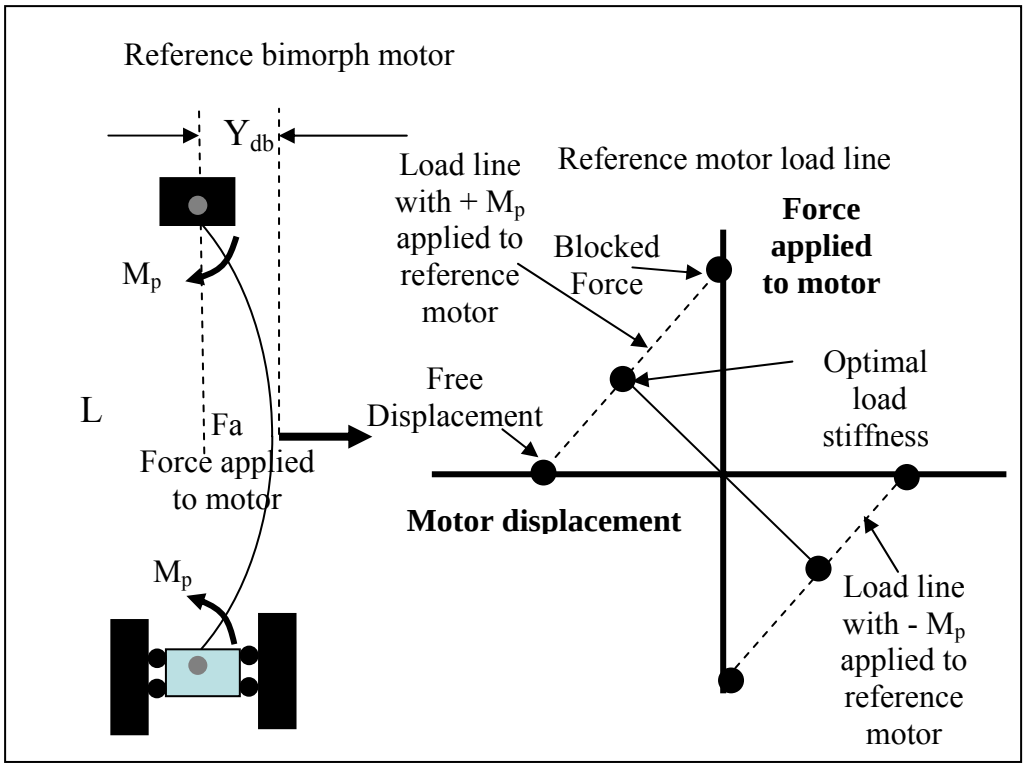

Figure 2.5 Reference motor and optimal load. Left: Reference motor drawing. Right: Reference motor and optimal load diagram.

Since the motor does not have an axial load applied it has one stable position corresponding to a straight condition. ***Equations 2.25*** and ***2.26*** respectively list the relationships between displacement and applied force R'_{nom} and displacement Y'_{bd} and moment M'_{nom} for a non-axially loaded pinned-pinned bimorph beam.

$$R'_{nom} = \frac{48Y'_{bd}}{\pi^2} \qquad (2.25)$$

$$M'_{nom} = \frac{8Y'_{bd}}{\pi^2} \qquad (2.26)$$

The force and moment were calculated using a static beam approach [36].

Subsection 2.3.2 Enhanced Displacement Motor Stiffness Properties

Figure 2.6 shows the force displacement relationship of the enhanced bimorph motor operating with the applied piezoceramic induced moment, M_p, set to zero. This is obtained by assuming that the voltage on the PFCs is zero. In this case the force from an external load is considered and the resulting displacement-force relationship is shown. Note that because the force applied by the load and the force applied by the motor must be equal and of opposite sign, this force will produce the same curve as the load line curve that is based on the force applied to the load. The ED motor has two positions that are stable at two positions, $Y_{bd0} = \pm 0.05$. Note: technically the motor is stable at Y_{bd} is zero, but any disturbance will cause the motor to move to one of the two stable positions. This unconventional force-displacement relationship can be used to develop ED motor relationships between motor displacement, Y_{bd} and applied or load force, Fa while the PFCs voltage is zero. Motor position, Y_{bd} will change between stable positions when a normalized force of 0.00425 is applied.

Appling Equations 2.25 and 2.26, The normalized force, R'_{nom}, required to displace the center position, Y'_{bd} of the reference motor to 0.05 is $2.4/\pi^2$ or 0.243. The corresponding bending moment, M'_{nom} , required to move the reference is $0.8/\pi^2$ or 0.025. The non-actuated stiffness of the ED motor is reduced by more than a factor of 100 compared with the reference motor. A property of the enhanced displacement motor is that the total energy required to move the motor from one stable position to the other is negligible compared to an unbuckled beam where an order of magnitude

more energy is required to displace the beam.

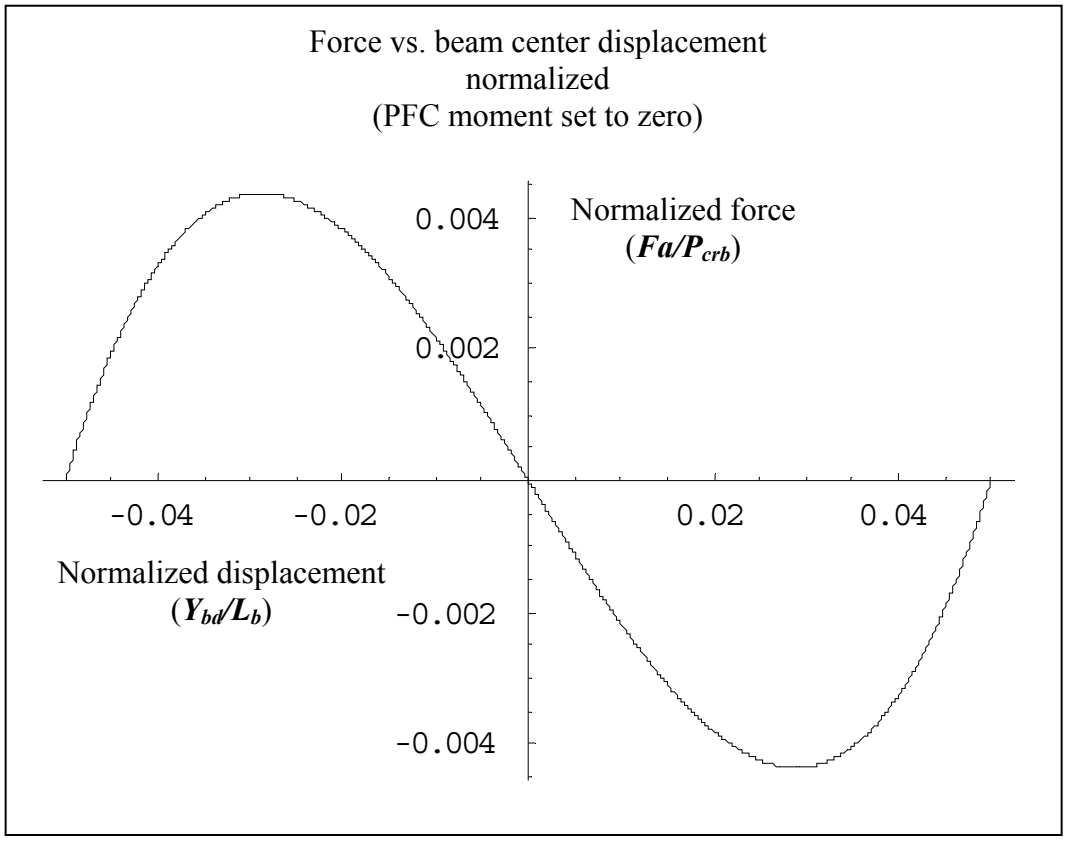

Figure 2.6 Normalized applied motor force vs. beam displacement with no applied PFC moment.

Subsection 2.3.3 Enhanced Displacement Motor with Piezoceramic-Induced Moment

In this section, the effect of using the PFCs to apply a bending moment to the bimorph within the ED motor is investigated. See the solution to Equation 2.22 for the quasi-static relationship between motor force and applied moment. Application of of moment with a magnitude above 0.0007 or a corresponding 0.00425 load changes the ED motor load line from a bi-stable load line to a single stable position load line with the zero load position offset from the origin. This can be seen in Figure 2.6 as the force resulting from the moment will overcome the load barrier between stable

positions. The optimal spring load for maximum energy transfer will be considerably different than the optimal energy transfer load for the reference motor. These differences are illustrated in Figure 2.7.

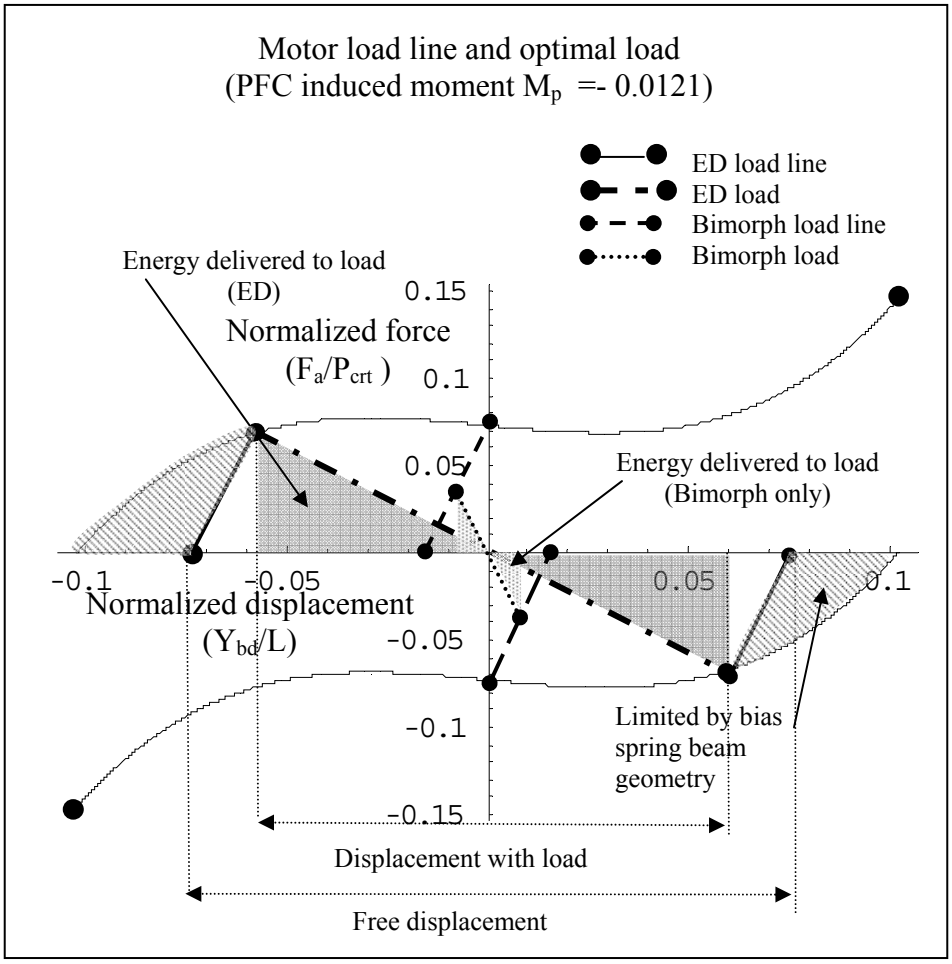

Figure 2.7 Comparison of elastic optimal loads for the enhanced displacement motor and reference motor.

The ED motor is assumed to have an initial displacement, Y_{bd0} of 0.05 and, M_p, the moment applied to the bimorph is set to 0.0121. This is the moment required to deform the reference motor to a normalized position of -0.0015. The ED motor bias spring beam length, L_{bs}, is set to $1.05L_b$ and E_bI_{bs} is set so that both beams have the same buckling load, P_{cr}. The plot shown in Figure 2.6 has two regions of increased stiffness. These regions represent where the bimorph is displaced so the bias beam is

fully extended and no longer supplies a buckling load to the bimorph. In these regions, the ED motor will exhibit the stiffness of the reference motor. The Lagrange modeling approach does not lend it self to discontinuities so this phenomenon is not modeled in the ED motor ODE solution but is included in Figure 2.7. Optimal elastic load lines for both the ED motor and the reference motor are shown. Areas between the regions where the bias beam is straight are modeled by setting the time derivatives $\boldsymbol{Y_{bd}}$ in the ED motor ODE to zeros and solving for the applied force $\boldsymbol{Fa}$ as a function of $\boldsymbol{Y_{bd}}$ while $\boldsymbol{Mp}$ is set to normalized moment of ±0.0121 resulting in the upper curve for a negative moment and the lower curve for a positive moment.

A spring load is characterized by a line with the slope equal to the stiffness of the load and intersecting at the origin. This spring load characterization will be called the R-Line for the reference motor load and ED-Line for the ED motor load. Note that the PFCs produce both positive and negative moment so the energy delivered to the load is twice the area of a single triangle.

An optimal load will have a slope or stiffness that will maximize the energy transfer from the motor to the load. The optimal R-Line load for the reference motor will have stiffness or slope equal and opposite to the reference motor load line slope or stiffness [22]. This will maximize the area formed under the R-Line and the R-Line intersection with the reference motor load line. Note this area under R-Line is a measure of energy per cycle of the motor transferred to the load.

The optimal ED-Line will have a slope that maximizes the area under the triangle formed by the ED-Load and its intersection with the ED motor load line. The largest area triangle is formed when the ED-Line intersects the ED load line the intersection of the bias beam slope and the ODE generated load line.

A Figure of Merit (***FoM***) is defined in ***Equation 2.27.***

$$FoM = \frac{\Phi_{ED}}{\Phi_{rm}} \qquad \textit{(2.27)}$$

Where $\boldsymbol{\Phi_{ED}}$ is the ED motor energy transferred to an optimal load and $\boldsymbol{\Phi_{rm}}$ is the reference motor energy transferred to a optimal load. Table 2.1 compares the two motor cases.

Table 2.1 Normalized enhanced displacement and non-axial loaded motor comparison

Characteristics	Enhanced Displacement Motor	Reference Motor
Free Displacement	0.071	0.015
Blocked Force	0.06	0.06
Optimal Displacement	0.057	0.0075
Optimal Force	0.06	0.03
Figure of Merit	14	1

Subsection 2.3.4 Enhanced Displacement Motor with Constant Force Load

The load experienced by the ED motor when driving a synthetic jet actuator is a combination of a spring type load and a constant pressure load. A fluid pump or constant pressure load line analysis is presented. The motor works against an incompressible fluid with a constant pressure like that which is developed by a check valve. This cycle is shown in Figure 2.8.

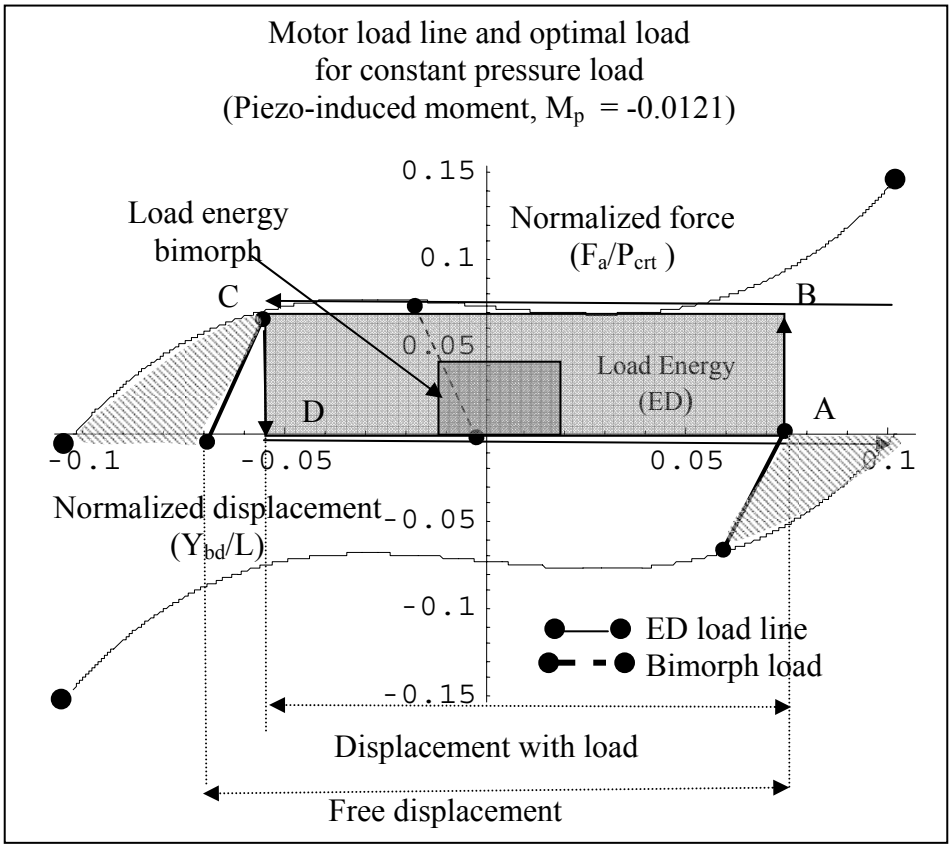

Figure 2.8 ED motor load line and bimorph load line with constant pressure loads.

The cycle begins when the motor applies a force until it overcomes the constant force generated by the pressurized fluid shown in segment AB. During segment BC, the motor pushes the fluid into a chamber at constant pressure. During segments C D the

motor reduces its force to zero as a check valve keeps the fluid from pushing on the motor. During the final segment, DA, the motor returns to the initial starting point without load. Table 2.2 summarizes key properties of this load case.

Table 2.2 Normalized enhanced displacement and non-axial loaded motor comparison.

Characteristics	Enhanced Displacement Motor	Non-Axially Loaded Bimorph
Free Displacement	0.13	0.015
Blocked Force	0.06	0.06
Optimal Displacement	0.13	0.0075
Optimal Force	0.06	0.03
Figure of Merit	11	1

Motor power supplied to the load is also an important characteristic. A high-energy per cycle motor may not be superior to a small-energy per cycle motor if the small-energy per cycle motor can produce more energy per unit time than the high-energy motor.

The results of a normalized dynamic simulation of both the ED and reference motors are shown in Figure 2.9.

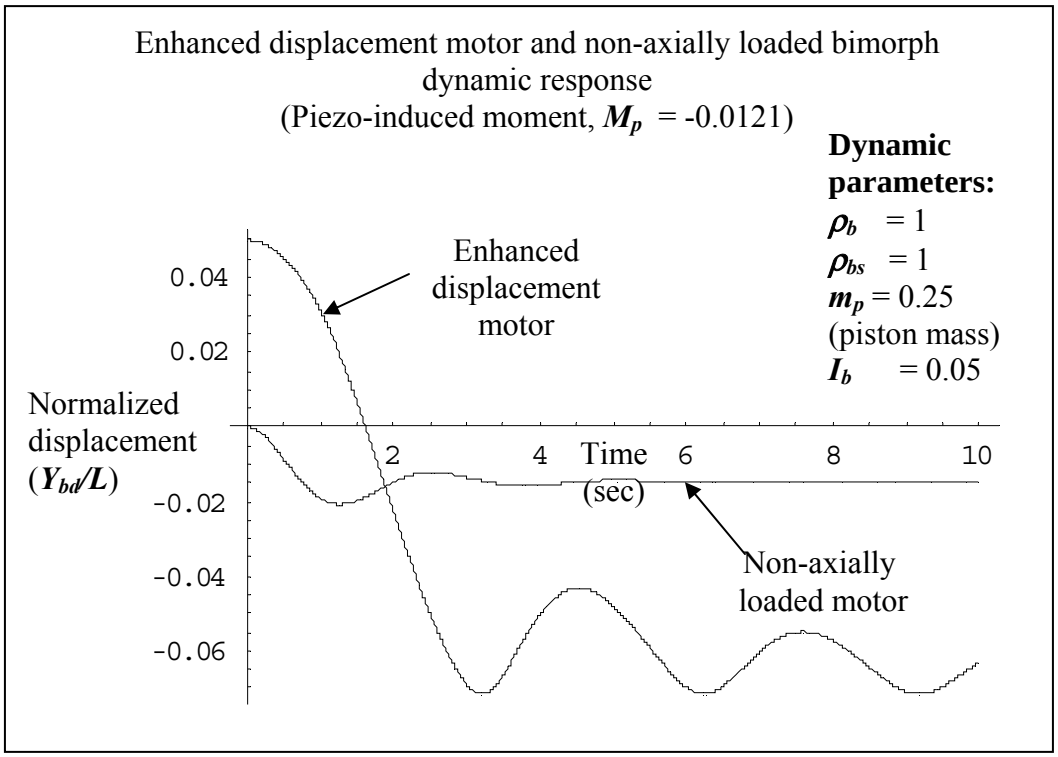

Figure 2.9 Enhanced displacement and reference motor dynamic response.

The initial position of the ED motor was set to 00.5 m/m; the positive zero moment steady state position. The reference motor position is zero and a normalized PFC moment of 0.0121 is applied. Both motors are driving a 0.25 Kg/Kg piston mass (m_p). Both the bimorph (ρ_b) and the bias beam (ρ_{bs}) mass densities are set to 1. The tilt connector moment of inertia (I_b) is set to 0.05 Kg-m^2/Kg-m^2 . The damping coefficient ζ is set to 1.05 for both motors.

The enhanced displacement motor has a 90% rise time of 2.5 seconds and the reference motor has a 90% rise time of 0.9 second or 2.8 times as fast. From these rise times and corresponding ***FoM***s, we can conclude that the enhanced displacement motor will produce significantly more power than the non-axially loaded bimorph under both the spring load and constant load cases.

Model verification of the enhanced displacement motor is difficult without test data, however, verification of the Lagrange approach can be accomplished by comparing model produced properties of a non-axially loaded pinned-pinned bimorph with published properties [36, 37]. Beam properties of stiffness, moment induced deflection and first mode natural frequency are compared and found to be similar. Table 2.3 shows a comparison between model and published results.

Table 2.3 Comparison of pinned-pinned beam properties with model and published properties.

Pinned-Pinned Beam Model Comparison		
Properties	Model	Published
Center Stiffness	$\frac{E_b I_b \pi^4}{2L^3}$ or $\left[\frac{48.7 E_b I_b}{L^3}\right]$	$\frac{E_b I_b 48}{L^3}$ [36]
Displacement with Applied Moment $\boldsymbol{M_p}$	$\frac{M_p 12 L^2}{\pi^4 E_b I_b}$ or $\left[\frac{M_p L^2}{8.1 E_b I_b}\right]$	$\frac{M_p L^2}{8 E_b I_b}$ [36]
Natural Frequency (First Mode)	$\pi^2 \sqrt{\frac{E_b I_b}{\rho_b L^4}}$	$\pi^2 \sqrt{\frac{E_b I_b}{\rho_b L^4}}$ [37]

The differences in modeled and published static beam properties can be attributed to the use of a sine function used in the model vs. the exact solution being a second order polynomial for the published values. These comparisons partially validate the Lagrange method and give credence to the model.

Section 2.4 Fluid Section Model

A model of the fluid section of the synthetic jet is presented. This model captures the fluid mechanical interaction between the piston, chamber and slot. The model assumes an adiabatic process where no heat flows into the system except from the fluid entering and leaving the system. Losses are modeled by a slot velocity coefficient. Figure 2.10 shows a diagram of the fluidic section and a list of parameters used in the model.

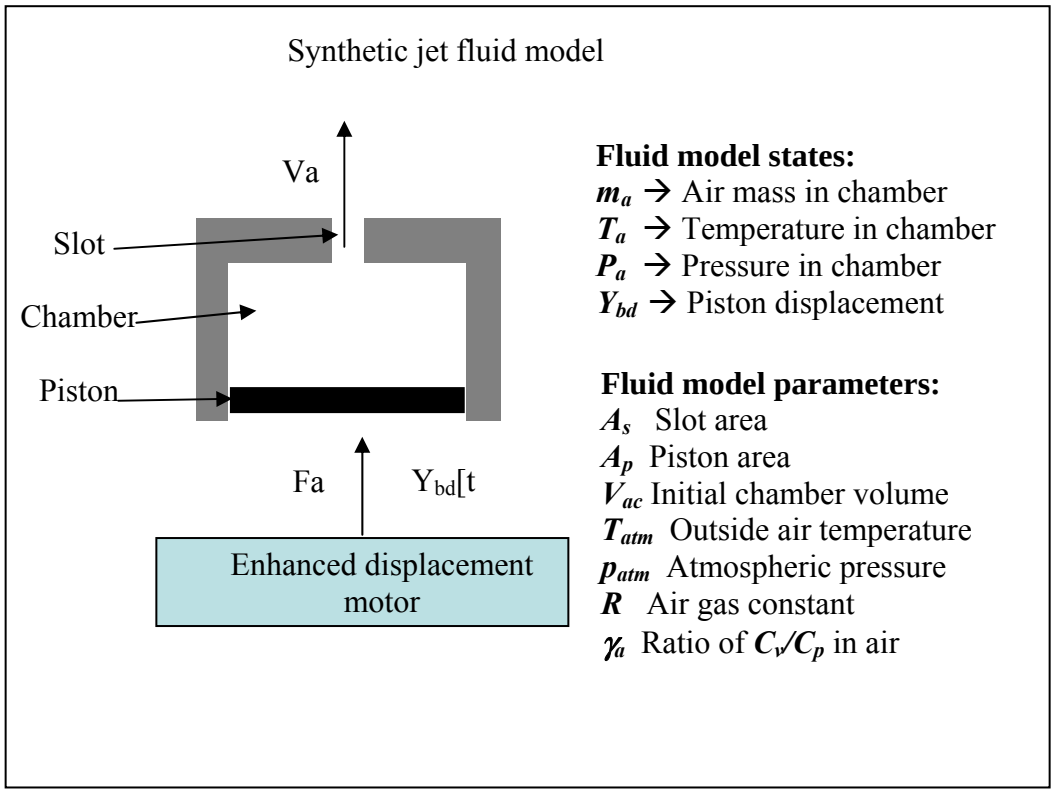

Figure 2.10 Fluid section model.

The change in mass with respect to time of the air inside the camber can be written as ***Equation 2.28***.

$$\frac{dm_a}{dt} = -\rho_a A_s K_s \sqrt{p_a - p_{atm}} \qquad \textbf{(2.28)}$$

Where ρ_a is the density of the air in the chamber, A_s is the slot area, K_s is the slot loss coefficient. This coefficient comprises models the loss in the slot and a required $(2/\rho_a)^{1/2}$ constant. Unfortunately, the pitot tube and model predictions did not contain the $(2/\rho_a)^{1/2}$ constant and suffer from this inaccuracy. p_a is the absolute pressure of the air in the chamber, m_a is the mass of air in the chamber and p_{atm} is the pressure of the air outside the chamber.

Using the ideal gas law state equation and V chamber volume leads to ***Equation 2.29***

$$P_a = \rho_c R T_c \qquad \textit{(2.29)}$$
$$m_a = V\rho_c$$
$$P_a V = m_a R T_c$$

P_a is the pressure within the chamber. ρ_a the mass density of air in the chamber, R the universal gas constant of air and T_c the absolute temperature of the air and taking the partial derivatives of the states with respect to time leads to ***Equation 2.30***.

$$V\frac{dp}{dt} + p_a\frac{dV}{dt} = RT_c\frac{dm_a}{dt} + m_a R\frac{dT_c}{dt} \qquad \textit{(2.30)}$$

The first law of thermodynamics may be written as ***Equation 2.31***.

$$m_a C_v \frac{dT_c}{dt} = \frac{dQ}{dt} - \frac{dW}{dt}$$
$$\frac{dQ}{dt} = 0. \qquad \textit{(2.31)}$$

Where C_v is the constant volume specific heat of air, W is the work being done on the air and Q is the heat in the gas. Since we are not adding any heat, $dQ/dt=0$. The work being done by the system can be written as ***Equation 2.32***.

$$\frac{dW}{dt} = -p_a \frac{dV}{dt} \qquad \textit{(2.32)}$$

Writing the above equations in matrix form yields ***Equation 2.33***.

$$\begin{bmatrix} 1 & 0 & 0 & 0 \\ RT_c & -V & m_a R & 0 \\ 0 & 0 & m_a C_v & -1 \\ 0 & 0 & 0 & 1 \end{bmatrix} \begin{bmatrix} \frac{dm_a}{dt} \\ p_a \frac{dV}{dt} \\ \frac{dT_c}{dt} \\ \frac{dW}{dt} \end{bmatrix} = \begin{bmatrix} -\rho_a A_s K_s \sqrt{p_a - p_{atm}} \\ p_a \frac{dV}{dt} \\ 0 \\ -p_a \frac{dV}{dt} \end{bmatrix} \qquad \textit{(2.33)}$$

Solving for the derivatives of the state variables yields ***Equations 2.34,*** a nonlinear differential equation of four variables.

$$\frac{dm_a}{dt} = -\rho_a A_s K_s \sqrt{p_a - p_{atm}}$$

$$\frac{dp}{dt} = \frac{\rho_a A_s \sqrt{p_a - p_{atm}} RT_c}{V} - p_a \frac{dV}{dt} - \frac{p_a R \frac{dV}{dt}}{C_v V} \qquad \textit{(2.34)}$$

$$\frac{dT_c}{dt} = -\frac{p_a \frac{dV}{dt}}{C_v m_a}$$

The following assumptions are made when implementing the model.

- Air flowing into the chamber is at room temperature and has a mass density of room temperature air.

- Air exiting the chamber is at chamber pressure and density.

- The process is adiabatic; no heat is exchanged with the walls of the chamber.

Equations 2.34 model flow from the chamber but fail to account for air density and pressure differences between inflow and outflow. Additionally, a negative square root will result when the chamber pressure becomes less than atmospheric pressure. ***Equations 2.35*** are a modified version of Equation 2.34 that take in account the differences in chamber and atmospheric air density and pressure and include equations for the air velocity through the slot. A ***Δp*** less than zero results in air flowing into the chamber; hence, a positive mass flow is expected. The air flowing

into the chamber is at the ambient atmospheric density and temperature. Air density in the chamber is set to atmospheric density and the temperature time rate of change is adjusted by the relative difference in chamber and atmosphere temperatures and the ratio of mass in the flow and the chamber mass. When the chamber pressure is greater than atmospheric pressure, mass flow is negative. The density of the air leaving the slot is the density of air in the chamber, which is calculated by dividing the volume of air in the chamber, ***V***, by the mass of the air in the chamber $\boldsymbol{m_a}$.

$$
\begin{aligned}
&\Delta p = p_a - p_{atm} \\
&\rho_a = m_a / V \\
&\frac{dm_a}{dt} = \rho_a A_s K_s \sqrt{\Delta p}, \frac{dT_c}{dt} = \frac{p_a \frac{dV}{dt}}{C_v m_a} - (T_c - T_{atm}) \frac{\frac{dm_a}{dt}}{m_a}, v_j = Ks\sqrt{\Delta p}, if\ \Delta p > 0 \\
&else \\
&\frac{dm_a}{dt} = -\rho_{atm} A_s K_s \sqrt{-\Delta p}, \frac{dT_c}{dt} = \frac{P_a \frac{dV}{dt}}{Cvm_a}, v_j = K_s \sqrt{-\Delta p}\ , if\ \Delta p \le 0 \\
&\frac{dp}{dt} = \frac{\rho_a A_s \frac{dV}{dt} RT_c}{V} - p_a \frac{dV}{dt} - \frac{p_a R \frac{dV}{dt}}{C_v V}
\end{aligned}
\qquad \textbf{(2.35)}
$$

In Equation 2.35**,** $\boldsymbol{\rho_{atm}}$ is the density of ambient air outside the chamber and $\boldsymbol{v_j}$ is the air velocity through the slot into the chamber.

Equations 2.36 introduce three state variable nonlinear ordinary differential equations needed to simulate the fluid section. These equations are solved numerically using Mathmatica and the NDSolve function. Simulation results for an example fluid section are shown in Figures 2-11a and 2-11b. The parameters were selected to

approximate the chamber of the synthetic jet that will be built and tested. The simulation was driven by a sinusoidal piston time history operating at 50 Hz with an amplitude of 0.32 cm, again chosen to reflect expected synthetic jet characteristics. Data from the three state model including chamber mass, chamber temperature and chamber pressure as well as slot velocity are shown. Slot velocity is a sinusoidal function at the excitation frequency. Chamber pressure has significant distortion from a sine function due to the nonlinear reduced flow at low pressures. Chamber mass has a small distortion due to the density of air changing with positive and negative mass flow. Chamber temperature changes 40 deg C in 5 milliseconds which seems extreme and may indicate a modeling error.

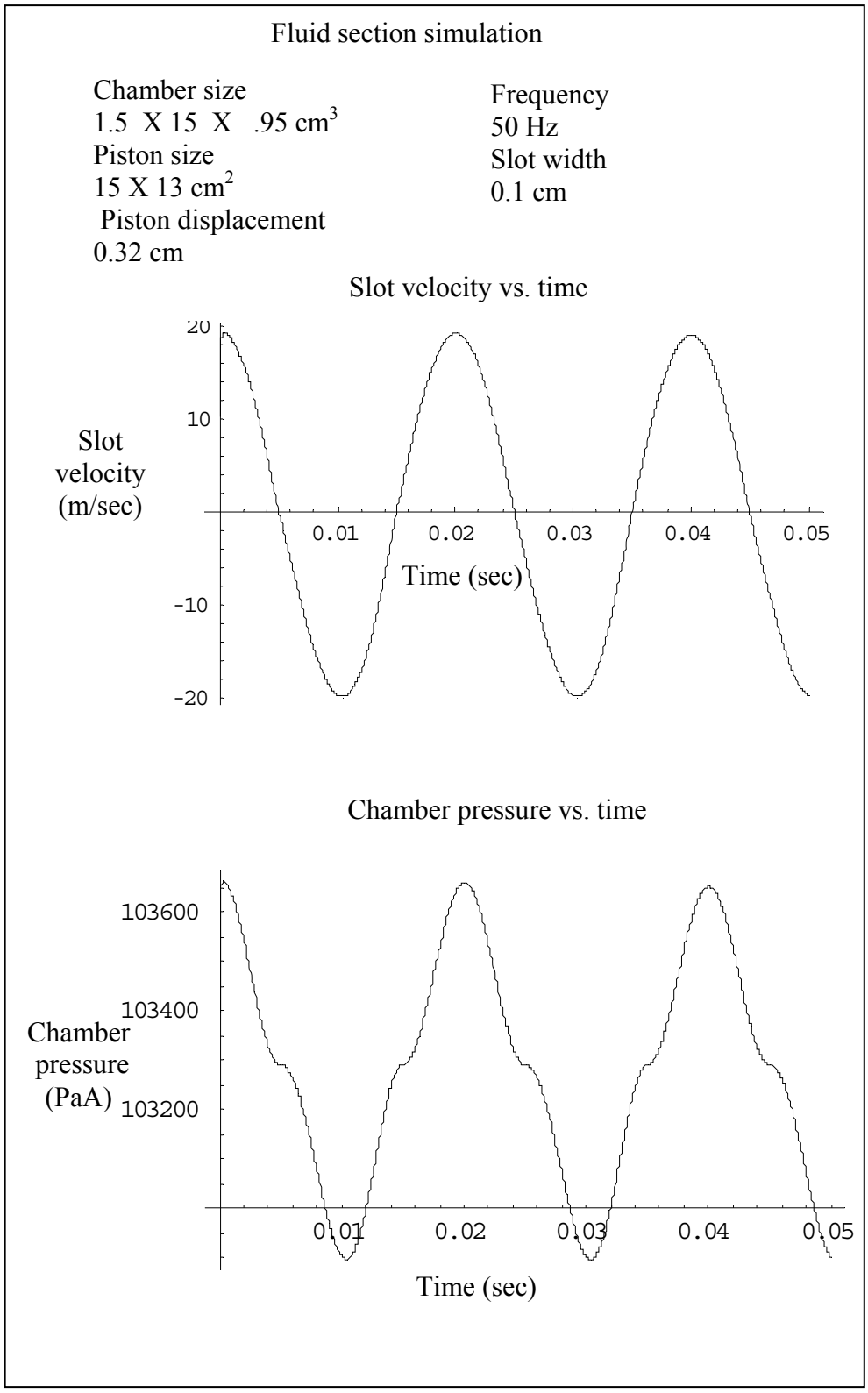

Figure 2.11A Fluid section simulation results. Top: Slot velocity vs. time. Bottom: Chamber pressure vs. time.

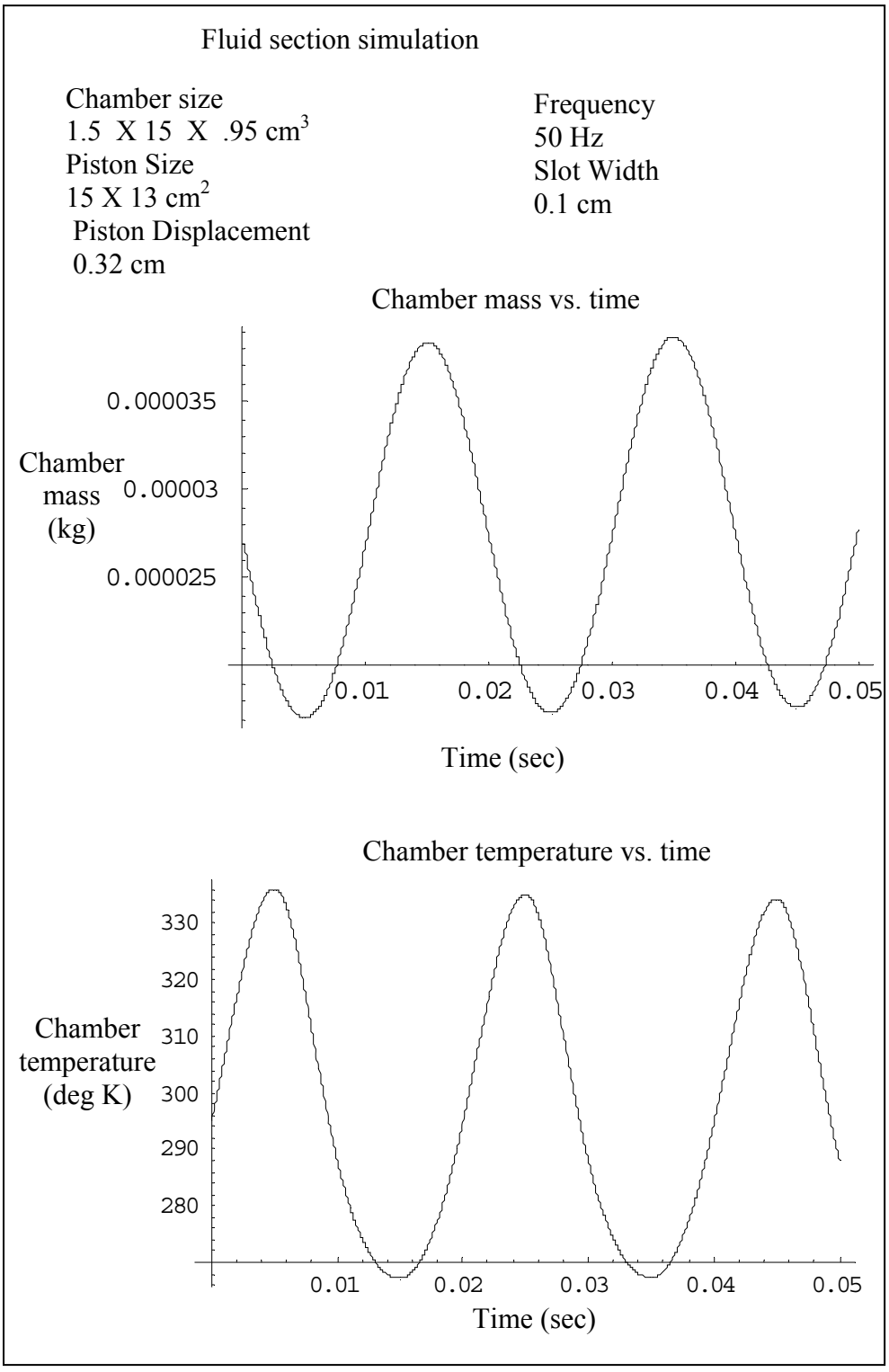

Figure 2.11B Fluid section simulation results. Upper: Air mass in chamber vs. time. Lower: Chamber air temperature vs. time.

Section 2.5 Enhanced Displacement Motor Coupled to the Fluid Model

The motor and fluid models are combined to generate a synthetic jet model.

Equations 2.35 are coupled into the enhanced displacement motor model by

Equations 2.36.

$$
\begin{aligned}
V &= V_{a0} - A_p Y_{bd} \\
\frac{dV}{dt} &= -A_p \frac{dY_{bd}}{dt} \\
Fa &= -(p_a - p_{atm}) * A_p
\end{aligned}
\qquad \textbf{(2.36)}
$$

In these equations, Y_{bd} is the previously defined motor displacement, ***Fa*** is the force on the motor, V is the volume of the chamber, V_{a0} is the volume of the chamber at zero motor position and A_p is the area of the piston. The mass of the piston is included in the motor dynamics.

Simulation results from a synthetic jet are shown in Figures 2.12a-c.

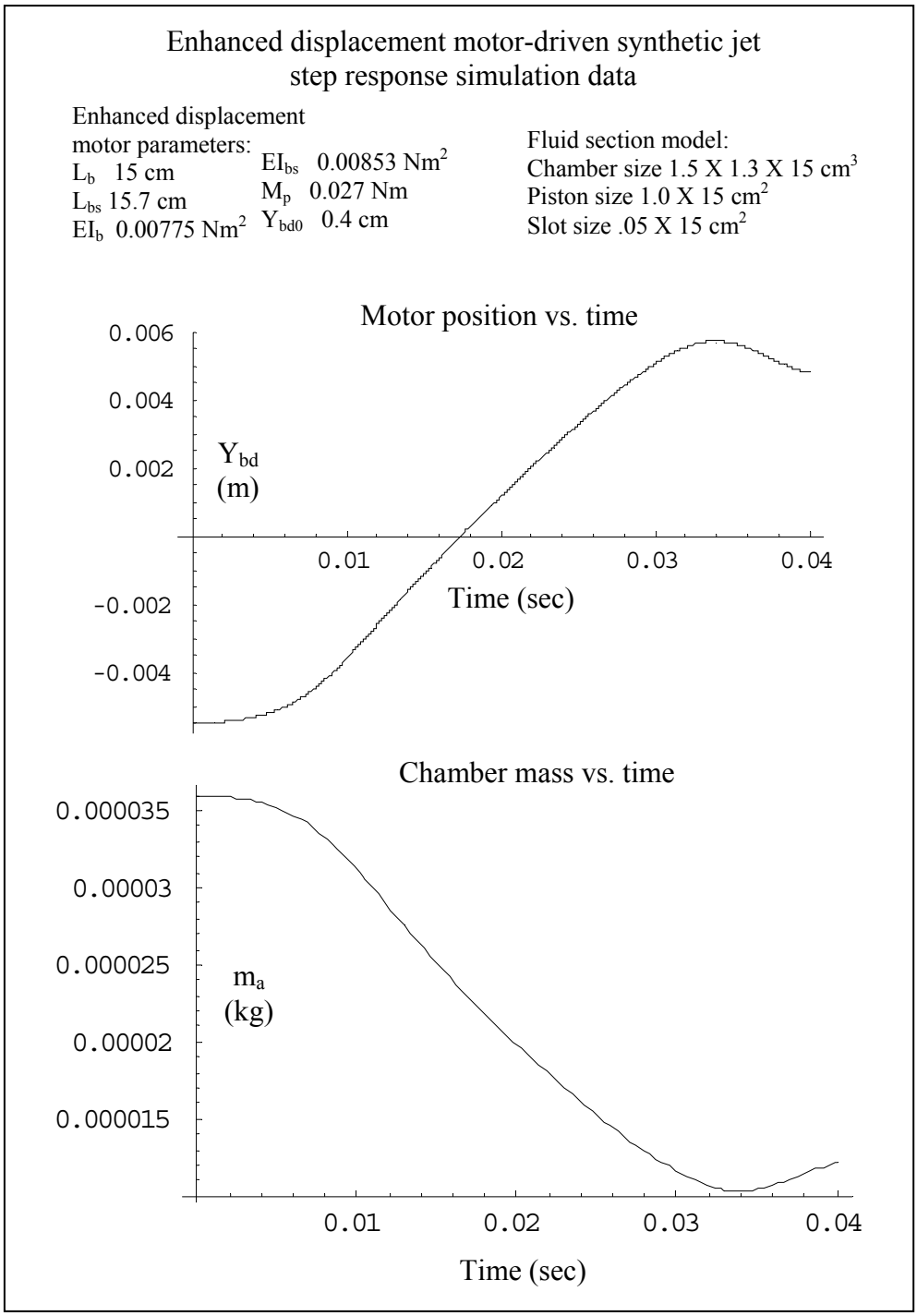

Figure 2.12A. Top: Simulated synthetic jet motor position vs. time.
Bottom: Chamber air mass vs. time for a step moment input.

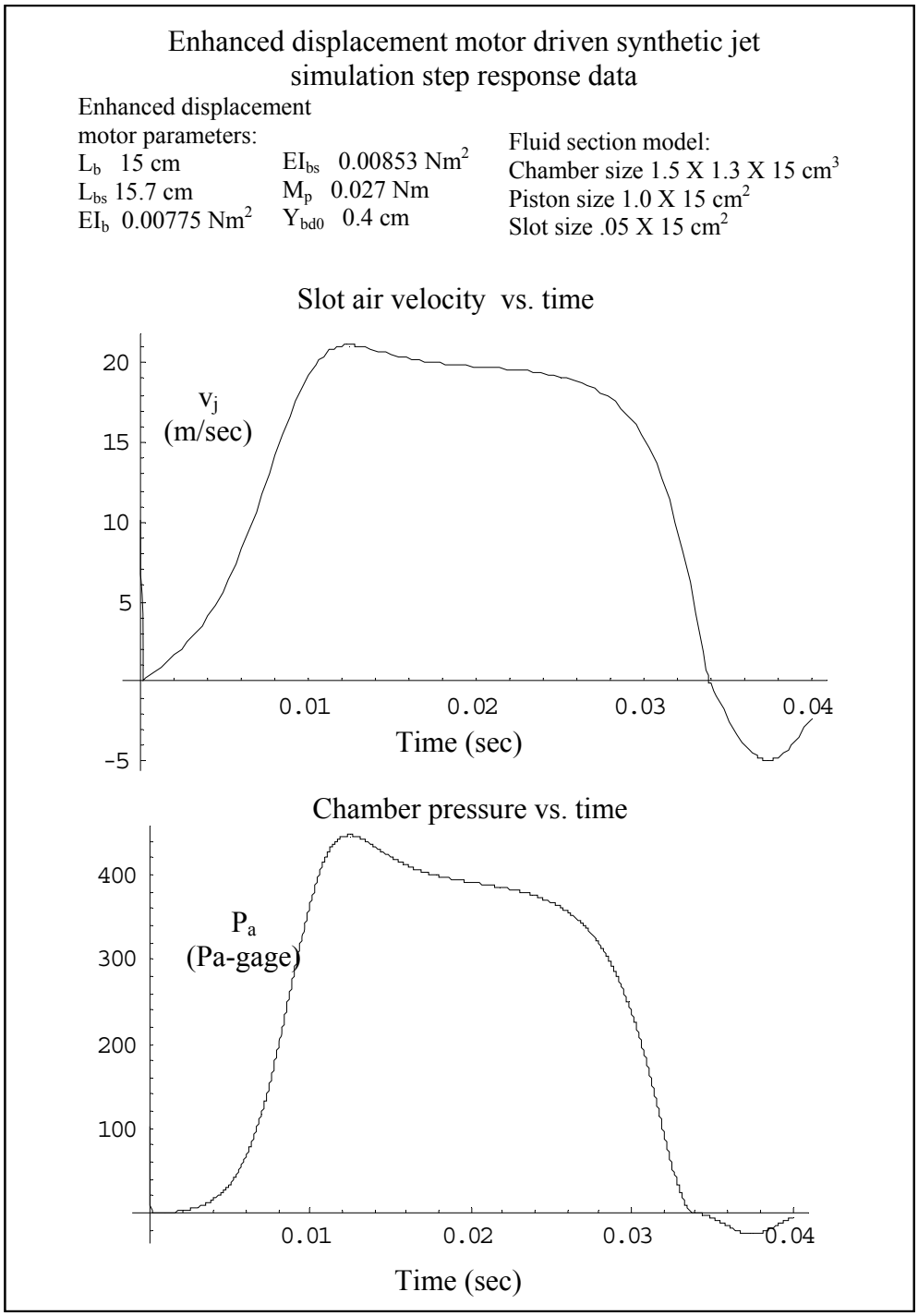

Figure 2.12B. Simulated synthetic jet velocity and pressure for a step moment input. Upper: Slot air velocity vs. time. Lower: Chamber pressure vs. time.

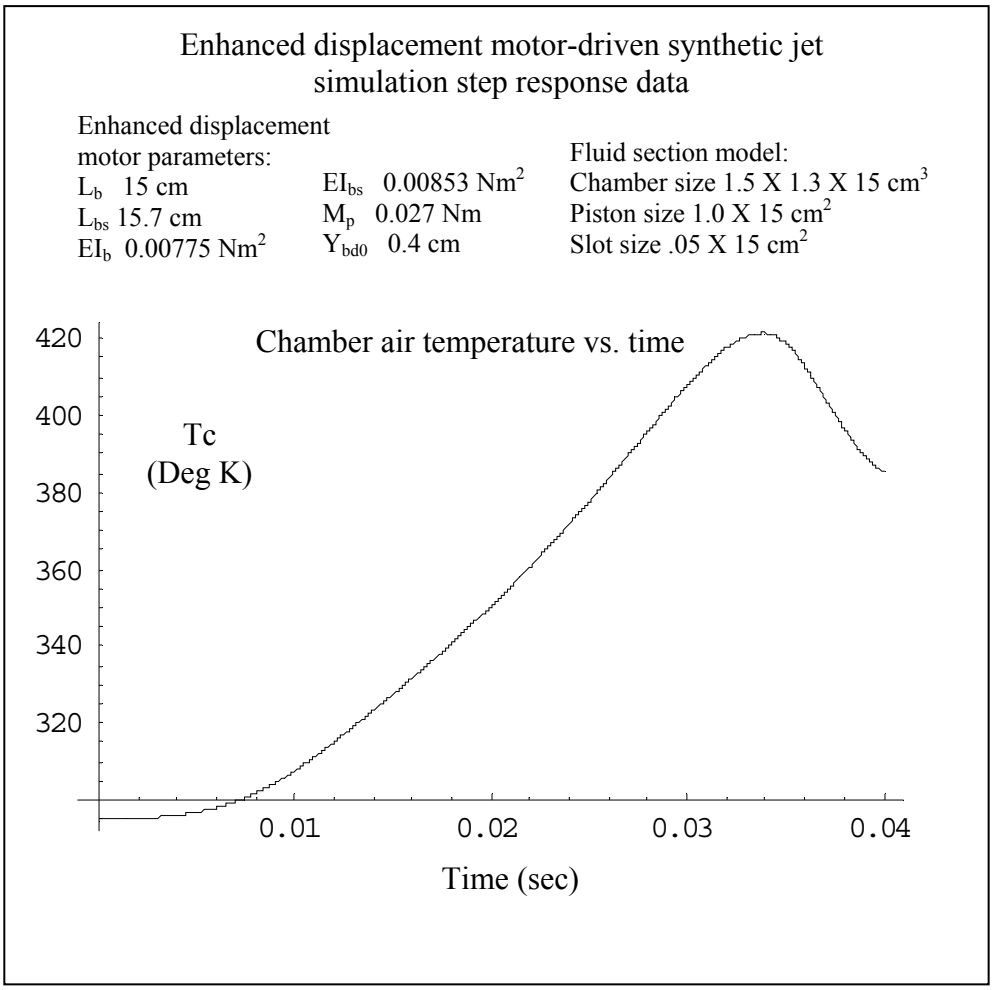

Figure 2.12c Simulated synthetic jet chamber temperature vs. time.

The data shown in Figures 2.12a, b and c was generated assuming an initial condition of -0.6 cm for the ED motor displacement and a constant 0.027 Nm of torque applied to the bimorph. Bimorph and bias beam are made from two PFCs (15.3 cm x 0.038 cm) sandwiched between a carbon composite center (15.3 cm x 0.013 cm). The applied torque (M_p) and bending stiffness (E_bI_b, E_bI_{bs}), were calculated using carbon composite properties summarized in Appendix II. PFC strain properties were obtained from the manufacturer via phone conversation (10 GPa extension modulus, 500 μstrain free strain). These properties were evaluated using the Euler-Bernoulli

model described in Equations 2.1 and 2.2 to provide moment (M_p) and bending modulus (E_bI_b, and E_bI_{bs}). The masses of the bimorph and bias beam are 8 grams and the tilt connector moment of inertia is 2 x 10^{-7} kgm^2. The piston mass is set to 2 grams. The zero moment displacement of the bimorph is set to 0.4 cm. The size of the bimorph is 15 x 1.2 cm^2 and the bias beam size is set to 15.7 x 1.3 cm^2. Fluid section properties are as follows; piston size 15 x 1.3 cm^2, slot size 15 x 0.05 cm^2 and chamber size 15 x 1.3 x 1.5 cm^3. Standard atmosphere, temperature and pressure are used.

The simulation shows that the piston has traveled the full stroke between -0.6 and 0.6 cm in 0.031 seconds. Peak air velocity develops at 0.012 seconds and then shows a nearly constant velocity and pressure region as the chamber is emptied. The nearly constant velocity and chamber pressure implies that the motor is working against a constant pressure, causing stroke velocity to be limited by the pressure in the chamber. At 0.03 seconds, the piston has nearly reached the end of its stroke; motion of the piston is now limited by the stiffness of the motor which prevents further motion of the piston. Air velocity and chamber pressure fall rapidly. Chamber temperature rises rapidly due to the piston providing a constant compression of the chamber air. The high temperature rise (100 K in 30 msec) for a modest pressure may indicate poor simulation accuracy. Once the end of the stroke is reached, temperature begins to fall.

The example shown above is a single design point. The enhanced displacement synthetic jet actuator offers a rich design space for optimized performance of the motor. The pulse-like behavior can be modified to produce a higher slot velocity. For instance, a high amplitude, short duration spike would result by decreasing the piston area and slot area so that the piston velocity is limited primarily by inertia, resulting in a high time rate of change in the chamber volume. A higher velocity can also be achieved by increasing bimorph-blocked force so that the chamber pressure is higher. A higher blocked force can be achieved by adding a second layer of PFC to the top and bottom of the bimorph. The additional layers increase the bimorph blocked force in two ways. First the added active material doubles the blocked force the PFCs apply to the beam. Second the PFC applied force is further from the neutral axis which results in an increased in bending moment. Increasing the thickness of the uni-axial carbon composite layer without adding additional PFC layers, will also increase blocked force due to the PFC generated force being applied further from the neutral axis. Unlike the reference motor, where increasing the thickness of the bimorph increases the stiffness and decreases the free displacement, the ED motor displacement is only limited by the maximum allowable strain of the bimorph materials.

The maximum frequency of the synthetic jet is limited by the inertia of the ED motor components and the blocked bimorph force. The major contributors are beam inertias. A shorter beam with the same cross section will increase the operational frequency at the cost of a decrease in piston displacement.

In summary, the enhanced displacement motor-based synthetic jet has been modeled using Lagrange's equations. The model predicts that with the parameters studied, the ED motor will provide 14 times the energy per cycle to an optimal spring load relative to energy per cycle produced by the reference motor. The frequency response of the ED motor is about 1/3 that of a reference motor but still provides a significant increase in power output. The fluid section of the actuator is modeled using three states and is integrated into the motor simulation. An example synthetic jet actuator design is modeled and is shown to produce air injection between 1 and 30 Hz.

Chapter 3: Synthetic Jet Design and Testing

The design and testing of the synthetic jet actuator will be presented in three sections. Section 1 will describe the design and testing of the ED motor and compare the results with the simulation. The model captures both the dynamics and low quasi-static properties of the ED motor. Section 2 will document the design, integration and testing of the synthetic jet actuator. Synthetic jet actuator data are compared with the simulation. The model captures the basic properties of the synthetic jet but over-predicts synthetic jet performance. Section 3 will summarize these results and discuss their implications for future motor and synthetic jet actuator design.

Section 3.1 Enhanced Displacement Motor Design and Testing

Subsection 3.1.1 PFC Characterization

Figure 3.1 shows a solid model of the ED motor. The ends of the PFC bimorph and the bias spring beams are attached to the left and right edges of two tilt connectors. The tilt connector-beam connections are designed to simulate pinned-pinned boundary conditions, i.e. to restrict lateral displacement while introducing minimal restriction to rotation at the beam ends. The middle of the tilt connectors are connected to a base support structure by a flexure wire interfaced with a threaded adjustment bolt that allows for fine adjustment of the compressive axial loads imposed on the beams by the tilt platforms. Several design concepts were assessed before identifying this combination as capable of providing suitable compression adjustment performance as the flexure wires are put in tension. A carbon composite piston attached to the bimorph provides an interface to the fluid section.

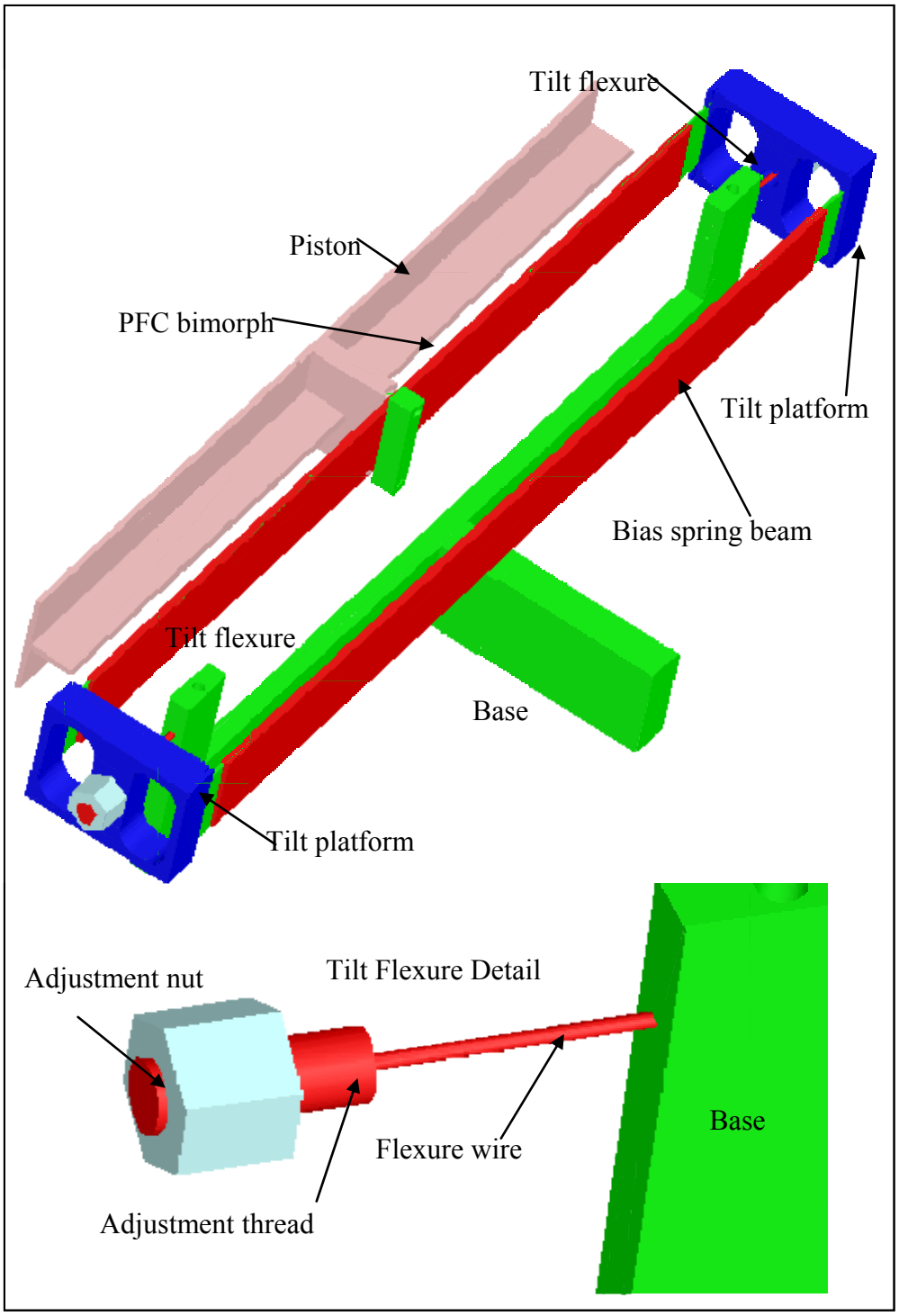

Figure 3.1 Top: Enhanced displacement motor design.
Bottom: Flexure detail..

The ED motor is designed around available PFC devices from Advanced Cerametrics Inc. Each PFC device is 15.3 X 1.3 X 0.038 cm^3 in size, so the bimorph and bias

spring beams are sized accordingly. Three layers of 0.017 cm thick uni-axial carbon fiber prepreg make up the center of each beam. The prepreg composite formulation allows for a straightforward fabrication using a hot press approach. The center ply of the bimorph performs three functions. First, the carbon provides a bond that holds the bimorph together. Second, carbon the composite moves the line of action of the PFC elements away from the neutral axis of the bimorph, which increases their moment arm and accordingly the moment generation ability of the bimorph. Third, the center ply is made from three layers of carbon composite where the center layer extends beyond the ends of the other two layers of the bimorph, providing flexure/hinges which are used to attach the bimorph to the tilt connector. One end of the PFC has two silver epoxy tabs for electrical connection. The tabs are 1.2 cm long and piezoceramic fiber is not under this section of the PFC, hence this section of the bimorph does not have a PFC-induced moment.

Measurement devices used to measure synthetic jet parameters were calibrated in the lab. The load cell was calibrated using known mass weights varying from 10 to 500 grams with a resolution of 0.1 gram. The pressure sensors were calibrated using a water manometer with pressures from 0.5 to 5 inches of water with a resolution of 0.1 inch. Both laser displacement sensors were calibrated using an optical stage with a resolution of 0.001 inch.

Figure 3.2 shows a PFC modified to allow characterization of PFC free strain and extension modulus. Characterization was performed by vertically suspending the

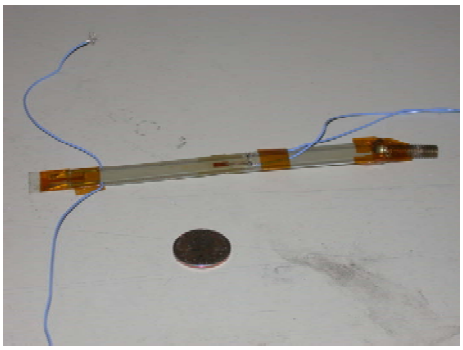

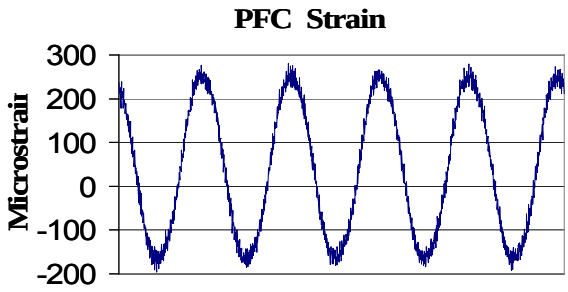

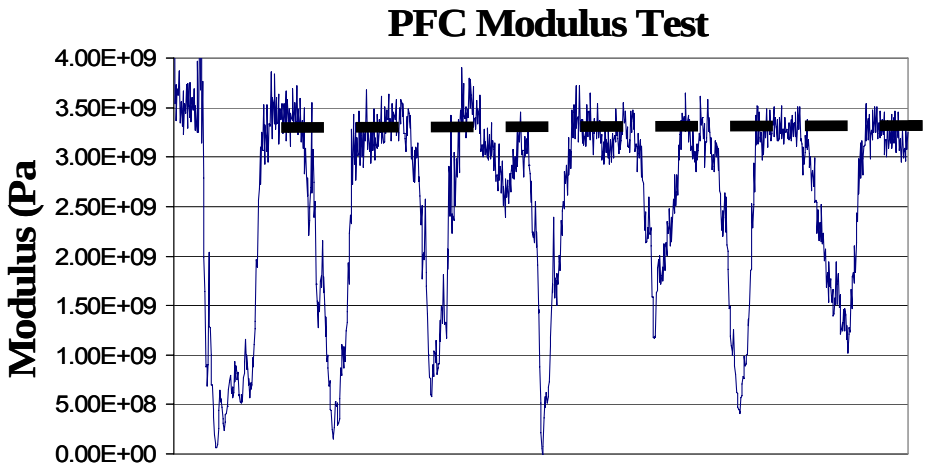

AFC Properties	Value
Size (cm^3)	13.9 X 12.4 X 0.0038
Free Strain (μstrain) at 500 V zero to peak	220
Modulus (MPa)	3.3

Figure 3.2 Piezo fiber composite actuation properties. Top Left: PFC Top Right: PFC Free Strain at 500 V 0-p. Middle: PFC Modulus test data. Bottom: Properties summery .

PFC from one end, attaching a 200 gram mass to the free end and recording strain responses to PFC actuation. Electrical leads were attached to the PFC using conductive epoxy. Free strain was measured using a strain gage, aligned along the length and attached in the center of the PFC. Additionally, a laser displacement

sensor measured the axial displacement of the PFC. The laser displacement sensor was used to measure the displacement of the 200 gram mass, which provides a second independent measurement of PFC strain. The strain gage measurement underreported PFC strain. A likely cause of the low strain measurement from the strain gage was a problem with the gage-structure bond and specifically the layer of epoxy applied to fill in the PFC ridges between electrodes to provide a smooth mounting surface for the strain gage. Figure 3.2 shows the free strain measurement with 500 V zero to peak sinusoidal voltages applied to the PFC. A zero to peak free strain of 220 μstrain was measured using the laser displacement sensor. The laser-derived strain measurement was used to calibrate the strain gage.

The PFC extension modulus was measured by attaching one end of the PFC to a load cell and cyclically applying an axial, primarily tension force (with a finger) to the PFC free end. Excursions into compression which caused buckling resulted in the non-constant modulus. Output from the PFC stain gage and the load cell were recorded. Figure 3.2 shows PFC modulus data. The measurement is valid only for constant data measuring about the 3 MPa region (indicated with a dashed line) because regions of rapid swings to much lower modulus values correspond to buckling of the PFC.

Subsection 3.1.2 Bimorph Beam Fabrication and Characterization

The PFC/ carbon composite bimorph beams are manufactured using a hot press process. Figure 3.3 illustrates this process. The press consists of two aluminum plates, 15.3 X 10 X 12.5 cm^3 in size. Six ¼-20 bolts hold the two plates together with

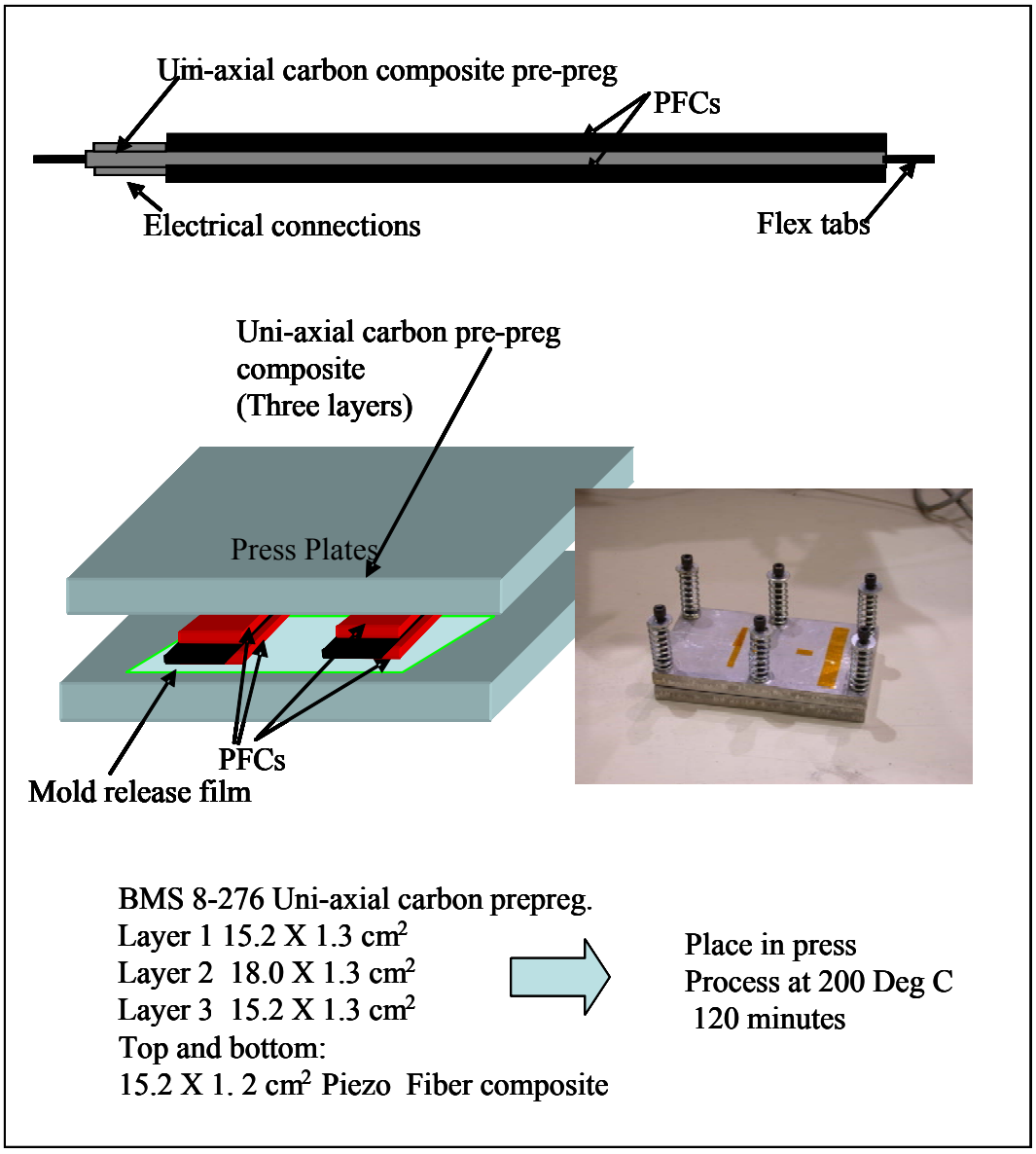

Figure 3.3 Bimorph beam assembly process. Top: Bimorph cross section, Middle Left: Fabrication lay-up. Middle Right: Assembly press Lower: Layer specifications.

compression springs providing a constant load force. Each plate has a layer of fluoro-polymer film attached with Kapton tape, which provides a non-stick surface. Three uni-axial carbon composite pre-preg plies (BMS 8-276) are cut to the size with the fiber direction along the PFC length. The outer plies are cut to match the PFC outline including the electrode area. The center ply is 2.5 cm longer than the outer carbon

plies to provide a flexure to attach the bimorph to the tilt platform. The bimorph is assembled with the three carbon composite layers in the center and a PFC on each outer surface. Two bimorphs are fabricated at the same time to keep the two press plates parallel. The press plates are forced together with the six spring/bolts threaded into the base ½ inch and placed in an oven at 200° C for 120 minutes. The press is removed from the oven and allowed to convection cool. Once cooled to room temperature, the bimorphs are removed from the press and trimmed to size. The hot press process displaces some of the fiber composite from between the PFCs. Original ply thickness is 0.02 cm, but post-cure plies have shrunk to a 0.0127 cm thickness. The PFCs are poled at the factory at 1200 VDC. The bimorphs will be operated at 500 V zero to peak. The PFCs are driven differentially, so when one is energized in the poling direction and the other is energized against the poling direction a bending moment is produced on the bimorph. Two electrical leads and jumper wires are attached to the bimorph using electrically conductive epoxy.

Measured bimorph properties include beam-bending stiffness, PFC applied moment, and buckling force displacement characteristics. Two test fixtures were built to measure these properties, a beam bending test fixture and a beam buckling fixture as shown in Figure 3.4. The bending test fixture consists of an aluminum plate, 17 X 10 X 1.2 cm^3. Two parallel 0.317 cm diameter rods separated by 15.3 cm are attached to the 17 X 10 cm^2 face of the plate. The rods lie along the 10 cm axis of the plate. The two rods provide a rolling contact at each end of the bimorph and approximate a pinned-pinned boundary condition. A 1.2 cm hole in the center of the 17 X 10 cm^2

plate face provides access to a laser displacement sensor. The plate is suspended between two blocks and the laser position sensor is placed below the plate. A load cell is attached to a vertical adjustable table so that it can contact the bimorph center and apply a measurable load to the center of the beam.

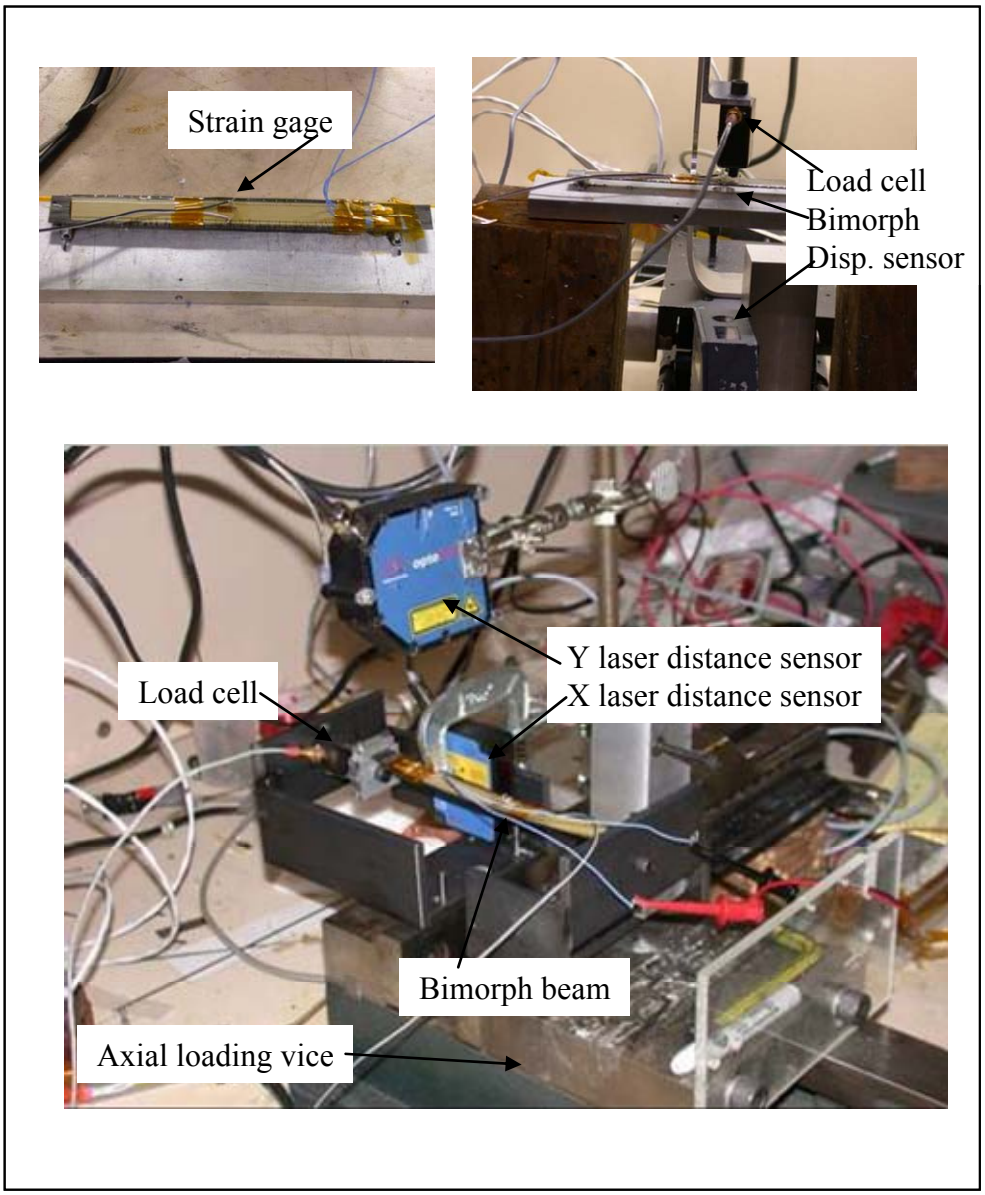

Figure 3.4 Buckled beam characterization test fixtures. Upper Left: Bimorph beam with strain gage. Upper Right: Bending test fixture. Lower: Buckling test fixture.

Three bimorph stiffness data sets were obtained for both open and short circuit conditions. Stiffness data was obtained by compressing the center of the beam with the load cell while bimorph center position and compression load data were recorded. A linear least square estimation of the slope of the force-displacement curve, K_b, for each data set was calculated using an Excel spreadsheet. Bimorph stiffness data, K_b, was used to calculate the composite modulus of elasticity times the beam cross section area moment of inertia [36], E_bI_b, using ***Eq 3.1.***

$$E_b I_b = \frac{K_b * L^3}{48} \qquad \textit{(3.1)}$$

The average of the three runs was calculated resulting in an estimate of the bimorph bending stiffness E_bI_b.

The bimorph free displacement data was obtained by applying a 500 Vpeak sinusoidal voltage to the bimorph and recording center displacement with the load cell removed. The beam measured modulus E_bI_b was used in Eq 3.2 to calculate the PFC measured applied moment M_p.

$$M_p = \frac{Y_{bd} * 8E_b I_b}{L^2} \qquad \textit{(3.2)}$$

A PFC moment coefficient was calculated by dividing M_p by 500 Volts. Figure 3.4 shows the bimorph test fixture and Table 3.1 summarizes bimorph data. A strain gage was mounted on the center of the bimorph to sense axial strain. Strain gage data agreed with displacement-based strain produced by solving Equation 3.2 for M_p/E_bI_b. Bimorph beam maximum strain which occurs on the surface of the beam is calculated by multiplying, M_p/E_bI_b curvature of the bimorph, to half the bimorph thickness [36].

Table 3.1 Measured bimorph properties.

Closed				Open		
Slope (N/mm)	E_bI_b (Pa-meters^4)	Average	Piezo Moment Coefficient (N-meters/V)	Slope	E_bI_b	Average
0.878	0.06480428			0.948	0.0699	
0.907	0.0668985			0.981	0.0723	
0.905	0.06675844	0.0661	3.25E-05	0.945	0.0697	0.07069
Blocked force (N)		0.57				
PFC moment (Nm)		0.0163				

The buckling properties test fixture, also shown in Figure 3.4, consists of a machinist's vice that was modified to provide rigid mounts for a load cell and beam-ends. A load cell is attached to the fixed end of the vice and a beam mount, which clamps the bimorph beam flexures, is affixed to the other side of the load cell. A second beam mount is attached to the moving vice plate. A laser distance sensor is mounted over the vice to measure beam out-of-plane displacement, $\boldsymbol{Y_{bd}}$ and a second laser sensor is placed to measure beam axial displacement, $\boldsymbol{X_b}$ while the bimorph is being axially compressed. A strain gage is placed on the center of the bimorph to measure bimorph maximum strain.

Open and short circuit buckling data was obtained for the bimorph beam. Short circuit buckling data is shown in Figure 3.5. Short circuit data is of primary interest because the motor is run by a constant voltage amplifier, which provides a short circuit condition. A critical buckling load of 22 N is observed which is consistent with a bucking load calculated using measured bending stiffness, $\boldsymbol{E_bI_b}$.

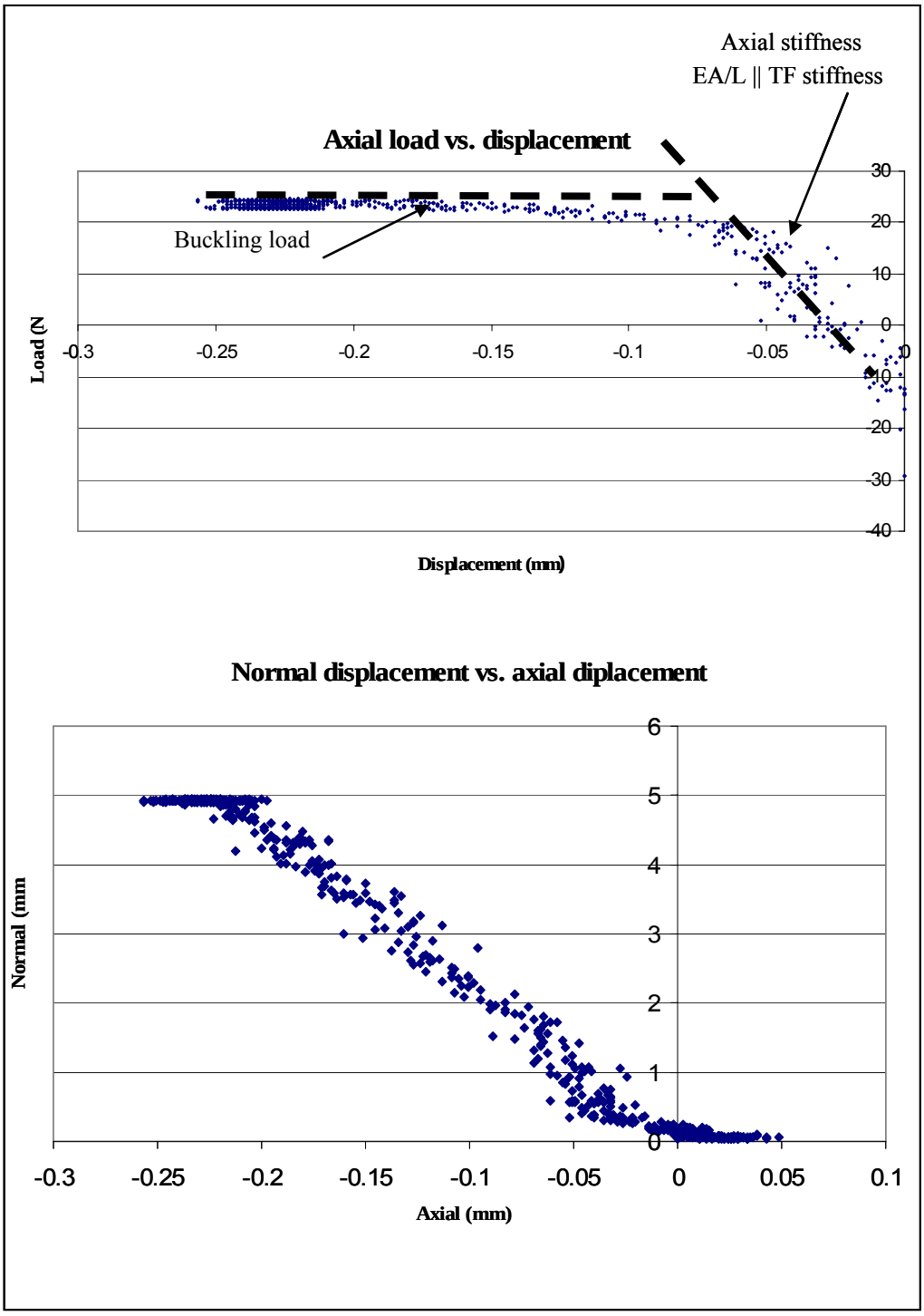

Figure 3.5 Bimorph beam buckling characterization. Upper: Bimorph axial load vs. displacement. Lower: Bimorph center displacement vs. axial displacement.

The bias spring buckled beam must have similar buckling properties as the bimorph

beam. A second un-powered bimorph is chosen for the bias spring. Table 3.2 shows bias beam stiffness and buckling properties.

Table 3.2 Measured bias beam properties.

Bias beam open circuit properties			
Slope (N/mm)	E_bI_b (Pa-m^4)	Average	Buckling load (N)
1.133	0.083549446		
1.0924	0.080555529		
1.1276	0.08315124	0.08242	25

Subsection 3.1.3 Enhanced Displacement Motor Assembly Design and Characterization

The assembled ED motor's force-displacement and displacement-time performance were characterized using the apparatus described in Figure 3.6.

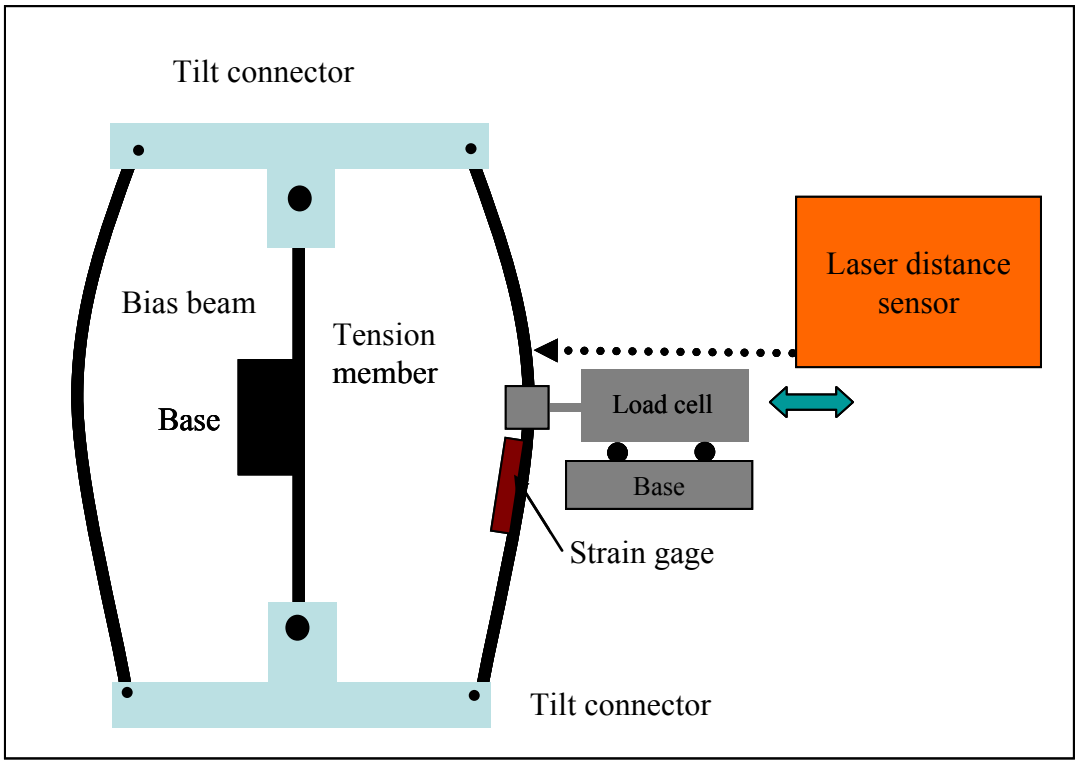

Figure 3.6 Enhanced displacement motor, force-displacement and displacement-time characterization test configuration.

The motor was clamped to a table and a laser displacement sensor rigidly mounted so that the center displacement of the bimorph could be measured. A load cell attached to the center of the bimorph was mounted using an adjustable mounting bracket for repositioning. This allowed horizontal translation of the load cell to facilitate measuring force-strain data under different initial strains, or equivalently, different initial bimorph biasing voltages. Additionally, as shown, a strain gage was installed on the inner surface at the center of the bimorph.

Force as a function of free displacement data was collected by applying a voltage to the ED motor and moving the load cell across the operational region while recording position and load data. Data was obtained with voltages of +500 volts, -500 volts,

+250 volts, -250 volts, and 0 volts. Motor force-displacement data for +500, 0 and -500 volt cases are shown in Figure 3.7.

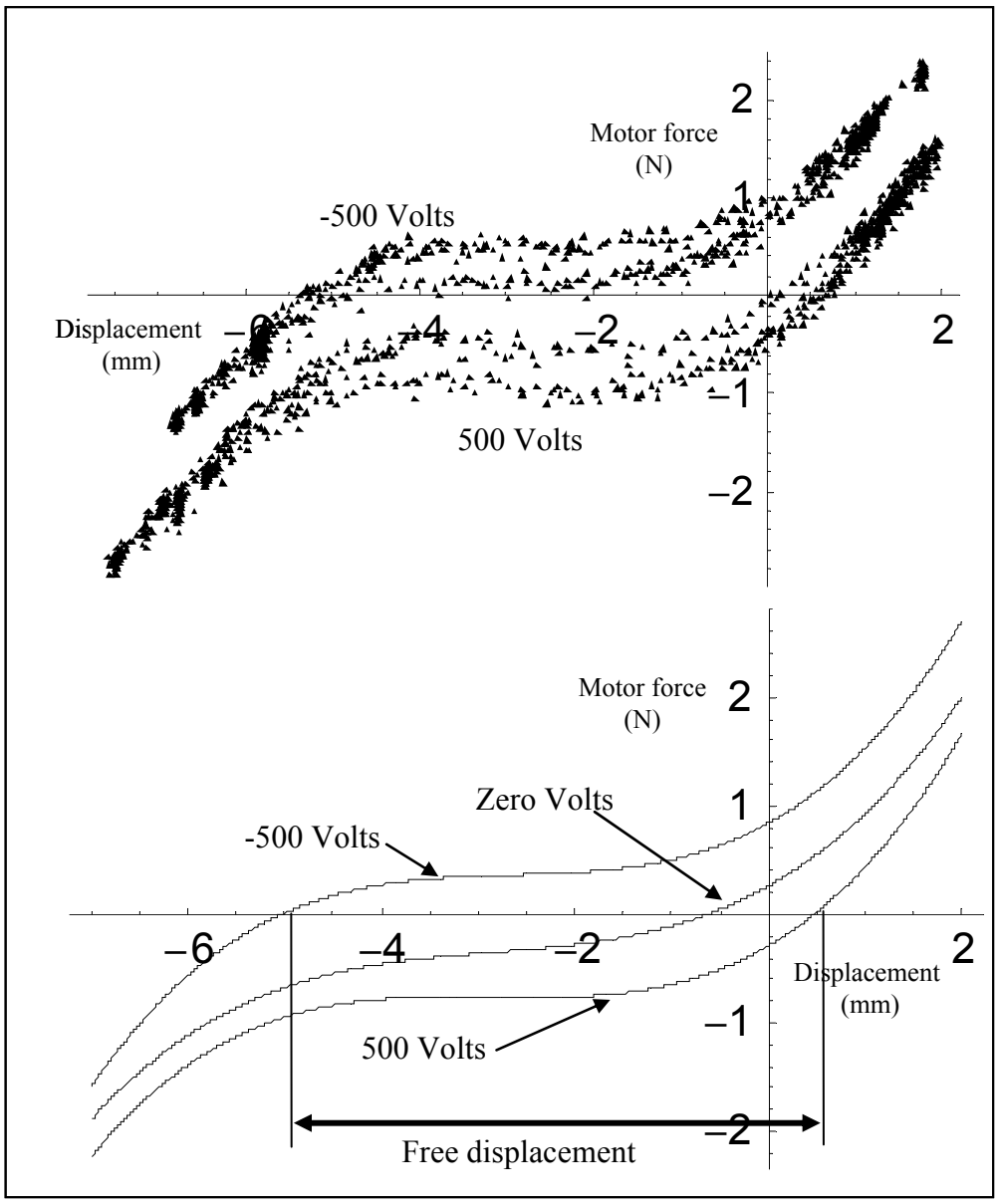

Figure 3.7 ED motor load line measurements. Upper: Motor force vs. Displacement raw data. Lower: Motor force vs. displacement least square fit.

The least square curve fits of the data show that the motor free displacement will range from -5.5 to 0.5 mm or a free displacement of 6 mm. This value is obtained from the distance between the +500 volt case zero crossing and the -500 volt case

zero crossing. The raw force-displacement data shows a hysteresis of 0.25 N for both positive and negative voltage cases. The motor force is not symmetric with the 500 volt case exhibiting 0.2 N larger force than the -500 volt case.

The load cell was removed and the dynamic characteristics of the motor were obtained. Data was obtained for step and sine inputs at ±500 and ±250 volts. The frequency response capability of the motor was also examined with data obtained at 10, 40 and 50 Hz. Figure 3.8 shows the time history data for this test. The data shows the 0- 40 Hz bandwidth capability of the motor. The 10 Hz data shows that the output of the motor is a lightly damped square wave with an amplitude of 5.5 mm. The same frequency sine data shows a distorted sinusoidal output amplitude of 4.5 mm. The 40 Hz square wave excitation data shows that the bandwidth response is rolling off as the output is nearly sinusoidal (i.e. the ability of the motor to displace at 120 Hz and the higher odd harmonics needed to accurately produce a square wave has disappeared). The 50 Hz data shows a reduced amplitude sinusoidal output for a square wave input. Data from the 10 Hz square wave excitation at ±250 volts shows a severely distorted, lightly damped square wave output most likely comprised of the 10 and 30 Hz components and greatly reduced higher odd harmonics. A recommendation for future characterization is that a spectral analysis of the output wave form and a frequency response function be performed using broad input to quantify the broadband capability of this motor. Also shown is the strain of the bimorph as the motor is driven by a ±500 volt square wave at 10 Hz. Peak to peak

strain experienced by the bimorph is 1700 μstrain. (The strain data has an anomaly for every half-cycle that has not been explained).

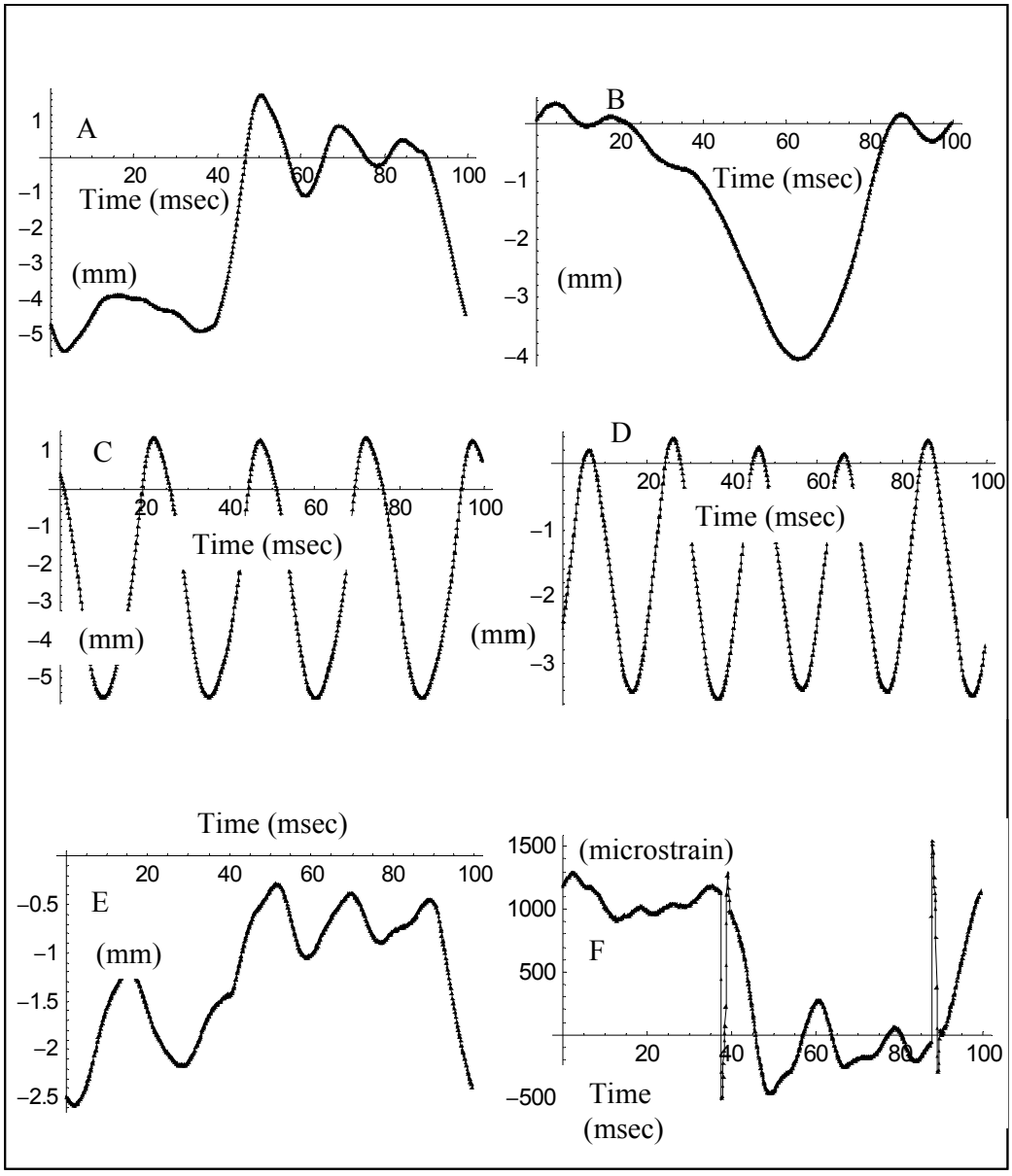

Figure 3.8 ED motor step and sine response vs. time with zero piston mass.
A: 10 Hz Step ±500 Volt drive. B: 10 Hz Sine ±500 Volt drive. C: 40 Hz Step ±500 Volt drive. D: 50 Hz Step ±500 Volt drive E: 10 Hz Step ±250 Volt drive. F: 10 Hz Step Bimorph strain vs. time ±500 Volt drive.

Subsection 3.1.4 Enhanced Displacement Motor Simulation and Data Comparison

Measured ED motor properties, shown in Table 3.3, were used in the ED motor model to verify model fidelity. Comparison between force-displacement

Table 3.3 ED motor and model properties

Parameter	ED model	ED motor
L (bimorph), (meters)	0.153	Measured 0.153
EI (bimorph)(Nm^2)	0.0661	Measured 0.0661
ρ (bimorph), (Kg/m)	0.052288	Measured 0.053
PFC Moment (bimorph), (500 Volt) (Nm)	0.0163	Measured 0.0163
L (bias beam) (meters)	0.1535	Measured 0.1535
EI (bias beam))(Nm^2)	0.068	Est. 0.068
P (bias beam), (Kg/m)	0.052117	Measured 0.052
Bimorph zero moment displacement, (meters)	0.002	Est. 0.002
Tilt Platform x moment of inertia, (Kgm^2)	6.84×10^{-7}	Measured 6.84×10^{-7}
Piston mass, (Kg)	0	0
Damping coefficient	1	Unknown
Tilt platform radius, (meters)	0.00953	Design 0.00953

characteristics from measured motor data and from model predictions are shown in Figure 3.9 upper and lower graphics respectively. As previously discussed, the quasi-static model does not capture the straightening of the bias beam. Near equal length

beams limit the displacement of the motor. As the bimorph beam extends, the bias beam straightens.

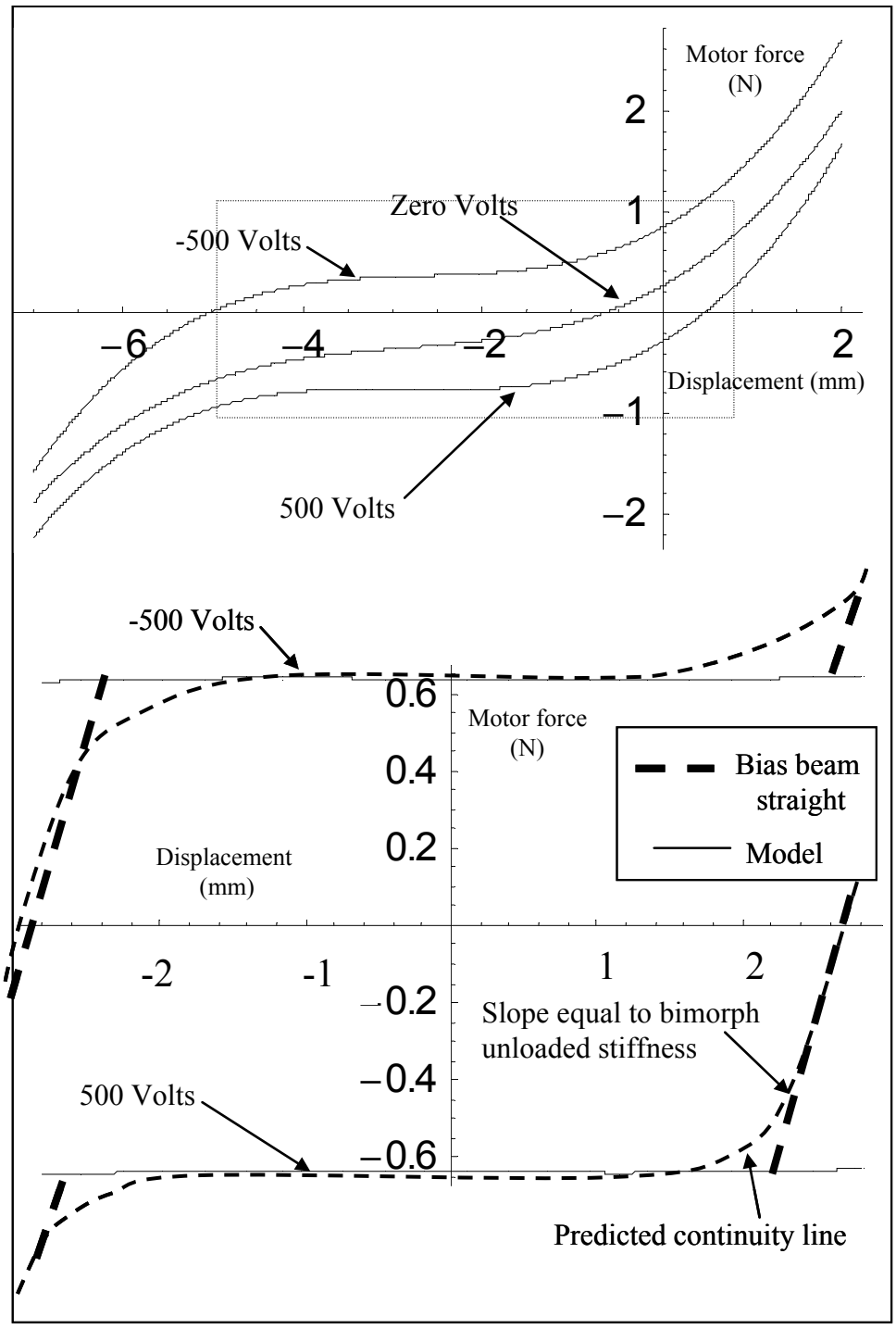

At the point where the bias beam is straight, any further motor displacement will unload the bias beam, removing the buckling load thereby significantly stiffening the bimorph actuator and limiting the bimorph beam excursion.

Two lines which represent the behavior of the motor when operating in the extended motor position region are shown for each of the two applied voltage cases. These lines have the same bending stiffness or slopes equal to the unbuckled bimorph beam stiffness. A fairing curve is added that may approximate the straightening characteristics of the real motor. Note that the bimorph beam buckling data shows a smooth transition between the un-buckled and buckled state, which would show up as a smooth transition in the ED motor data. This data shows good agreement between total displacement and blocked force.

The measured motor position data is arbitrarily referenced to a 2 mm in position from the mid point of the motor displacement or the mid point between the zero force positive voltage point and zero force negative voltage point. (The boxed-in region from +1mm to -5mm.)

A common initial offset for both the ED motor and ED motor model were set to 2 mm. The ED motor offset was set to 2mm by adjusting the tension nut and the model zero-applied moment offset (Y_{bd0}) was set to 2 mm. Although the bimorph beam bending stiffness is soft to the touch, it exhibits a single stable position without applied electrical input. This is indicative of an un-modeled applied moment. The

unequal base lengths, L_b' and L_{bs}' ,of the bimorph and bias beam case an angle to be introduced into the flexure tabs which produce an un-modeled bending moment on the bimorph beam. The tab angle has been confirmed by observing the motor. Measured blocked force data is consistent between the model predictions and the data gathered from the ED motor. The relationship between PFC-induced moment and blocked force was a concern but the agreement between the model and the blocked force data supports the modeling approach. The constant displacement portion of the motor data confirms the Lagrange energy approach used for analysis.

Figure 3.10 compares the model and ED motor dynamic responses with each driven with a -500 to 500 volt step input. Unlike the static force-displacement model, the dynamic model captures the effect of the bias beam straightening. It is thought that as the bias beam approaches a straight condition, a high reverse acceleration is generated from the nonlinear velocity (dY_{bd}/dt) terms of the ordinary differential equation. The damping factor, ζ_m, within the model was adjusted to match both the transition time and the overshoot characteristics of the ED motor data. The high correlation between model and ED motor dynamic data shows that the model captures the nonlinear dynamics of the ED motor.

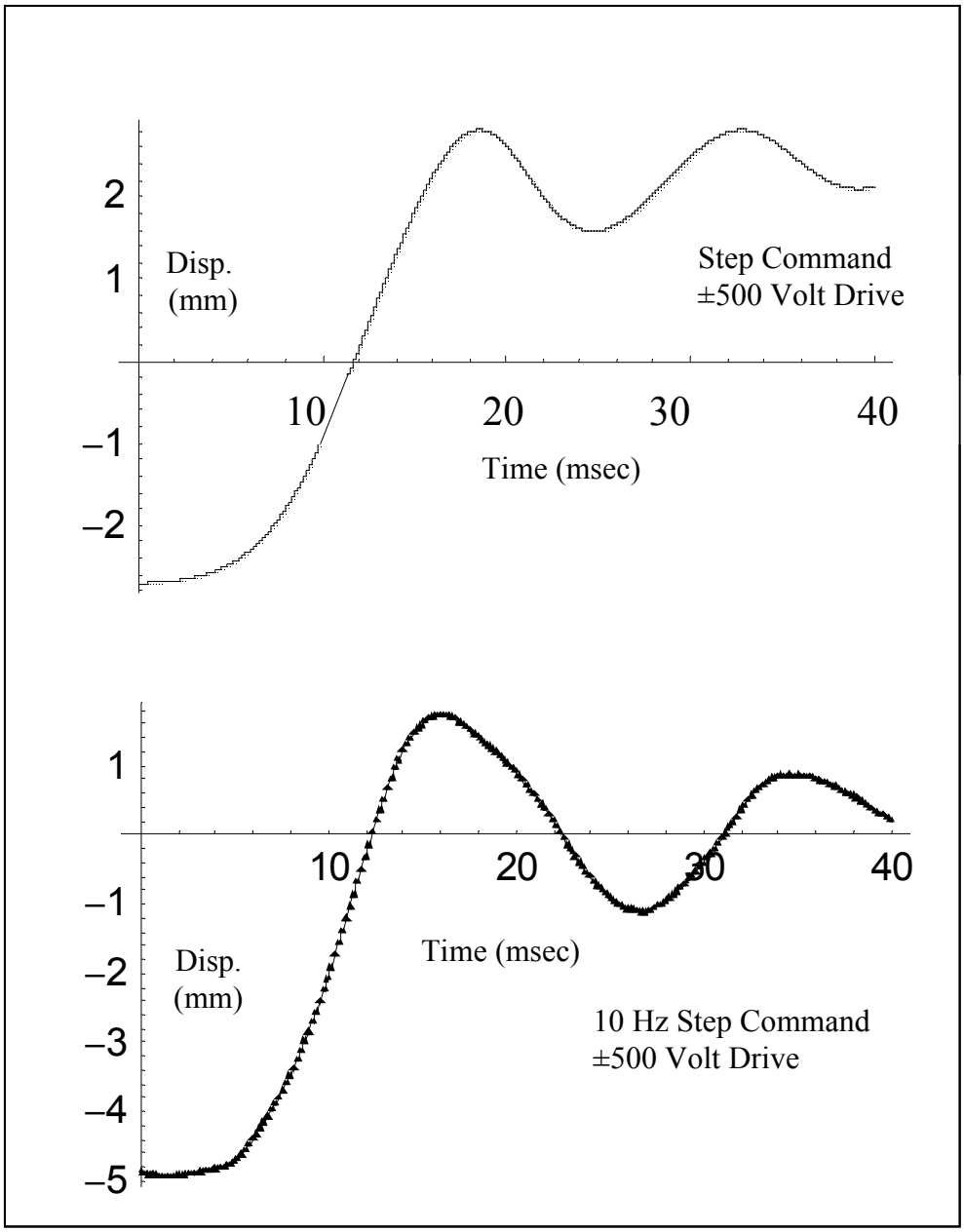

Figure 3.10 Dynamic position data from ED motor and simulation. Top: Simulated bimorph center position vs. time. Bottom: Measured bimorph center position vs. time.

Section 3.2 Synthetic Jet Actuator Design and Testing

A synthetic jet actuator was designed and built based on the ED motor. Figure 3.11 shows a solid model of the actuator.

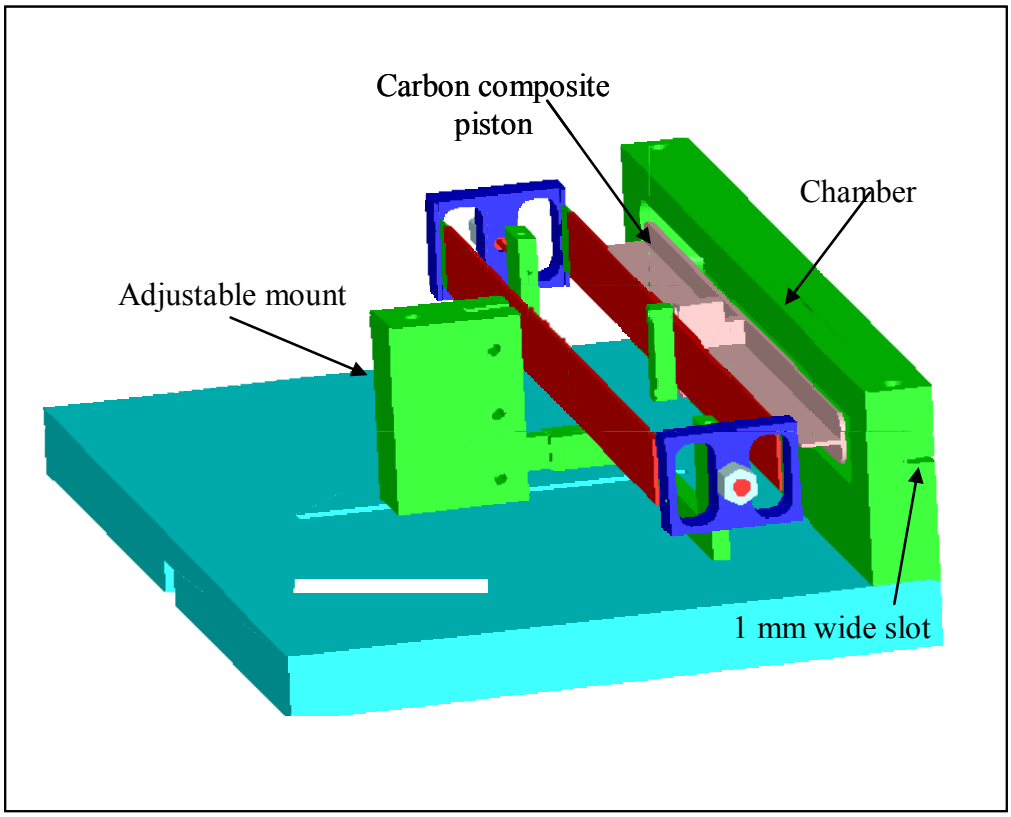

Figure 3.11 Enhanced displacement synthetic jet actuator

The actuator consists of a base, ED motor, piston and chamber. The piston is attached to the bimorph with a G10 composite clamp. The piston face is 140 X 10 mm^2 with an 8 mm mounting rib and weighs 5.4 grams. The piston is constructed from the same carbon composite as is used in the bimorph, which provides high stiffness and low mass. The piston chamber is a 15.3 X 1.4 X 1.3 cm^3 void in an aluminum block. A 0.1 cm width slot is machined into the face of the block. A latex sheet or dental dam is attached loosely between the piston and chamber to seal the chamber. The seal is held in place with double-backed tape placed on both the piston

and chamber block. The active bimorph used for the ED motor was electrically damaged during integration into the synthetic jet. The ED motor was repaired by switching the bimorph and bias beam. Switching the beams required changing the $E_b I_{bs}$ of the new bias beam by removing a 1 mm strip of composite material along the side of the bimorph beam. The trimming reduced the flexure modulus of the beam by 5%.

Subsection 3.2.1 Synthetic Jet Characterization

Measured synthetic jet properties include piston position, chamber pressure and slot dynamic pressure. A laser displacement transducer [38] was used to measure piston position and two MEMS-based pressure sensors [39] were used to measure chamber pressure (via a tube placed into the chamber) and slot dynamic pressure (via a tube placed in front of the slot).

The synthetic jet was driven by a ±500 Volt square wave applied to the PFCs. Data was recorded with square wave frequencies of 2, 10, 20 and 28 Hz. At each frequency data was taken with a full slot, 1/2 slot, 1/6 slot and a closed slot. Dynamic pressure measurements were taken with the sensor tube 0.05 cm away from the slot and located in the center of the slot. Chamber pressure was measured by a small tube inserted into the chamber and glued in place. Piston displacement was measured by a laser displacement sensor that tracked the piston displacement. Figure 3.12 shows a photograph of the synthetic jet test hardware.

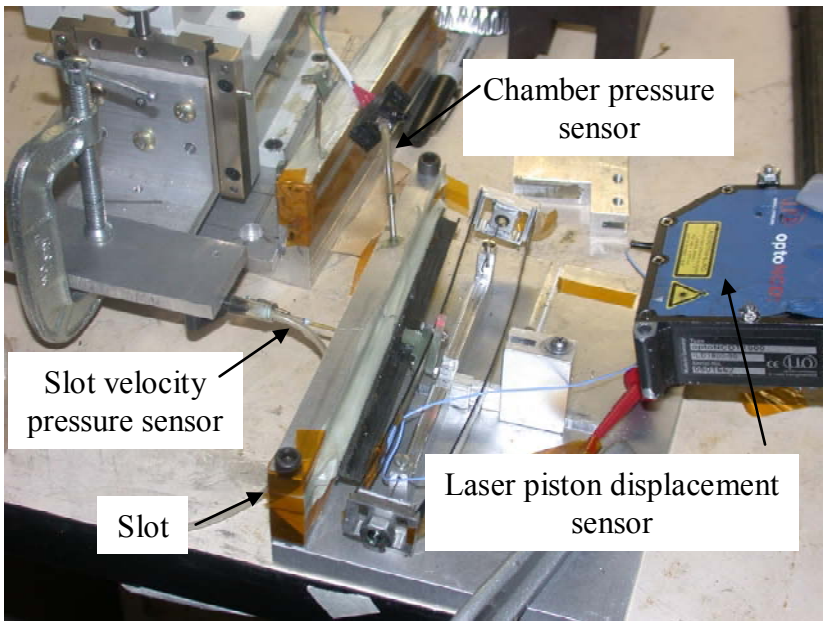

Figure 3.12 Synthetic jet actuator and sensors

Figure 3.13 shows the response of the synthetic jet to a 2 Hz, ±500 Volt square wave applied to the PFCs. Peak to peak displacement of the piston is 0.25 cm and produces a peak slot velocity of 8 m/sec over a 10 millisecond pulse. The peak chamber pressure measured is 135 Pa. The piston response is lightly damped with the amplitude transients decaying in 6 cycles. The transient rise time for this case is 10 milliseconds. The position reference is arbitrary and does not reflect the bimorph position relative to the motor.

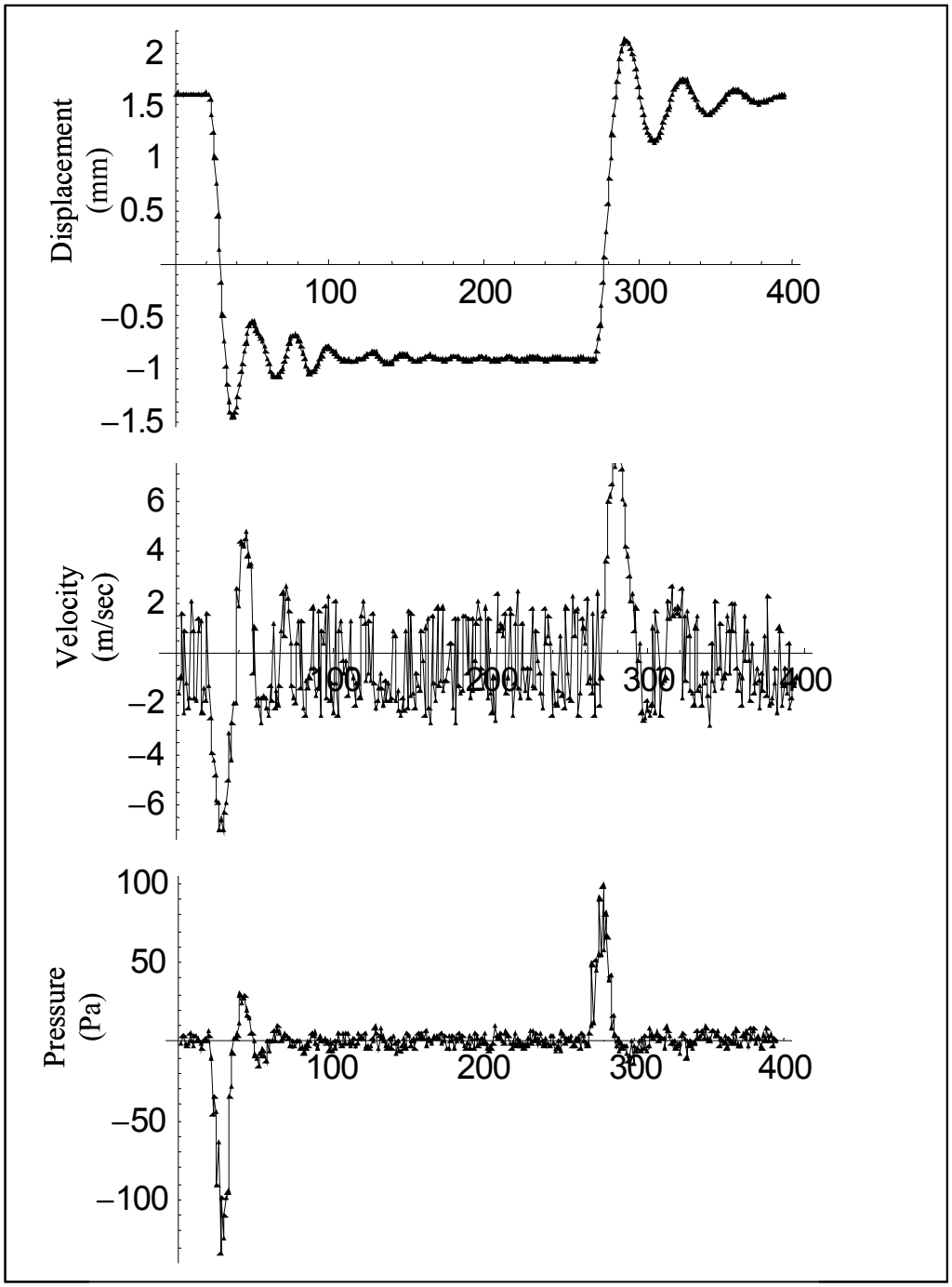

Figure 3.13 Synthetic jet performance with a 2 Hz, ±500 Volt square wave drive signal and a 1/ 6 width slot. Top: Piston displacement vs. time. Middle: Slot air velocity vs. time. Bottom Chamber pressure vs. time

Synthetic jet performance is examined while being driven by a 20 Hz, ±500 Volt square wave. Figures 3.14, 3.15 and 3.16 show performance with a full 15.3 X

0.1cm^2 slot, 7.56 X 0.1 cm^2 slot (½ slot), 2.54 X 0.1 cm^2 (1/6 slot) and a completely blocked slot. The piston is not inertia-limited when operating at 20 Hz but operation at higher frequencies will reduce piston motion due to inertial effects. This can be seen in Figure 3.13 where the piston travel is near the low duty cycle excursion. Reducing the slot size increases pressure loading on the piston which reduces piston displacement. This is shown in Figures 3.14, 3.15 and 3.16. Figure 3.17 shows the performance with a blocked slot. A theoretical slot velocity is calculated assuming the pressure generated with a blocked slot is applied to a very small slot and the resulting air velocity is calculated using the flow equation shown in Equation 2.23.

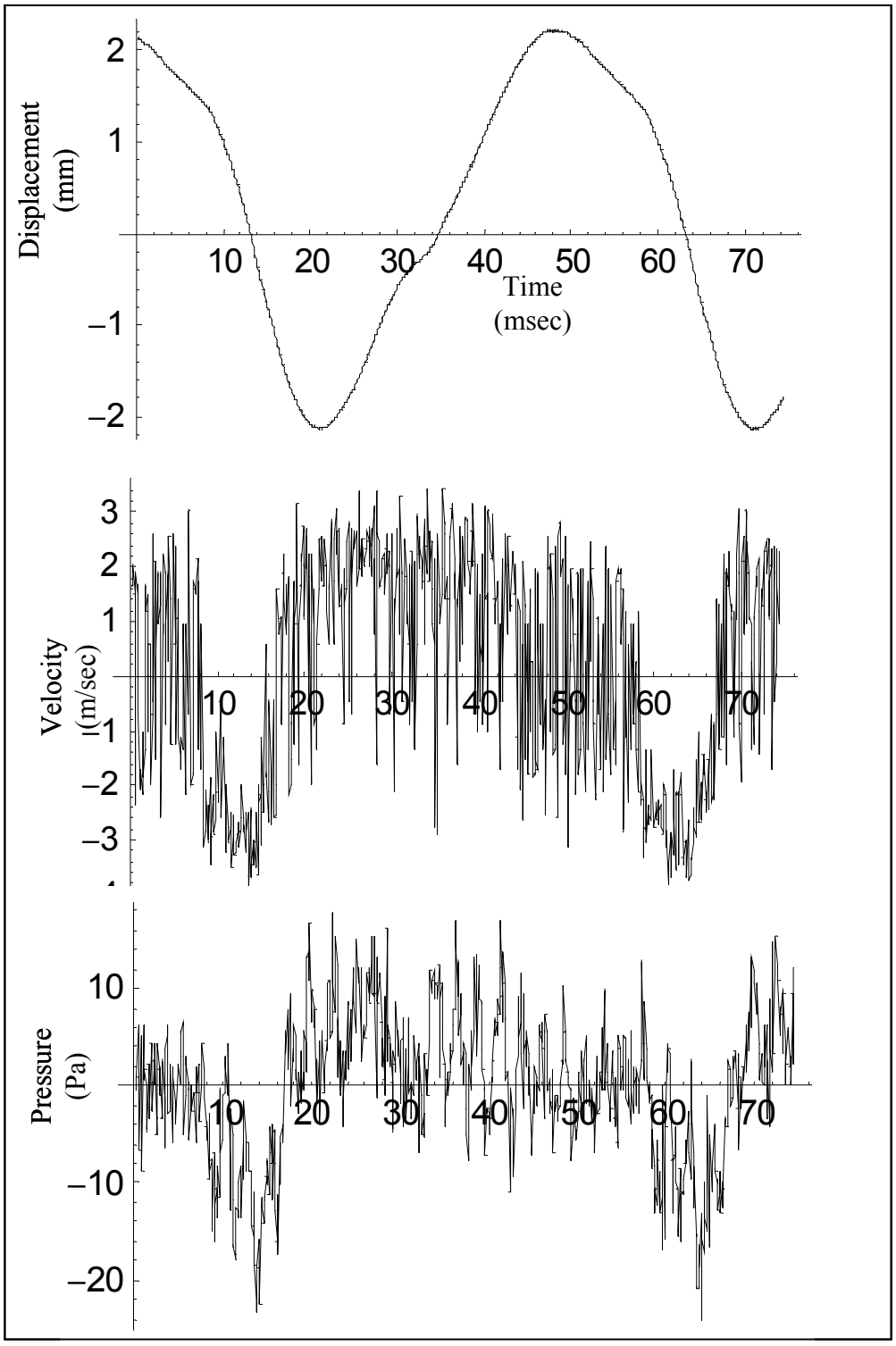

Figure 3.14 Synthetic jet full size slot with a ±500 Volt, 20 Hz square wave drive. Top: Piston position vs. time. Middle: Slot air velocity vs. time. Bottom: Chamber pressure vs. time.

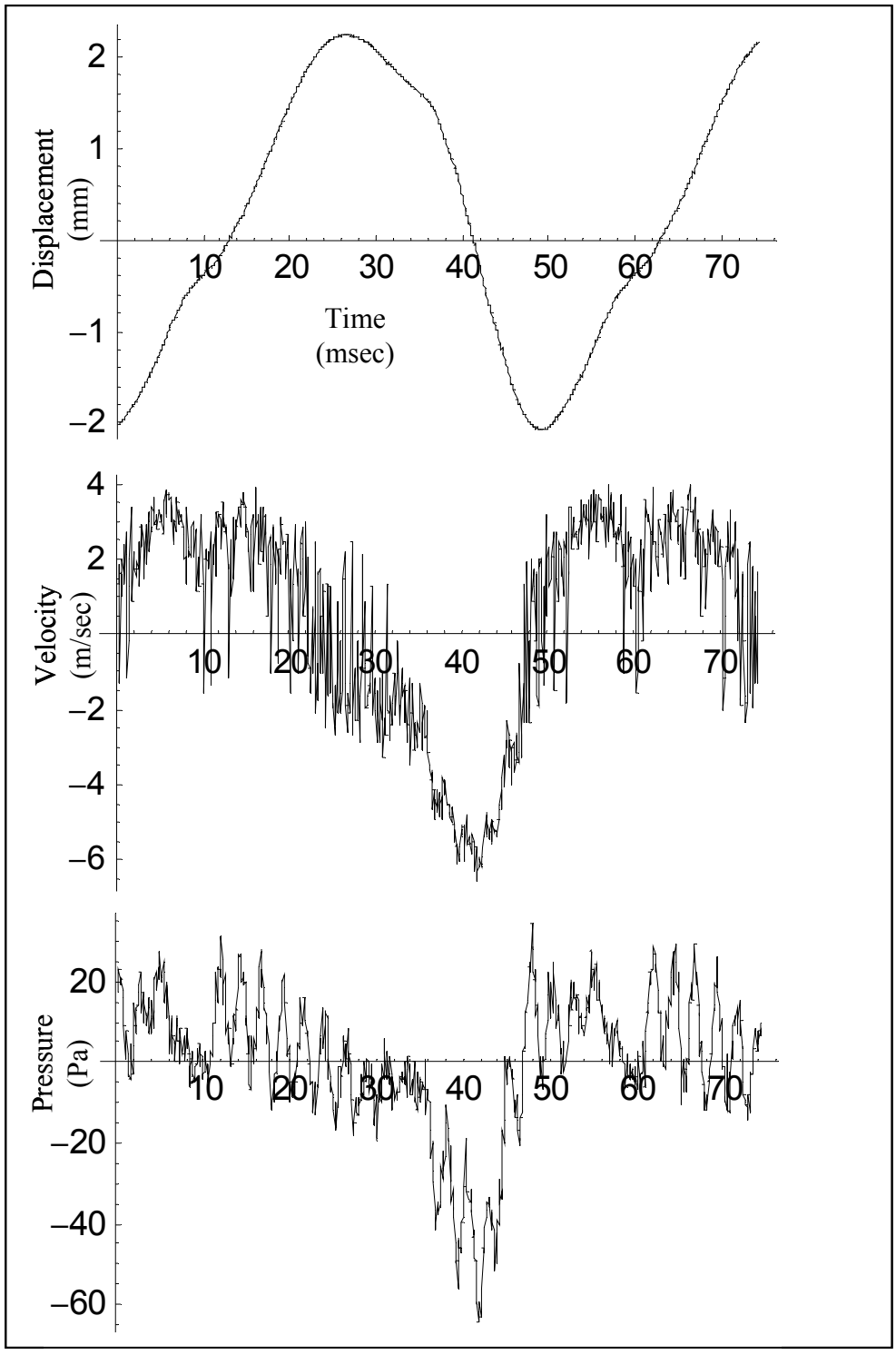

Figure 3.15 Synthetic jet 1/2 size slot with a ±500 Volt, 20 Hz square wave drive. Top: Piston position vs. time. Middle: Slot air velocity vs. time. Bottom: Chamber pressure vs. time.

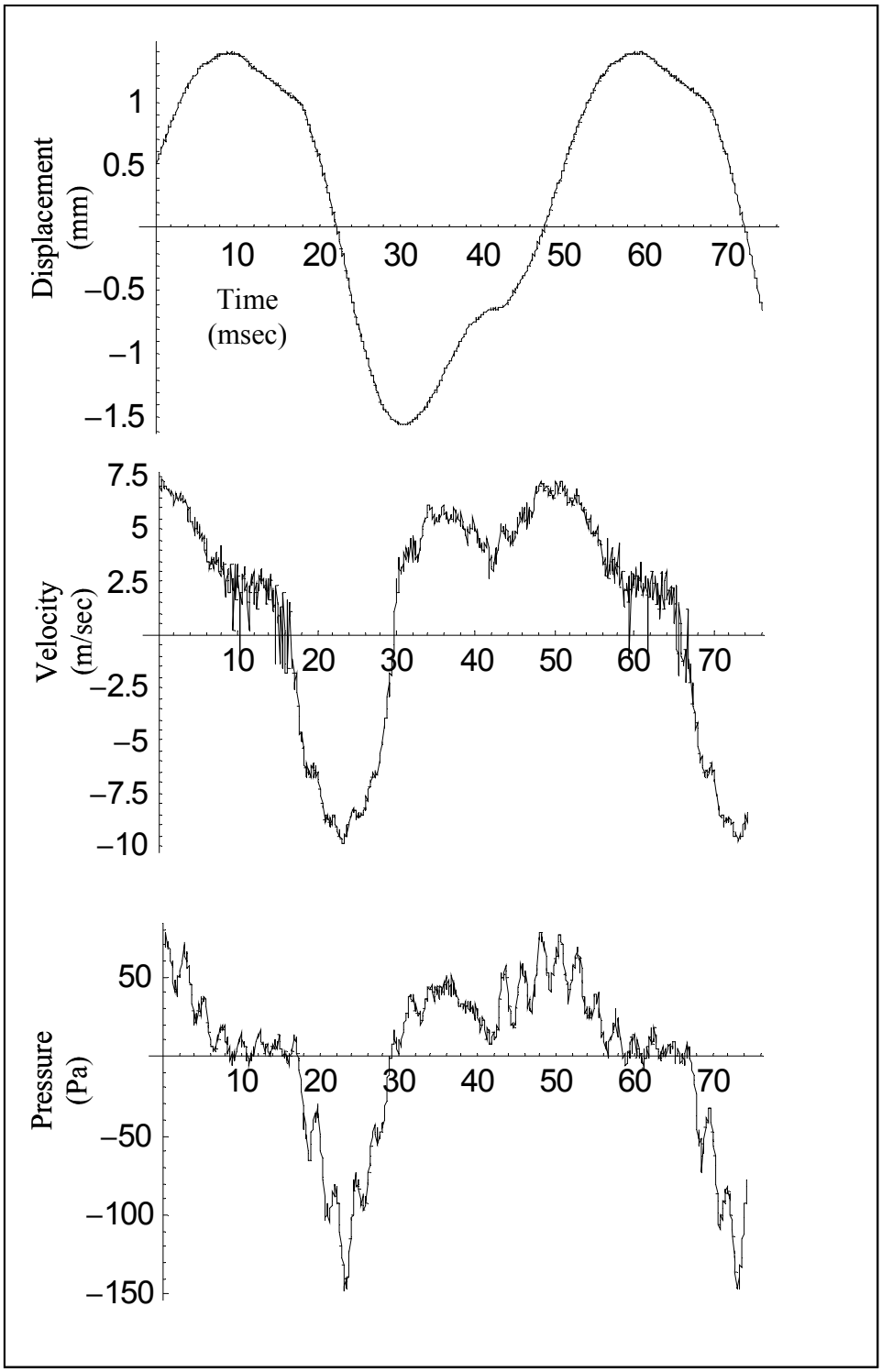

Figure 3.16 Synthetic jet 1/6 size slot with a ±500 Volt, 20 Hz square wave drive. Top: Piston position vs. time. Middle: Slot air velocity vs. time. Bottom: Chamber pressure vs. time.

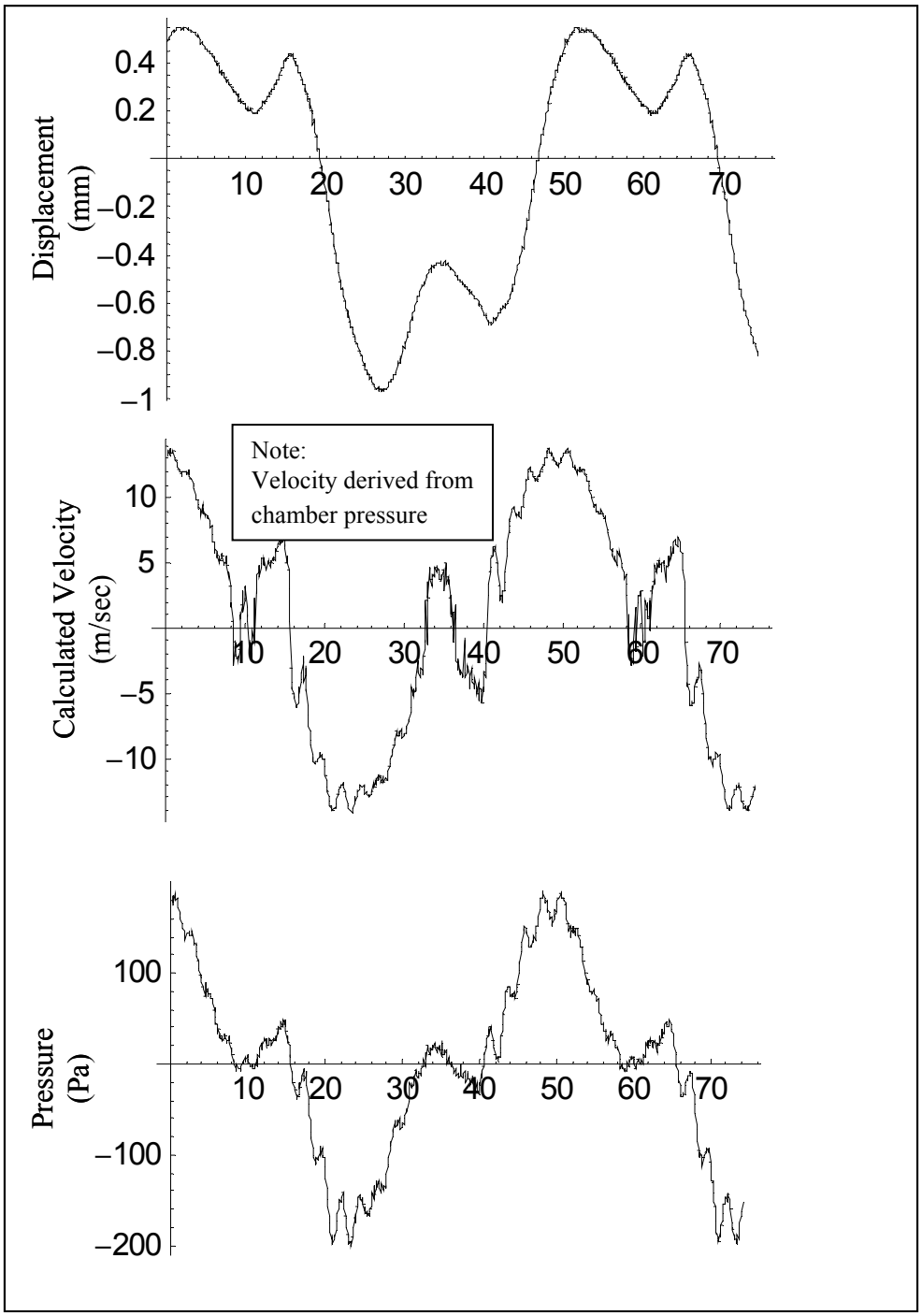

Figure 3.17 Synthetic jet blocked slot with a ±500 Volt, 20 Hz square wave drive. Top: Piston position vs. time. Middle: Calculated slot air velocity vs. time for a very small slot. Bottom: Chamber pressure vs. time.

The power delivered by the motor to the synthetic jet actuator is measured by calculating energy per cycle and multiplying this quantity by the frequency of operation. Energy per cycle is calculated by plotting the piston displacement versus the piston force and measuring the area enclosed by the plot. Piston force is calculated by multiplying the piston area by the chamber pressure. Figure 3.18 shows the force versus displacement curves for various slot sizes operating at 20 Hz.

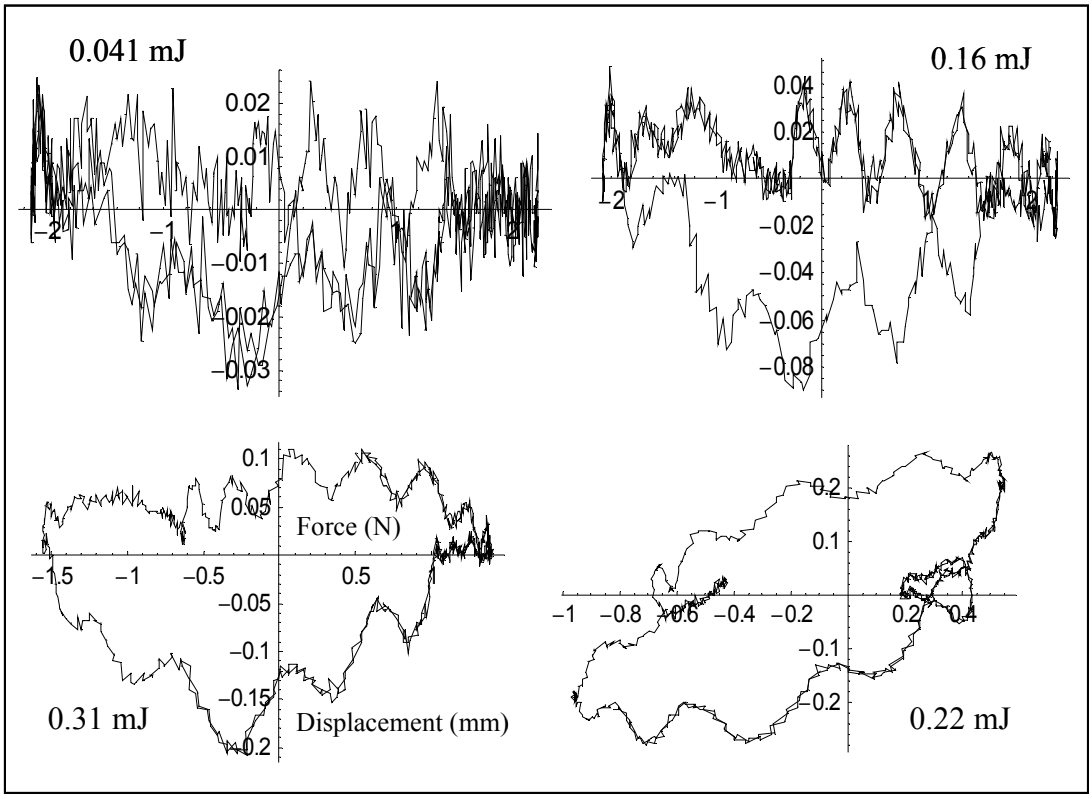

Figure 3.18 Synthetic jet piston force vs. piston displacement for different slot sizes. Plots used to calculate energy per cycle applied by the motor. ±500 Volt 20 Hz Square wave drive. Upper left: Full slot Upper right: ½ slot. Lower left: 1/6 slot. Lower right: Blocked slot.

Energy data obtained from the curves shown in Figure 3.18 shows the ED motor produces a peak power 0.31 mJ with a 1/6 slot size. Energy produced by the ED motor with a blocked slot is also significant (0.22 mJ). This energy is probably dissipated in the flexible seal.

Drive voltage and current were not measured; however, the capacitance of the bimorph is 14 nF and is driven with ±500 volts. Using these capacitance and voltage levels, the energy per cycle supplied by the amplifier is calculated to be 3.5 mJ. This leads to a motor efficiency of 9% for the 20 Hz 1/6 slot case shown in Figure 3.18. In practice, a switching amplifier would be used to drive the bimorph where 80% of the capacitive energy is recovered leading to much higher motor efficiencies [40].

A figure of merit that is useful for characterizing synthetic jet actuators is $C\mu$, described in Chapter 1. From Equation 1.1, $C\mu$ is proportional to slot area and air velocity squared. $C\mu$ performance is compared by defining a nominal aero-surface with a chord length equal to the width of the slot (0.1 cm) and a free stream velocity of 1 m/sec. Figure 3.19 compares $C\mu$ synthetic jet performance at various actuation frequencies and slot widths assuming this normalized aero-surface.

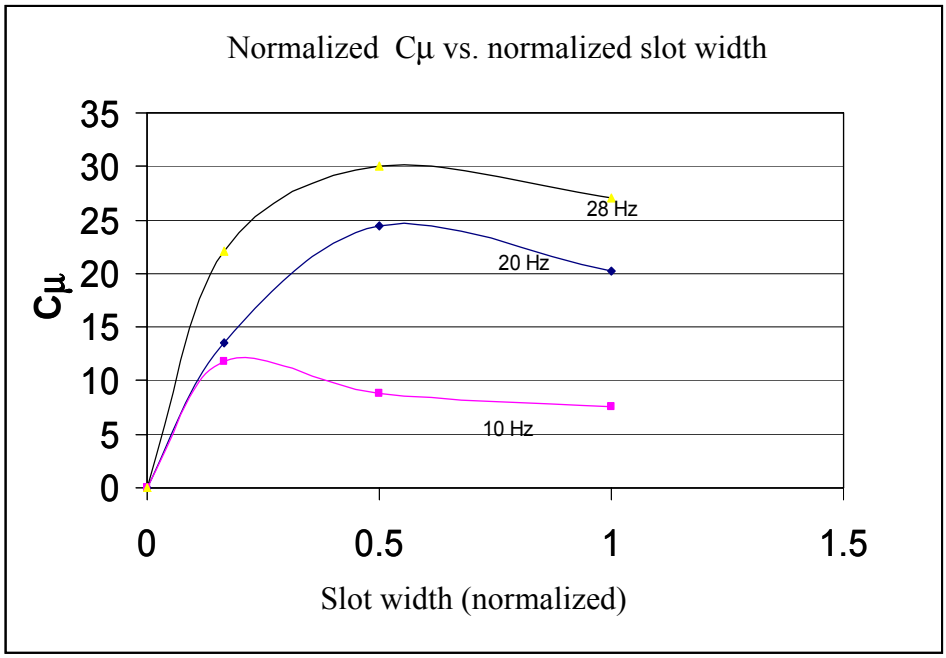

Figure 3.19 ***Cμ*** comparison between slot width and actuation frequency.

The data shown in Figure 3.19 indicates that ***Cμ*** is maximized by increasing the actuation frequency and providing a slot area of 1/2 the design slot. The 1/6 slot area case provides the highest air velocity but the total momentum is less due to the reduced slot area.

Subsection 3.2.2 Comparison of Synthetic Jet Data and Model Predictions.

The ED motor used for the synthetic jet actuator testing is different from the ED motor discussed in Chapter 2. The original bimorph was exposed to 900 volts resulting in an electrical short. The ED motor was repaired by switching the bimorph and bias beams. The new bimorph stiffness was reduced to allow proper operation of the bimorph. The new properties of both beams were measured using the static bimorph test fixture described in section 3.1. The bending stiffness of the beams and PFC induced moment are:

EI bimorph (E_bI_b) = 0.727 Nm^2

EI bias beam (E_bI_{bs}) = 0.609 Nm^2

PFC moment (M_{pfc}) = 0.118 Nm

These values were inserted in the AFC simulation along with the synthetic jet parameters which did not change. The length of the bias beam was adjusted to 14.2 cm in the simulation to allow convergence when calculating the ED motor preload. The bias beam was measured to be 15.3 cm long. Comparison data presented is based on the adjusted length. Note that the PFC moment is 70% of the moment measured in the original motor. This influences synthetic jet performance as blocked force is directly related to the pressure that can be applied to the piston and hence jet velocity.

Figures 3.20 through 3.22 show comparisons between measured data and simulated performance for ±500 Volt square wave drive signal at 10 Hz. for full and 1/6 area slots and ±500 Volt 20 Hz square wave drive signals with 1/2 area slot. Data shown is piston displacement vs. time, slot air velocity vs. time and chamber pressure vs. time.

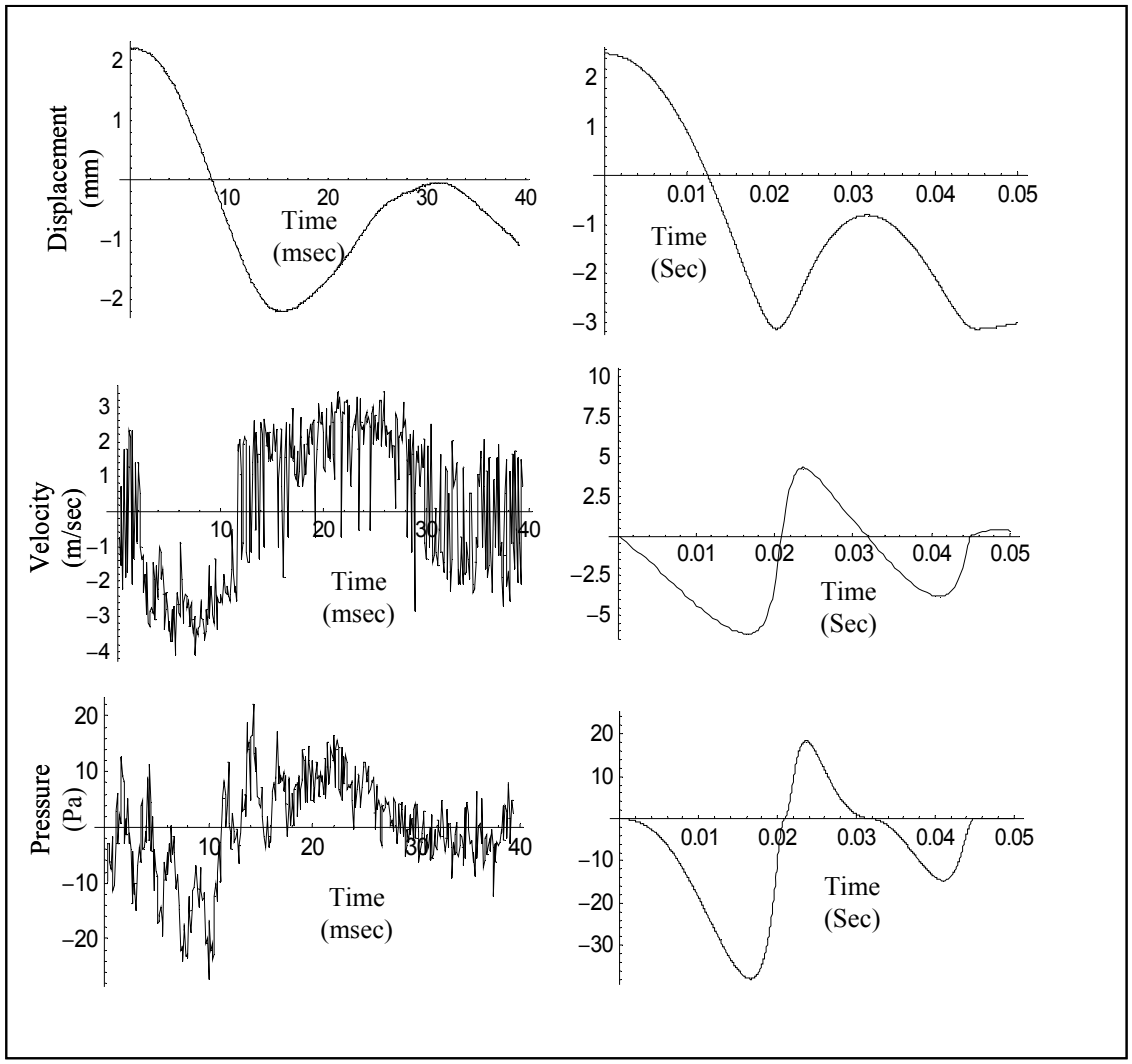

Figure 3.20 Comparison between measured and simulated synthetic full slot jet data. Drive signal: ±500 Volts, 10 Hz. Upper left: Piston displacement vs. time. Upper right: Simulated piston displacement vs. time. Middle left: Slot air velocity vs. time. Middle right: Simulated slot air velocity vs. time. Lower left: Chamber pressure vs. time. Lower right: Simulated chamber pressure vs. time.

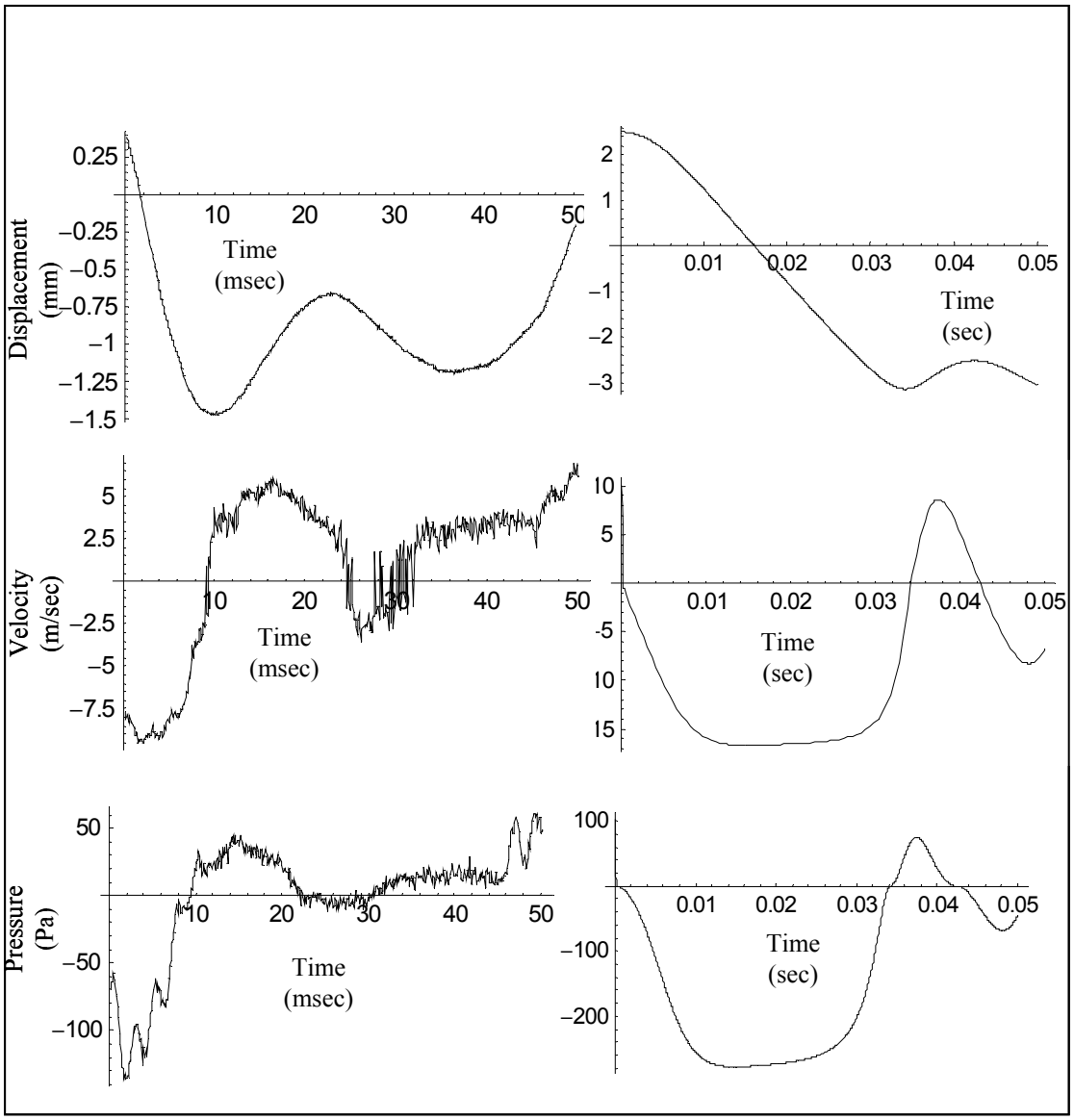

Figure 3.21 Comparison between measured and simulated synthetic jet 1/6 slot data. Drive signal: ±500 Volts, 10 Hz. Upper left: Piston displacement vs. time. Upper right: Simulated piston displacement vs. time. Middle left: Slot air velocity vs. time. Middle right: Simulated slot air velocity vs. time. Lower left: Chamber pressure vs. time. Lower right: Simulated chamber pressure vs. time.

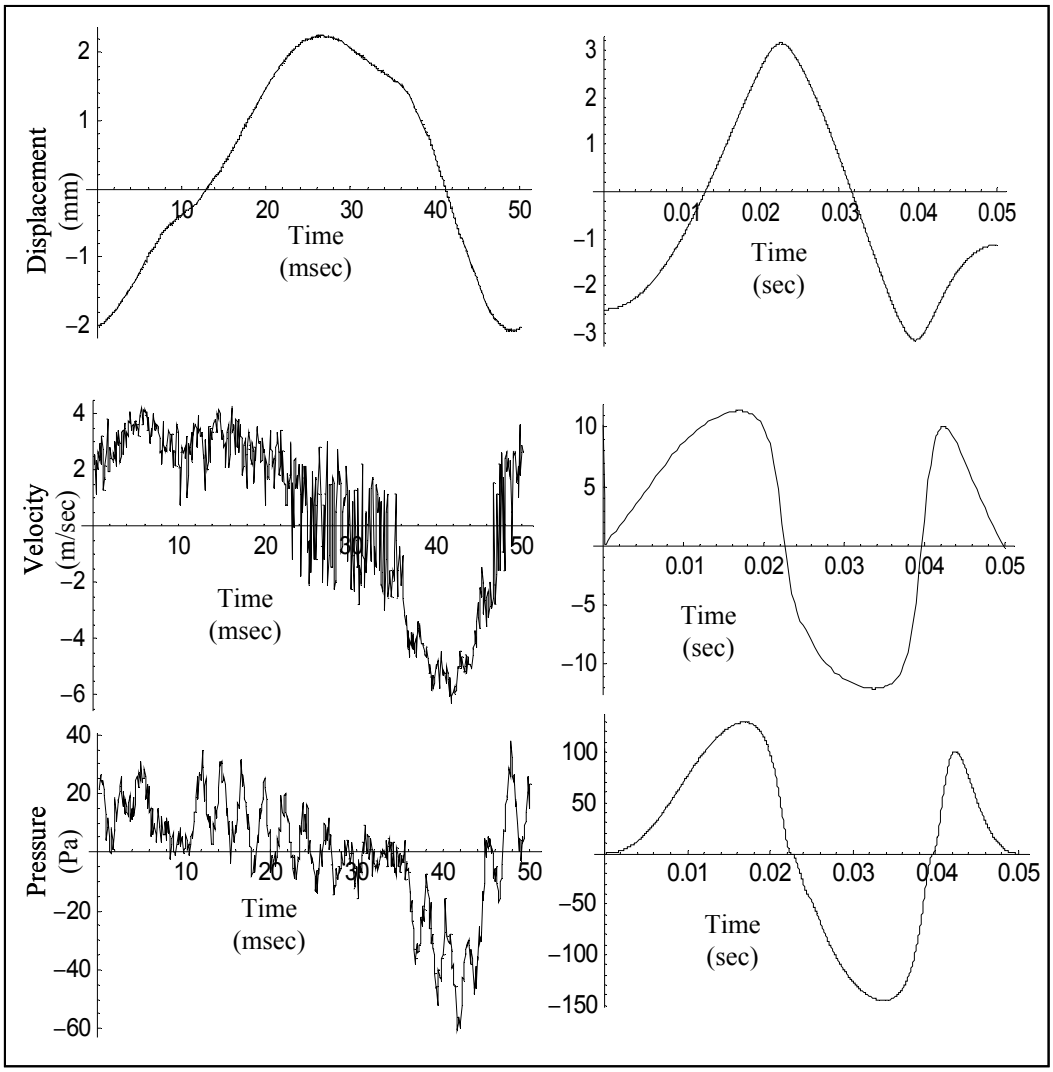

Figure 3.22 Comparison between measured and simulated synthetic jet 1/2 slot area data. Drive signal: ±500 Volts, 20 Hz. Upper left: Piston displacement vs. time. Upper right: Simulated piston displacement vs. time. Middle left: Slot air velocity vs. time. Middle right: Simulated slot air velocity vs. time. Lower left: Chamber pressure vs. time. Lower right: Simulated chamber pressure vs. time.

The model captures the synthetic jet piston dynamics as shown in Figure 3.20. The modeled rise time is faster than the measured synthetic jet rise time. This is consistent with the motor data presented earlier. Jet velocity and chamber pressure profiles are captured but the predicted magnitude is higher than the measured data.

The model over-predicts chamber pressure and slot velocity and under-predicts piston transition time as shown in Figures 3.20 and 3.21. The model assumes the piston chamber interface is a loss-less seal. The latex seal does not provide a no-loss interface. This is indicated by the large energy loss seen in the blocked slot data. Overall, the dynamics of the actuator are matched by the model and the un-modeled high loss seal is believed to cause the model to over-predict actuator performance.

Section 3.3 Synthetic Jet System Observations

The ED motor model does not include the effects of the flexure that attach the ends of the beams to the tilt connectors. These flexures can introduce a moment into the bimorph. If the buckled bimorph and bias beam lengths are not equal, an angle offset is introduced. This angle offset will apply a moment to the bimorph beam. The flexure-induced moment is consistent with the single stable position seen during the ED motor testing and is probably the cause of the poor convergence of the beam preload and the need for modifying the length of the bias beam inserted into the simulation.

The model does not capture the effect of the bias beam straightening, which unloads the bimorph beam. When the bimorph is unloaded, its stiffness becomes that of an

unbuckled beam. During high frequency operation, a noticeable clanking sound was observed that can be attributed to the bias beam unloading from the tilt connector then snapping back when the bimorph beam's full stiffness is applied to the motor.

The PFC based beams used for the ED motor exhibit visco-elastic behavior. The beams plastically deform when left under load. This phenomenon made actuator characterization difficult because the motor was constantly changing its properties and required frequent preload adjustment. During testing of the synthetic jet actuator, the motor would not adjust to a stable low stiffness setting until the bimorph was removed and placed under a center load that was sufficient to remove the beam curvature.

Chapter 4: Conclusion and Future Work

4.1 Conclusion

The ED based synthetic jet actuator demonstrates a new concept in piezoelectric actuation. Buckling the bimorph beam reduces the structural stiffness of the device allowing blocked force at a much larger displacement. A modeling technique based on Lagrange's equations was developed that predicts both static and dynamic motor performance. An air flow model based on adiabatic conditions was developed and coupled with the motor model to provide a synthetic jet model. A synthetic jet actuator was designed and tested. The ED motor demonstrated an energy-per-cycle or figure of merit increase of eight times compared to that of an unbuckled bimorph. The simulation predicts figure of merits of approximately 14. The useful bandwidth of the ED motor was about 1/3 of the bandwidth of an unbuckled bimorph motor. The ED motor demonstrated a bi-directional, nearly constant force of 1 N over a displacement of 5.5 mm. The maximum frequency for full displacement was 30 Hz. The synthetic jet demonstrated peak air velocities of 15 m/sec with a duty cycle of 30 Hz. High frequency operation was demonstrated with duty cycles varying between 1 and 30 cycles per second.

4.2 Future Work

The bimorphs' visco-elastic behavior is a significant problem for a practical ED motor. The bimorph plastically deforms when the motor is not operating, resulting in a reduced motor displacement when operation is resumed. An approach to alleviate this behavior is to fabricate bimorphs with an outer layer of uniaxial glass fiber. This

outer layer will behave as an elastic material decreasing the effect of the visco-elastic behavior of the PFCs. The increased stiffness of the bimorph will result in a higher buckling load but should not impact blocked force or free displacement as the strain capability of the glass fiber is significantly higher than the PFCs.

The flexure attachments of the bimorph and bias beams introduce a moment into the bimorph beam if the angle between the beams is not the same. This moment, although small relative to the overall beam stiffness is significant once the beam is buckled. This produces an un-modeled induced moment which results in a single stable state of the motor and a motor sensitivity to the relative lengths of the two buckled beams. Replacing the flexures with pivots may alleviate this.

The maximum frequency of the ED synthetic jet is about 30 Hz. This is too low for many applications. Adding additional layers of PFCs and shortening bimorph length will increase the synthetic jet maximum operation frequency.

The synthetic jet actuator demonstrated significantly higher losses than the model predicted. These losses are likely due to the loose fitting piston and seal material. A new piston and seal design could be developed to reduce seal losses. This might take the form of a smaller gap between piston and chamber or a rolling contact seal.

Appendices

Appendix 1 Enhanced Displacement Motor Equation of Motion

$$
\begin{aligned}
&Yd''[t] = \\
&\left(Fa + \frac{6\,Mp}{L} - \frac{EI\,\pi^6\,Yd[t]^4\,(-80\,L^2\,\pi^2\,Yd[t] - 12\,\pi^4\,Yd[t]^3)}{64\,(4\,L^3 - L\,\pi^2\,Yd[t]^2)^3} - \right. \\
&\quad \left(\pi^2\,\left(8\,EIb\,L^4\,Lb - EI\,Lb^3\,\left(8\,L^2 + \pi^2\,Y0^2\right) + EIb\,L^3\,\pi^2\,Yd[t]^2\right)^2\right. \\
&\qquad \left(4\,EIb\,L^3\,Lb\,\pi^2\,\left(-4\,EIb\,L^4 + 3\,EI\,Lb^2\,\left(8\,L^2 + \pi^2\,Y0^2\right)\right)\,Yd[t] - \right. \\
&\qquad\quad \left.\left. 12\,EIb^2\,L^6\,\pi^4\,Yd[t]^3\right)\right) / \\
&\quad \left(64\,L^4\,Lb^2\right. \\
&\qquad \left.\left(12\,EIb\,L^4\,Lb - EI\,Lb^3\,\left(8\,L^2 + \pi^2\,Y0^2\right) + EIb\,L^3\,\pi^2\,Yd[t]^2\right)^3\right) - \\
&\quad \frac{3\,EI\,L\,\pi^8\,Yd[t]^5\,(464\,L^4 - 40\,L^2\,\pi^2\,Yd[t]^2 - 3\,\pi^4\,Yd[t]^4)}{32\,(4\,L^3 - L\,\pi^2\,Yd[t]^2)^4} - \\
&\quad \frac{EI\,\pi^6\,Yd[t]^3\,(464\,L^4 - 40\,L^2\,\pi^2\,Yd[t]^2 - 3\,\pi^4\,Yd[t]^4)}{16\,(4\,L^3 - L\,\pi^2\,Yd[t]^2)^3} + \\
&\quad \left(3\,EIb\,\pi^4\,Yd[t]\right. \\
&\qquad \left(8\,EIb\,L^4\,Lb - EI\,Lb^3\,\left(8\,L^2 + \pi^2\,Y0^2\right) + EIb\,L^3\,\pi^2\,Yd[t]^2\right)^2 \\
&\qquad \left(592\,EIb^2\,L^8\,Lb^2 + 8\,EI\,EIb\,L^4\,Lb^4\,\left(8\,L^2 + \pi^2\,Y0^2\right) - \right. \\
&\qquad\quad 3\,EI^2\,Lb^6\,\left(8\,L^2 + \pi^2\,Y0^2\right)^2 + \\
&\qquad\quad 2\,EIb\,L^3\,Lb\,\pi^2\,\left(-4\,EIb\,L^4 + 3\,EI\,Lb^2\,\left(8\,L^2 + \pi^2\,Y0^2\right)\right)\,Yd[t]^2 - \\
&\qquad\quad \left.\left. 3\,EIb^2\,L^6\,\pi^4\,Yd[t]^4\right)\right) / \\
&\quad \left(32\,L\,Lb^2\right. \\
&\qquad \left.\left(12\,EIb\,L^4\,Lb - EI\,Lb^3\,\left(8\,L^2 + \pi^2\,Y0^2\right) + EIb\,L^3\,\pi^2\,Yd[t]^2\right)^4\right) - \\
&\quad \left(EIb\,\pi^4\,Yd[t]\right. \\
&\qquad \left(8\,EIb\,L^4\,Lb - EI\,Lb^3\,\left(8\,L^2 + \pi^2\,Y0^2\right) + EIb\,L^3\,\pi^2\,Yd[t]^2\right) \\
&\qquad \left(592\,EIb^2\,L^8\,Lb^2 + 8\,EI\,EIb\,L^4\,Lb^4\,\left(8\,L^2 + \pi^2\,Y0^2\right) - \right. \\
&\qquad\quad 3\,EI^2\,Lb^6\,\left(8\,L^2 + \pi^2\,Y0^2\right)^2 + \\
&\qquad\quad 2\,EIb\,L^3\,Lb\,\pi^2\,\left(-4\,EIb\,L^4 + 3\,EI\,Lb^2\,\left(8\,L^2 + \pi^2\,Y0^2\right)\right)\,Yd[t]^2 - \\
&\qquad\quad \left.\left. 3\,EIb^2\,L^6\,\pi^4\,Yd[t]^4\right)\right) /
\end{aligned}
$$

$$
\begin{aligned}
&\left(16\,L\,Lb^2\left(12\,EIb\,L^4\,Lb - EI\,Lb^3\left(8\,L^2+\pi^2\,Y0^2\right)+EIb\,L^3\,\pi^2\,Yd[t]^2\right)^3\right)-\\
&Kdamp\,Yd'[t]+\frac{3\,mb\,\pi^2\,Yd[t]\,Yd'[t]^2}{4\,L}-\frac{Ib\,\pi^4\,Yd[t]\,Yd'[t]^2}{8\,L^2\,r1^2}+\\
&\frac{128\,L^5\,mb\,\pi^6\,Yd[t]^5\,Yd'[t]^2}{\left(-4\,L^2+\pi^2\,Yd[t]^2\right)^5}+\frac{256\,L^5\,mb\,\pi^8\,Yd[t]^5\,Yd'[t]^2}{3\left(-4\,L^2+\pi^2\,Yd[t]^2\right)^5}-\\
&\frac{96\,L^3\,mb\,\pi^8\,Yd[t]^7\,Yd'[t]^2}{\left(-4\,L^2+\pi^2\,Yd[t]^2\right)^5}-\frac{64\,L^3\,mb\,\pi^{10}\,Yd[t]^7\,Yd'[t]^2}{\left(-4\,L^2+\pi^2\,Yd[t]^2\right)^5}+\\
&\frac{24\,L\,mb\,\pi^{10}\,Yd[t]^9\,Yd'[t]^2}{\left(-4\,L^2+\pi^2\,Yd[t]^2\right)^5}+\frac{16\,L\,mb\,\pi^{12}\,Yd[t]^9\,Yd'[t]^2}{\left(-4\,L^2+\pi^2\,Yd[t]^2\right)^5}-\\
&\frac{2\,mb\,\pi^{12}\,Yd[t]^{11}\,Yd'[t]^2}{L\left(-4\,L^2+\pi^2\,Yd[t]^2\right)^5}-\frac{4\,mb\,\pi^{14}\,Yd[t]^{11}\,Yd'[t]^2}{3\,L\left(-4\,L^2+\pi^2\,Yd[t]^2\right)^5}-\\
&\frac{64\,L^5\,mb\,\pi^4\,Yd[t]^3\,Yd'[t]^2}{\left(-4\,L^2+\pi^2\,Yd[t]^2\right)^4}-\frac{128\,L^5\,mb\,\pi^6\,Yd[t]^3\,Yd'[t]^2}{3\left(-4\,L^2+\pi^2\,Yd[t]^2\right)^4}+\\
&\frac{72\,L^3\,mb\,\pi^6\,Yd[t]^5\,Yd'[t]^2}{\left(-4\,L^2+\pi^2\,Yd[t]^2\right)^4}+\frac{48\,L^3\,mb\,\pi^8\,Yd[t]^5\,Yd'[t]^2}{\left(-4\,L^2+\pi^2\,Yd[t]^2\right)^4}-\\
&\frac{24\,L\,mb\,\pi^8\,Yd[t]^7\,Yd'[t]^2}{\left(-4\,L^2+\pi^2\,Yd[t]^2\right)^4}-\frac{16\,L\,mb\,\pi^{10}\,Yd[t]^7\,Yd'[t]^2}{\left(-4\,L^2+\pi^2\,Yd[t]^2\right)^4}+\\
&\frac{5\,mb\,\pi^{10}\,Yd[t]^9\,Yd'[t]^2}{2\,L\left(-4\,L^2+\pi^2\,Yd[t]^2\right)^4}+\frac{5\,mb\,\pi^{12}\,Yd[t]^9\,Yd'[t]^2}{3\,L\left(-4\,L^2+\pi^2\,Yd[t]^2\right)^4}-\\
&\Big(Lb\,mbs\,\pi^2\,Yd[t]^2\\
&\quad\Big(4\,EIb\,L^3\,Lb\,\pi^2\\
&\qquad\left(16\,EIb\,L^4\left(9+2\,\pi^2\right)-EI\,Lb^2\left(15+4\,\pi^2\right)\left(8\,L^2+\pi^2\,Y0^2\right)\right)Yd[t]+\\
&\qquad4\,EIb^2\,L^6\,\pi^4\left(15+4\,\pi^2\right)Yd[t]^3\Big)\,Yd'[t]^2\Big)\Big/\\
&\Big(48\,L^2\left(96\,EIb^2\,L^8\,Lb^2-20\,EI\,EIb\,L^4\,Lb^4\left(8\,L^2+\pi^2\,Y0^2\right)+\right.\\
&\quad EI^2\,Lb^6\left(8\,L^2+\pi^2\,Y0^2\right)^2+\\
&\quad2\,EIb\,L^3\,Lb\,\pi^2\left(10\,EIb\,L^4-EI\,Lb^2\left(8\,L^2+\pi^2\,Y0^2\right)\right)Yd[t]^2+\\
&\quad\left.EIb^2\,L^6\,\pi^4\,Yd[t]^4\right)\Big)+\\
&\Big(Lb\,mbs\,\pi^2\,Yd[t]^2\\
&\quad\Big(4\,EIb\,L^3\,Lb\,\pi^2\left(10\,EIb\,L^4-EI\,Lb^2\left(8\,L^2+\pi^2\,Y0^2\right)\right)Yd[t]+\\
&\quad4\,EIb^2\,L^6\,\pi^4\,Yd[t]^3\Big)\\
&\quad\Big(Lb^2\left(16\,EIb^2\,L^8\left(87+16\,\pi^2\right)-\right.\\
&\qquad32\,EI\,EIb\,L^4\,Lb^2\left(9+2\,\pi^2\right)\left(8\,L^2+\pi^2\,Y0^2\right)+\\
&\qquad\left.EI^2\,Lb^4\left(15+4\,\pi^2\right)\left(8\,L^2+\pi^2\,Y0^2\right)^2\right)+\\
&\quad2\,EIb\,L^3\,Lb\,\pi^2\\
&\qquad\left(16\,EIb\,L^4\left(9+2\,\pi^2\right)-EI\,Lb^2\left(15+4\,\pi^2\right)\left(8\,L^2+\pi^2\,Y0^2\right)\right)\\
&\qquad Yd[t]^2+EIb^2\,L^6\,\pi^4\left(15+4\,\pi^2\right)Yd[t]^4\Big)\,Yd'[t]^2\Big)\Big/
\end{aligned}
$$

$$
\begin{aligned}
&\Big(48\,L^2\\
&\quad\Big(96\,EIb^2\,L^8\,Lb^2-20\,EI\,EIb\,L^4\,Lb^4\,\left(8\,L^2+\pi^2\,Y0^2\right)+\\
&\qquad EI^2\,Lb^6\,\left(8\,L^2+\pi^2\,Y0^2\right)^2+\\
&\qquad 2\,EIb\,L^3\,Lb\,\pi^2\,\left(10\,EIb\,L^4-EI\,Lb^2\,\left(8\,L^2+\pi^2\,Y0^2\right)\right)\,Yd[t]^2+\\
&\qquad EIb^2\,L^6\,\pi^4\,Yd[t]^4\Big)^2\Big)+\\
&\Big(Lb\,mbs\,\pi^2\,Yd[t]\\
&\quad\Big(Lb^2\,\Big(16\,EIb^2\,L^8\,\left(87+16\,\pi^2\right)-\\
&\qquad 32\,EI\,EIb\,L^4\,Lb^2\,\left(9+2\,\pi^2\right)\,\left(8\,L^2+\pi^2\,Y0^2\right)+\\
&\qquad EI^2\,Lb^4\,\left(15+4\,\pi^2\right)\,\left(8\,L^2+\pi^2\,Y0^2\right)^2\Big)+\\
&\qquad 2\,EIb\,L^3\,Lb\,\pi^2\\
&\qquad\Big(16\,EIb\,L^4\,\left(9+2\,\pi^2\right)-EI\,Lb^2\,\left(15+4\,\pi^2\right)\,\left(8\,L^2+\pi^2\,Y0^2\right)\Big)\\
&\qquad Yd[t]^2+EIb^2\,L^6\,\pi^4\,\left(15+4\,\pi^2\right)\,Yd[t]^4\Big)\,Yd'[t]^2\Big)\Big/\\
&\Big(24\,L^2\,\Big(96\,EIb^2\,L^8\,Lb^2-20\,EI\,EIb\,L^4\,Lb^4\,\left(8\,L^2+\pi^2\,Y0^2\right)+\\
&\qquad EI^2\,Lb^6\,\left(8\,L^2+\pi^2\,Y0^2\right)^2+\\
&\qquad 2\,EIb\,L^3\,Lb\,\pi^2\,\left(10\,EIb\,L^4-EI\,Lb^2\,\left(8\,L^2+\pi^2\,Y0^2\right)\right)\,Yd[t]^2+\\
&\qquad EIb^2\,L^6\,\pi^4\,Yd[t]^4\Big)\Big)-\\
&\Big(Lb\,mbs\,\pi^2\,Yd[t]^2\\
&\quad\Big(Lb^2\,\Big(16\,EIb^2\,L^8\,\left(87+16\,\pi^2\right)-\\
&\qquad 32\,EI\,EIb\,L^4\,Lb^2\,\left(9+2\,\pi^2\right)\,\left(8\,L^2+\pi^2\,Y0^2\right)+\\
&\qquad EI^2\,Lb^4\,\left(15+4\,\pi^2\right)\,\left(8\,L^2+\pi^2\,Y0^2\right)^2\Big)+\\
&\qquad 2\,EIb\,L^3\,Lb\,\pi^2\\
&\qquad\Big(16\,EIb\,L^4\,\left(9+2\,\pi^2\right)-EI\,Lb^2\,\left(15+4\,\pi^2\right)\,\left(8\,L^2+\pi^2\,Y0^2\right)\Big)\\
&\qquad Yd[t]^2+EIb^2\,L^6\,\pi^4\,\left(15+4\,\pi^2\right)\,Yd[t]^4\Big)\,Yd'[t]\\
&\quad\Big(4\,EIb\,L^3\,Lb\,\pi^2\,\left(10\,EIb\,L^4-EI\,Lb^2\,\left(8\,L^2+\pi^2\,Y0^2\right)\right)\,Yd[t]\,Yd'[t]+\\
&\qquad 4\,EIb^2\,L^6\,\pi^4\,Yd[t]^3\,Yd'[t]\Big)\Big)\Big/\\
&\Big(24\,L^2\\
&\quad\Big(96\,EIb^2\,L^8\,Lb^2-20\,EI\,EIb\,L^4\,Lb^4\,\left(8\,L^2+\pi^2\,Y0^2\right)+\\
&\qquad EI^2\,Lb^6\,\left(8\,L^2+\pi^2\,Y0^2\right)^2+\\
&\qquad 2\,EIb\,L^3\,Lb\,\pi^2\,\left(10\,EIb\,L^4-EI\,Lb^2\,\left(8\,L^2+\pi^2\,Y0^2\right)\right)\,Yd[t]^2+\\
&\qquad EIb^2\,L^6\,\pi^4\,Yd[t]^4\Big)^2\Big)+\\
&\Big(Lb\,mbs\,\pi^2\,Yd[t]^2\,Yd'[t]\\
&\quad\Big(4\,EIb\,L^3\,Lb\,\pi^2\\
&\qquad\Big(16\,EIb\,L^4\,\left(9+2\,\pi^2\right)-EI\,Lb^2\,\left(15+4\,\pi^2\right)\,\left(8\,L^2+\pi^2\,Y0^2\right)\Big)\\
&\qquad Yd[t]\,Yd'[t]+4\,EIb^2\,L^6\,\pi^4\,\left(15+4\,\pi^2\right)\,Yd[t]^3\,Yd'[t]\Big)\Big)\Big/\\
&\Big(24\,L^2\,\Big(96\,EIb^2\,L^8\,Lb^2-20\,EI\,EIb\,L^4\,Lb^4\,\left(8\,L^2+\pi^2\,Y0^2\right)+\\
&\qquad EI^2\,Lb^6\,\left(8\,L^2+\pi^2\,Y0^2\right)^2+\\
&\qquad 2\,EIb\,L^3\,Lb\,\pi^2\,\left(10\,EIb\,L^4-EI\,Lb^2\,\left(8\,L^2+\pi^2\,Y0^2\right)\right)\,Yd[t]^2+\\
&\qquad EIb^2\,L^6\,\pi^4\,Yd[t]^4\Big)\Big)+
\end{aligned}
$$

$$\frac{1}{2}\,mb\left(-\frac{3\pi^2\,Yd[t]\,Yd'[t]^2}{4L}-\frac{128L^5\pi^6\,Yd[t]^5\,Yd'[t]^2}{(-4L^2+\pi^2\,Yd[t]^2)^5}-\frac{256L^5\pi^8\,Yd[t]^5\,Yd'[t]^2}{3\,(-4L^2+\pi^2\,Yd[t]^2)^5}+\frac{96L^3\pi^8\,Yd[t]^7\,Yd'[t]^2}{(-4L^2+\pi^2\,Yd[t]^2)^5}+\frac{64L^3\pi^{10}\,Yd[t]^7\,Yd'[t]^2}{(-4L^2+\pi^2\,Yd[t]^2)^5}-\frac{24L\pi^{10}\,Yd[t]^9\,Yd'[t]^2}{(-4L^2+\pi^2\,Yd[t]^2)^5}-\frac{16L\pi^{12}\,Yd[t]^9\,Yd'[t]^2}{(-4L^2+\pi^2\,Yd[t]^2)^5}+\frac{2\pi^{12}\,Yd[t]^{11}\,Yd'[t]^2}{L\,(-4L^2+\pi^2\,Yd[t]^2)^5}+\frac{4\pi^{14}\,Yd[t]^{11}\,Yd'[t]^2}{3L\,(-4L^2+\pi^2\,Yd[t]^2)^5}+\frac{64L^5\pi^4\,Yd[t]^3\,Yd'[t]^2}{(-4L^2+\pi^2\,Yd[t]^2)^4}+\frac{128L^5\pi^6\,Yd[t]^3\,Yd'[t]^2}{3\,(-4L^2+\pi^2\,Yd[t]^2)^4}-\frac{72L^3\pi^6\,Yd[t]^5\,Yd'[t]^2}{(-4L^2+\pi^2\,Yd[t]^2)^4}-\frac{48L^3\pi^8\,Yd[t]^5\,Yd'[t]^2}{(-4L^2+\pi^2\,Yd[t]^2)^4}+\frac{24L\pi^8\,Yd[t]^7\,Yd'[t]^2}{(-4L^2+\pi^2\,Yd[t]^2)^4}+\frac{16L\pi^{10}\,Yd[t]^7\,Yd'[t]^2}{(-4L^2+\pi^2\,Yd[t]^2)^4}-\frac{5\pi^{10}\,Yd[t]^9\,Yd'[t]^2}{2L\,(-4L^2+\pi^2\,Yd[t]^2)^4}-\frac{5\pi^{12}\,Yd[t]^9\,Yd'[t]^2}{3L\,(-4L^2+\pi^2\,Yd[t]^2)^4}\right)\Big/$$

$$\left(Mass+\frac{L\,mb}{2}-\frac{3\,mb\,\pi^2\,Yd[t]^2}{8L}+\frac{Ib\,\pi^4\,Yd[t]^2}{8L^2\,r1^2}+\frac{16L^5\,mb\,\pi^4\,Yd[t]^4}{(-4L^2+\pi^2\,Yd[t]^2)^4}+\frac{32L^5\,mb\,\pi^6\,Yd[t]^4}{3\,(-4L^2+\pi^2\,Yd[t]^2)^4}-\frac{12L^3\,mb\,\pi^6\,Yd[t]^6}{(-4L^2+\pi^2\,Yd[t]^2)^4}-\frac{8L^3\,mb\,\pi^8\,Yd[t]^6}{(-4L^2+\pi^2\,Yd[t]^2)^4}+\frac{3L\,mb\,\pi^8\,Yd[t]^8}{(-4L^2+\pi^2\,Yd[t]^2)^4}+\frac{2L\,mb\,\pi^{10}\,Yd[t]^8}{(-4L^2+\pi^2\,Yd[t]^2)^4}-\frac{mb\,\pi^{10}\,Yd[t]^{10}}{4L\,(-4L^2+\pi^2\,Yd[t]^2)^4}-\frac{mb\,\pi^{12}\,Yd[t]^{10}}{6L\,(-4L^2+\pi^2\,Yd[t]^2)^4}-\left(Lb\,mbs\,\pi^2\,Yd[t]^2\left(Lb^2\left(16\,EIb^2\,L^8\left(87+16\pi^2\right)-32\,EI\,EIb\,L^4\,Lb^2\left(9+2\pi^2\right)\left(8L^2+\pi^2\,Y0^2\right)+EI^2\,Lb^4\left(15+4\pi^2\right)\left(8L^2+\pi^2\,Y0^2\right)^2\right)+2\,EIb\,L^3\,Lb\,\pi^2\left(16\,EIb\,L^4\left(9+2\pi^2\right)-EI\,Lb^2\left(15+4\pi^2\right)\left(8L^2+\pi^2\,Y0^2\right)\right)Yd[t]^2+EIb^2\,L^6\,\pi^4\left(15+4\pi^2\right)Yd[t]^4\right)\right)\Big/\left(24L^2\left(96\,EIb^2\,L^8\,Lb^2-20\,EI\,EIb\,L^4\,Lb^4\left(8L^2+\pi^2\,Y0^2\right)+EI^2\,Lb^6\left(8L^2+\pi^2\,Y0^2\right)^2+2\,EIb\,L^3\,Lb\,\pi^2\left(10\,EIb\,L^4-EI\,Lb^2\left(8L^2+\pi^2\,Y0^2\right)\right)Yd[t]^2+EIb^2\,L^6\,\pi^4\,Yd[t]^4\right)\right);$$

Appendix II: Uni-axial carbon prepreg properties

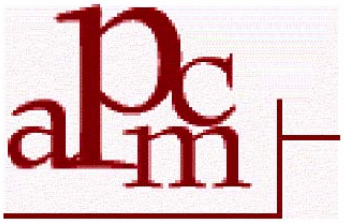

DA 911U
Unidirectional Carbo
Epoxy Prereg System

DESCRIPTION

DA 911U is a tough, versatile, modified epoxy resin system that cures at 350°F to 400°F. DA911U can be supplied as a prepreg tape coated on unidirectional graphite.

PHYSICAL PROPERTIES

Weight:	0.053 lbs./sq ft
Resin Content:	40% by Weight
Volatiles:	Less than 1%
Tack:	Medium
Gel Time:	71 Minutes, 9 Seconds at 300°F 25 Minutes, 4 Seconds at 350°F 9 Minutes, 15 Seconds at 400°F
Shelf Life:	One year at 0°F with a cumulative out time of 150 hours at room temperature.
Standard Roll:	per customer request.

MECHANICAL PROPERTIES

Cure Cycle:	Press cured for two hours at 350°F and 50 psi pressure or one hour at 400°F with a 2 to 5°F per minute ramp time.	
Thickness:	0.006 inch/ply	
Resin Content:	32% by Weight	
Interlaminar Shear	(ASTM D 2344)	14.6 KSI
Tensile Strength	(ASTM D 3039)	250 KSI
Tensile Modulus	(ASTM D 3039)	17.5 MSI

ADHESIVE PREPREGS FOR COMPOSITES MANUFACTURERS
P.O. BOX 264 1366 NORWICH RD. PLAINFIELD CT 06374
PHONE 860-564-7817 FAX 860-564-1535 www.prepregs.com

Bibliography

References:

1) C. Lachlen and D. Cerchie, Private conversation. Aerodynamics and Fluid Laboratory, University of Arizona, December 2002.

2) A.A. Hassan, **"**Applications of Zero-Net-Mass Jets for Enhanced Rotorcraft Aerodynamic Performance", AIAA Journal of Aircraft, Vol. 38, No. 3, May-June 2001.

3) W.L. Sellers III, G.S. Jones and M.D. Moore, "Flow Control Research at NASA Langley in Support of High-Lift Augmentation", AIAA 2002-6006, Biennial International Powered Lift Conference and Exhibit, 5-7 November 2002, Williamsburg VA.

4) V.R. D'Andrea, R.L. Behnken and R.M. Murray, "Active control of an axial flow compressor via pulsed air injection", ASME Journal of Turbomachinery, vol. 119, No. 4, 1997.

5) F.T. Calkins and D.J. Clingman, "Vibrating surface actuators for active flow control", Proceedings of SPIE -- Vol. 4698, pp. 85-96, Smart Structures and Materials Conference, 2002.

6) B.L. Smith and A. Glezer, "Vectoring and Small-Scale Motions Effected in Free Shear Flows Using Synthetic Jet Actuators", AIAA 97-0213, Jan. 1997.

7) F.T. Calkins, J. H. Mabe, J. P. Smith and D.J. Arbogast, "Low frequency (F+=1.0) multilayer piezopolymer synthetic jets for active flow control", AIAA-2002-2823, 1st Flow Control Conference, St. Louis, Missouri, June 24-26, 2002.

8) M. Amitay, B. L. Smith, and A. Glezer , "Aerodynamic Flow Control Using Synthetic Jet Technology", AIAA 98-0208, Aerospace Sciences Meeting and Exhibit, 36th, Reno, NV, January 12-15, 1998.

9) JL Gilarranz, LW Traub, OK Rediniotis "A New Class of Synthetic Jet Actuators—Part I: Design, Fabrication and Bench Top Characterization", Journal of Fluids Engineering 127, 367, 2005

10) F. Chen and G. Beeler, NASA Langley Research Center, Hampton, VA "Virtual Shaping of a Two-dimensional NACA 0015 Airfoil Using Synthetic Jet Actuator" , AIAA-2002-3273 1st Flow Control Conference, St. Louis, Missouri, June 24-26, 2002

11) D. C. McCormick, “Boundary Layer Separation Control with Directed Synthetic Jets”, AIAA 2000-0519, Aerospace Sciences Meeting and Exhibit, 38th, Reno, NV, January 10-13, 2000.

12) R. Funk, D. Parekh, T. Crittenden and A. Glezer, “Transient Separation Control Using Pulse Actuation “, AIAA-2002-3166 , 1st Flow Control Conference, St. Louis, Missouri, June 24-26, 2002

13) A Glezer. Private conversation, DARPA Nano UAV Workshop. February 2004

14) Raman G.1; Khanafseh S.; Cain A.B.; Kerschen E. “ Development of high bandwidth powered resonance tube actuators with feedback control” , Journal of Sound and Vibration, Volume 269, Number 3, 22 January 2004

15) Frederick T. Calkins and James H. “Multilayer PVDF actuators for active flow control, AIAA-2001-1560 AIAA/ASME/ASCE/AHS/ASC Structures, Structural Dynamics, and Materials Conference and Exhibit, 42nd, Seattle, WA, Apr. 16-19, 2001

16) Q. Gallas, R. Holman, T. Nishida, B. Carroll, M. Sheplak and L. Cattafesta, “Lumped Element Modeling of Piezoelectric-Driven Synthetic Jet Actuators”, AIAA Journal, 0001-1452, Vol.41, No.2 (240-247), February 2003.

17) Ahmed A. Hassan and Edwin A, “Transverse and near-tangent synthetic jets for aerodynamic flow control” ,AIAA-2000-4334 ,AIAA Applied Aerodynamics Conference and Exhibit, 18th, Denver, CO, Aug. 14-17, 2000

18) S. Ugania and A. Flatau, “Investigation of synthetic jet actuator design parameters”, Proceedings of SPIE -- Volume 5390, Smart Structures and Materials 2004: Smart Structures and Integrated Systems, July 2004, pp. 284-296

19) Nail K. Yamaleev; Mark H. Carpenter; Frederick Ferguson, “Reduced-Order Model for Efficient Simulation of Synthetic Jet Actuators”, AIAA Journal 2005 0001-1452 vol.43 no.2 (357-369)

20) Poorna Mane, Karla Mossi1, Robert Bryant, “Synthetic jets with piezoelectric diaphragms”, Proceedings of SPIE -- Volume 5761,Smart Structures and Materials 2005: Active Materials: Behavior and Mechanics, May 2005, pp. 233-243

21) PIEZO SYSTEMS, INC., 186 Massachusetts Avenue Cambridge, MA 02139, http://www.piezo.com/tech2intropiezotrans.html

22) Prechtel, E and Hall, S "X-Frame-actuator servo flap actuation system for rotor control" , Proc. SPIE Vol. 3329, p. 309-320, Smart Structures and Materials 1998: Smart Structures and Integrated Systems.

23) R.F. Osborn, S. Kota, J. A. Hetrick, D. E. Geister, C. P. Tilmann, J. Joo, "Active Flow Control Using High-Frequency Compliant Structures", Journal of Aircraft, 0021-8669, Vol.41, No.3, May–June 2004 (603-609).

24) G. A. Lesieutre, J. Loverich, G. H. Koopmann and E. M. Moockenstrum, "A Nonlinear Transmission that Increases Piezo-Stack Work Output ", AIAA-2003-1639, 44th AIAA/ASME/ASCE/AHS/ASC Structures, Structural Dynamics, and Materials Conference, Norfolk, Virginia, Apr. 7-10, 2003

25) Bailo, Kelly C.; Brei, Diann E. Calkins, Frederick T, "Investigation of PVdF active diaphragms for synthetic jets", Proc. SPIE Vol. 3991, p. 220-231, Smart Structures and Materials 2000.

26) Ervin, J.D. Brei, D.E, ".Dynamic behavior of piezoelectric recurve actuation architectures", Journal of Vibration and Acoustics (Transactions of the ASME). Vol. 126, no. 1, pp. 37-46. Jan. 2004

27) G. Lesieutre and C. Davis, "Can a coupling coefficient of a piezoelectric device be higher than those of its active material?," Journal of intelligent material systems and structures 8{1O], p. 859, 1997.

28) D. J. Clingman and R. T. Ruggeri , "Mechanical strain energy shuttle for aircraft morphing via wing twist or structural deformation", Proceedings of SPIE -- Volume 5388 Smart Structures and Materials 2004: Industrial and Commercial Applications of Smart Structures Technologies

29) J. Darío Aristizábal-Ochoa, "Large Deflection Stability of Slender Beam-Columns with Semirigid Connections: Elastica Approach" J. Engrg. Mech., Volume 130, Issue 3, pp. 274-282 (March 2004)

30) C. T. Sun "Mechanics of Aircraft Structures" Publisher: John Wiley & Sons 1998, ISBN 0-471-17877-2

31) M.T.A. Saif, "On a Tunable Bistable MEMS—Theory and Experiment", Journal of Microelectromechanical Systems, Vol. 9 No. 2, June 2000.

32) C. Cadou, Associate Professor, University of Maryland. Private conversation, Fall 2004.

33) Advanced Cerametrics Inc. PO Box 128, Lambertville, NJ, 08530, Phone: (800) 261-1208 www.advancedcerametrics.com

34) Inder Chopra, University of Maryland ANAE 652 Smart Structures class notes. Fall 2004.

35) Wolfram Research, Inc. 100 Trade Center Drive. Champaign, Illinois 61820, Phone: 217-398-0700

36) John N. Cernica, "Strength of Materials", Second Edition, 1997 Publisher: Holt, Rinehart and Winston Pg 284-286

37) Leonard Meirovitch, "Fundamentals of Vibration", New York: McGraw-Hill.

38) Laser Displacement Sensor. Micro-Epsilon, http://www.micro-epsilon.com 3200 Glen Royal Road, Suite 110, Raleigh, NC 27617-7419 Part Number ILD 2200-50

39) MXP5010DP Case 867C-95 Freescale Semiconductor Inc

40) Clingman, D. J. "Drive Electronics for Large Piezoactuators," *Proceeding of SPIE's 1997 North American Symposium on Smart Structures and Materials:*

Industrial and Commercial Applications of Smart Structures Technologies, Janet M. Sater; Ed., Vol. 3044, San Diego, CA, March, 1997, pp. 459-467